Multiscale Modeling of CO_2 Migration and Trapping in Fractured Reservoirs with Validation by Model Comparison and Real-Site Applications

Final Technical Report

Reporting Period: 10/01/2014 through 09/30/2018

Michael A. Celia, professor, celia@princeton.edu, 609-258-5425

Karl W. Bandilla, associate research scholar, bandilla@princeton.edu

DOE Award #: DE-FE0023323

01/18/19

The Trustees of Princeton University

New South Building

ORPA, P.O. BOX 36

Princeton, NJ 08544-2020

Disclaimer

Abstract

This report documents the accomplishments achieved during the project titled "Multiscale Modeling of CO_2 Migration and Trapping in Fractured Reservoirs with Validation by Model Comparison and Real-Site Applications" funded by the US Department of Energy, Office of Fossil Energy. The objectives of the project were to develop modeling capabilities for predicting CO_2 and brine migration in fractured reservoirs during geologic carbon storage and to investigate the feasibility of carbon storage in fractured reservoirs using the newly developed modeling capabilities. To achieve these objectives new mass transfer functions were developed to adapt existing dual-continuum approaches – a commonly used approach in hydrocarbon reservoir modeling – to the CO_2-brine system. In the dual-continuum approach the undisturbed rock matrix and the fractures are modeled as two separate continua, which are coupled through mass exchange of CO_2 and brine between the two continua. Mass transfer functions represent the mass exchange between fractures and the rock matrix, without requiring highly resolved numerical grids of individual fractures, thus allowing large modeling domains relevant to geologic carbon storage questions (tens of meters to hundreds of kilometers).

Mass transfer functions for the exchange of both free-phase CO_2 and brine between fractures and rock matrix were developed for both the injection phase and the post-injection phase. During the injection phase the fractures are filled with CO_2, while the rock matrix is initially filled with brine. Therefore, a mass transfer function was developed that is based on vertical displacement of brine by CO_2 in the rock matrix due to gravitational forces. Once CO_2 injection ceases and CO_2 migrates away from the direct vicinity of the injection site, the fractures will begin to re-fill with brine, while the rock matrix will have high CO_2 saturations. For these conditions a mass transfer functions was developed that is based on spontaneous imbibition, as the pore spaces in the rock matrix are much smaller than in the fractures. For formations with low permeability or high capillary entry pressure of the rock matrix, free-phase CO_2 may not be able to enter the rock matrix. However, free-phase CO_2 at the interface between fractures and rock matrix can dissolve into brine resident in the rock matrix. Therefore, additional mass transfer functions were developed based on aqueous-phase diffusion of CO_2 through the rock matrix. These mass transfer functions are based on existing solutions for diffusion and were expanded to be applicable to a variety of block shapes relevant to dual-continuum modeling. Implementations of the newly developed mass transfer functions showed that they give accurate results when compared to highly resolved models.

In addition to developing new transfer functions, a new vertically-integrated dual-continuum modeling framework was developed. This development takes advantage of fast vertical segregation of CO_2 and brine in the fractures due to the density difference between CO_2 and brine and the high permeability of the fractures. Therefore, a vertically-integrated vertical equilibrium model for the fractures is coupled with a vertically-distributed model for the rock matrix. The newly developed approach significantly reduces the computational effort, but is only accurate for fracture permeabilities of 100 mD or higher.

Finally, the newly developed models were applied to real and hypothetical geologic carbon storage sites to investigate the feasibility of using fractured reservoirs for carbon storage. The

general results were, that storage of CO_2 – both as free-phase and dissolved – is feasible, but that storage capacities are likely lower than in unfractured systems. While the high permeability of the fractures reduces the injection pressure (or permits higher injection rates), fast migration of CO_2 may limit the overall storage volume, because CO_2 may escape laterally with not enough of the rock matrix being swept for effective storage.

Table of Contents

1 Executive Summary

The main goal of the project was to develop new modeling approaches to improve the accuracy of modeling CO_2 and brine migration and CO_2 storage in fractured reservoirs by including interactions of flow in fractures and the rock matrix. This was accomplished by achieving four primary objectives: 1) study the small-scale interactions between fracture and matrix flow using numerical modeling, and use the results to develop new mass transfer functions for CO_2 and brine; 2) incorporate the new mass transfer functions into the existing reservoir simulator MRST and develop a new vertically integrated modeling approach for fractured reservoirs that includes the new mass transfer functions; 3) investigate CO_2 storage capacity and trapping efficiency in site-scale fractured reservoirs with various sensitivity analyses using the newly developed mass transfer functions; and 4) apply the newly developed modeling capabilities to predict CO_2 migration and trapping at the In Salah storage site and conduct sensitivity analysis of fracture-matrix interactions and compare the simulation results with monitoring data. Princeton University, in conjunction with the two projects partners, Lawrence Berkeley National Laboratory and Heriot-Watt University, achieved the goals of the project and a brief description of the main achievements is given below.

Development of new mass transfer functions: New mass transfer functions to represent the interaction of CO_2 and brine between fractures and the rock matrix were developed for both the injection phase and the post-injection phase. Using highly resolved numerical models of a single rock matrix block showed that gravity drainage is the dominant process for mass transfer during the injection phase. Therefore, an exponential decay-type mass transfer function was chosen. Insights from a vertical fractional flow formulation of fluid displacement led to an estimation of the drainage time scale, which is an important parameter for the mass transfer function. The drainage time scale is calculated based on rock and fluid properties, and thus does not need to be calibrated. The details of the newly developed mass transfer function are published in March et al. (2018).

Additional modeling of a single rock matrix block showed that spontaneous imbibition is the process governing mass transfer during the post-injection phase when CO_2 is swept from the fractures due to regional migration. The mass transfer due to spontaneous imbibition has two distinct regimes: an early diffusive regime and a late exponential regime. While separate models exist for the two regimes, the contribution of this project is in combining the regimes by determining an appropriate transition time. This transition time is the time where the solution starts to deviate from the diffusion solution and can be calculated based on rock parameters. Details of this hybrid mass transfer function can be found in March et al. (2016).

The mass transfer functions described above are for mass exchange of free-phase CO_2 and brine. However, mass may also be exchanged through migration of dissolved CO_2, especially in reservoirs with low permeability rocks. For exchange of dissolved CO_2, the mass transfer is governed by solute diffusion into matrix blocks. Infinite-series solutions already exist for some block geometries for early and late-time behavior, but they are computationally intensive. Therefore, a simplified, unified model was developed that describes diffusion into blocks of different geometries (e.g., spheres, slabs, rectangular parallelepipeds) by combining models of early and late-time behavior. The appropriate switch-over time depends on the block geometry and was found through numerical experiments. The main simplification approach was significantly reducing the number of terms of the infinite-series solutions; this simplifications leads to a maximum relative error of less than 0.2% for the cases tested. Details on the new solutions can be found in Zhou et al. (2017b) and Zhou et al. (2017a).

Implement new mass transfer functions into simulators: The two newly developed mass transfer functions for free-phase CO_2 and brine were implemented in the reservoir simulator Matlab Reservoir Simulation Toolbox (MRST). MRST is open-source and publically available. The dual porosity capability with the newly developed mass transfer functions has been part of the standard MRST release since version 2017a (www.sintef.no/mrst).

The diffusive transfer function for dissolved CO_2 storage was used to guide the local refinement of matrix blocks with the Multiple Interacting Continuum (MINC) model used in TOUGH2. This implementation enhanced modeling accuracy and efficiency. For TOUGH2 modeling of free-phase CO_2 storage, a revised MINC model was introduced to account for matrix-matrix connectivity and buoyancy-driven flow.

In addition to increasing the capabilities of exiting simulators, a vertically-integrated multi-phase flow modeling approach for fractured storage reservoirs was developed. This modeling approach takes advantage of the high permeability of the fractures, which leads to a rapid vertical segregation of CO_2 and brine. Therefore, the so-called vertical equilibrium assumption is likely to be valid, allowing the two-phase flow in the fractures to be modeled using a vertically-integrated, vertical-equilibrium approach. The vertical saturation and pressure profiles in the fractures are calculated based on the results of the vertically-integrated equations. These profiles are needed to calculate the spatially distributed mass transfer between fractures and the rock matrix. The rock matrix is conceptualized in three different ways: “sugar cubes” with no fluid migration from a rock matrix block to its neighbors and no fluid migration within a block, “match sticks” with vertical fluid migration within a block, but no migration to neighboring blocks, and “dual-permeability” where fluid migration occurs both in the fractures and the rock matrix. More details on the vertically-integrated approach for fractured reservoirs can be found in Tao et al. (2018).

Application of site-scale models and sensitivity analysis: Several site-scale sensitivity analyses have been conducted to investigate geologic carbon storage in fractured reservoirs. One such study looked at the impact of vertical capillary bridges on storage capacity of the rock matrix by using highly resolved numerical modeling. The study found that capillary bridges can significantly increase storage capacity. Another study compared CO_2 injection into unfractured and fractured anticlines, and showed that less CO_2 is stored in a fractured reservoir, because the high permeability of the fractures led to earlier migration out of the anticline (March et al., 2018). The same study also found that the density difference between CO_2 and brine plays an important role in determining the storage capacity of the rock matrix, with higher density difference (i.e., lower CO_2 density) leading to higher relative storage capacity. A study of the impact of injection rate on storage capacity found that the fracture-rock mass transfer rate is an important factor for the relative partitioning of CO_2 between fractures and rock matrix (March et al., 2017). A study of storage capacity due to diffusion of dissolved CO_2 into the rock matrix showed that about twice as much dissolved CO_2 can be stored in the rock matrix than free-phase CO_2 is stored in the fractures for a fracture spacing of around 2 m or less (Zhou et al., 2017b). Fracture spacing, porosities of fractures and rock matrix, CO_2 and brine densities, and CO_2 solubility were found to be important parameters to determine the ratio between fracture and matrix storage.

Modeling at the In Salah site: The revised MINC model with matrix-matrix connectivity was used to simulate CO_2 storage at the In Salah site. The focus was on CO_2 injection at injection well KB-501. The modeling results show the coupling between fast migration of free-phase CO_2 in the fracture continuum and massive CO_2 storage in the rock matrix. Sensitivity analysis shows that the dynamic fracture-matrix interactions depend on fracture spacing, matrix permeability, and matrix capillary pressure function.

2 Report Details

2.1 Introduction

Carbon capture and storage (CCS) is a climate change mitigation technology, where CO_2 is captured from large anthropogenic sources, such as coal-fired power plants and ethanol production facilities, instead of being emitted to the atmosphere (Metz et al., 2005). The captured CO_2 is then injected into the subsurface for permanent storage; this is termed geologic carbon storage (GCS). Deep saline aquifers are being considered as the most likely choice of GCS, due to their large storage capacity and wide spatial distribution. CO_2 needs to remain in the storage formation for hundreds or thousands of years for CCS to be an effective climate change mitigation option. Storage formations are chosen to be deep enough so that the ambient pressure and temperature conditions are such that CO_2 is in its supercritical state, with a density of a liquid instead of a gas. Density of supercritical CO_2 is on the order of 500 – 750 kg/m^3, which is lower than that of the resident saline water at 1000 – 1300 kg/m^3. This means that the injected CO_2 has an upward drive due to buoyancy and migrates upward unless it is trapped by a low-permeability barrier (stratigraphic trapping) or other trapping mechanisms (capillary trapping, solution trapping, mineral trapping). Therefore, formations that prevent vertical CO_2 migration due to their low permeability – termed caprocks – are an important feature of GCS sites.

The majority of the formations currently being considered as GCS sites are mainly comprised of sandstone, due to sandstones high porosity and permeability. However, carbonate formations are increasingly being investigated as potential storage targets as well. One major difference between sandstone and carbonate formations is that carbonate formations tend to be fractured, while sandstone formations tend to consist of continuous rock. In the context of GCS, fractures can play an important role, as the fractures have a higher permeability than the rock matrix. Therefore, lower injection pressures are required to inject CO_2 into the storage formation. However, the void spaces of the fractures are small compared to that of overall rock volume, because the fractures are very thin. This means that the CO_2 plume needs to stretch out over a longer distance to accommodate the same volume of CO_2. This has a negative impact on storage safety, as the larger spread increases the likelihood of CO_2 encountering a leakage pathway through the caprock (e.g., abandoned wells, faults). However, CO_2 not only reside in the fractures, it also migrates into the rock matrix. Free-phase CO_2 migrates into the rock matrix mainly due to gravity and capillary forces, while dissolved CO_2 migrates by diffusion. From the perspective of storage safety, migration into the rock matrix is beneficial, because there is much more storage capacity in the rock matrix than in fractures, thus reducing the horizontal spread of the plume. Also, CO_2 is less mobile once it is in the rock matrix, due to the lower permeability of the rock matrix compared to the fractures. This means that the interaction of flow between fractures and rock matrix needs to be well understood to determine storage capacity and storage safety of fractured storage reservoirs.

Numerical modeling is an important tool for predicting the migration of CO_2 and brine in the subsurface. These models are based on the governing equations of multi-phase flow in porous media. The governing equations consist of mass balance equations for CO_2 and brine, Darcy's law fluxes for CO_2 and brine, and constitutive relationships for fluid density and viscosity, as well as relationships that relate fluid saturation to capillary pressure and relative permeability. Due to the complexity of the governing equations and the complexity of domain geometry, the governing equations often need to be solved numerically. The domain is discretized into cells to find the numerical solution to the governing equations. The presence of fractures and the interaction between fractures and the rock matrix complicate modeling of CO_2 storage. In order to directly capture the flow of CO_2 and brine from the fractures into the rock matrix, the model domain needs to be very finely resolved, with grid spacing at the millimeter scale and below. However, questions related to storage capacity and storage safety are usually answered at the site or regional scale (i.e., length scales of hundreds of meters to hundreds of kilometers). The computational effort involved in running such large modeling domains with very fine spatial resolution is prohibitive, so that simplified approaches are necessary. One such simplified approach is the dual-continuum approach, where fractures and rock matrix are conceptualized as two separate continua (Figure 1). The interaction of fractures and rock matrix are represented by mass transfer functions, which couple the two continua. The dual-continuum approach has been successfully applied to hydrocarbon reservoir modeling for several decades. The dual-continuum approach typically requires well-connected fracture networks that satisfy the continuum hypothesis on appropriate length scales. Given the large length scales involved in GCS modeling, continuum models are likely to be reasonable choices.

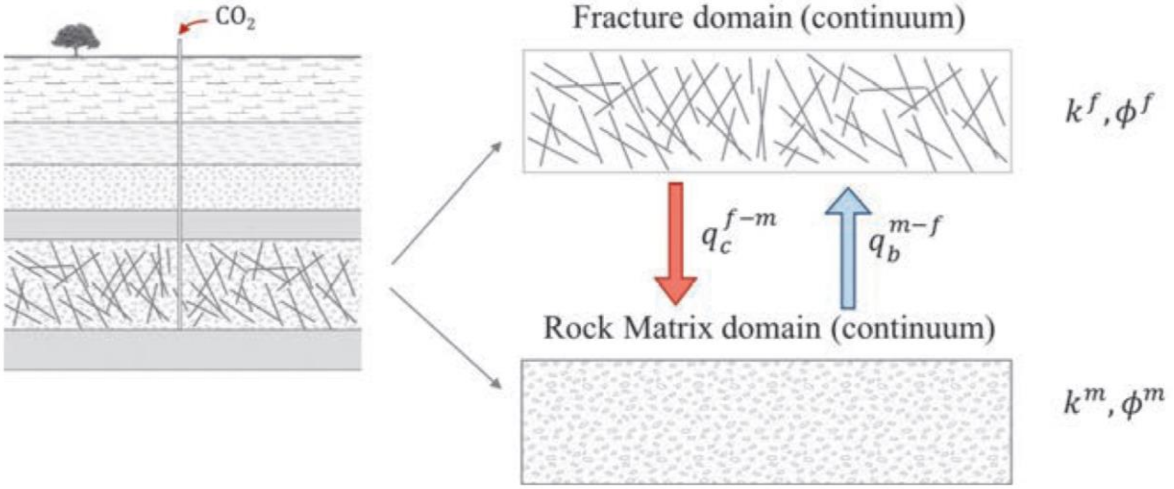

Figure 1: Conceptualization of the dual-continuum approach with the fracture continuum and rock matrix continuum connected through mass transfer terms q_c and q_b. Taken from Guo et al. (2017).

The fracture continuum is generally conceptualized as a continuous domain and is modeled as a porous medium with high permeability and low porosity. However, there are several different conceptualization of the rock matrix continuum (Figure 2). The most common approach is to conceptualize the rock matrix as a set of unconnected blocks; this conceptualization is termed the dual-porosity approach. The sugar cube model is one such dual-porosity approach and was originally developed by Warren and Root (1963) and later extended for multiphase flow by Kazemi et al. (1976), among others. This approach conceptualizes the rock matrix as identical rectangular parallelepipeds with homogeneous and isotropic rock properties. Those matrix blocks, which are often referred to as "sugar cubes," are not connected to each other and they only exchange fluids with fractures. As a result, the rock matrix effectively serves as a source or sink for fluids that flow in the fractures. The so-called Multiple Interacting Continua (MINC) approach (Pruess & Narasimhan, 1985) is a sugar cube variant where each sugar cube consists of multiple sub-domains nested within each other, akin to the concept of Russian nesting dolls. The outermost sub-domain interacts with the fracture continuum and the first sub-domain; the other sub-domains interact with the two neighboring sub-domains that either encloses this sub-domain or is enclosed by this sub-domain. In this manner flow from the edges to the center of the sugar cube can be modeled.

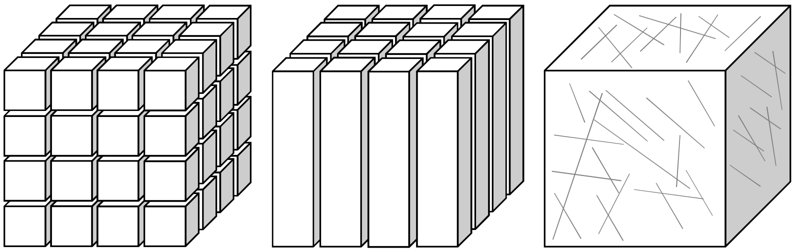

Figure 2: Schematic graphs showing the rock matrix conceptualizations of the three models: Dual-porosity sugar cube model (left), dual-porosity matchstick model (middle), and dual-permeability model (right). Taken from Tao et al. (2018).

Gilman and Kazemi (1988) extended the sugar cube model and developed the dual-porosity matchstick model, in which the rock matrix is conceptualized as a collection of vertical columns separated by vertical fractures through the entire thickness of the geological formation. The dual-porosity matchstick model allows vertical flow in the matrix continuum, but no flow from matchstick to matchstick. From a modeling perspective this means that there are now multiple flow systems – one in the fractures and one in each matchstick – and the flow systems are coupled through the mass transfer functions.

In the third conceptualization of rock matrix blocks, termed dual-permeability approach (Barenblatt et al., 1960), flow occurs in the rock matrix, as well as in the fractures. In other words, the rock matrix forms a continuum, just like the fractures. Two multi-phase flow systems need to be solved – one for the fracture continuum and one for the rock matrix continuum – and the two flow systems are coupled through mass transfer functions.

Mass transfer functions are based on the physical processes that led to mass exchange between fractures and rock matrix. For instance, capillary forces will draw a wetting fluid from the fractures into the rock matrix, if the rock matrix is occupied by the non-wetting fluid and the fractures are filled with wetting fluid, because the pore spaces in the rock matrix are usually much smaller than those in the fractures. Gravity is another important driver for mass exchange, as a less dense fluid will replace a denser liquid, if the rock matrix is filled with the denser fluid, while the surrounding fractures are filled by the less dense fluid. If the fluids contain dissolved constituents, mass exchange between fractures and the rock matrix may occur due to diffusion along concentration gradients. Other mechanisms, such as compressibility, may also lead to mass exchange, but are not expected to be relevant for mass exchange between fractures and rock matrix in the CO_2-brine system.

While the dual-continuum approach has been used extensively in hydrocarbon reservoir modeling and contaminant flow and transport modeling, it has not been applied to systems comprised of CO_2 and brine. In order to adapt existing dual-continuum approaches to GCS modeling, new mass transfer functions need to be developed, and this is one of the main accomplishments of this project. Mass transfer functions are developed for both free-phase and dissolved CO_2. The developed mass transfer functions are then implemented into existing and newly developed simulators, to achieve the second main goal of this project, which is to investigate storage reservoir properties and operational parameters beneficial to GCS.

In this report we first discuss the newly developed mass transfer functions for the CO_2-brine system for the following three conditions: mass exchange due to gravity during the CO_2 injection phase, mass exchange due to capillary forces during the post-injection phase, and mass exchange due to diffusion of dissolved CO_2 into the rock matrix. The report then describes the implementation of the mass transfer functions into the existing simulator MRST and the newly developed library SHPALib, as well as the development of a dual-continuum vertically-integrated modeling approach. The updated/new simulators are then used to investigate conditions that are favorable for storage capacity and storage safety. Lastly, the impact of fractures on CO_2 migration at the In Salah site with its fractured storage reservoir is investigated.

2.2 Development of mass transfer functions for CO_2 – brine system

This section describes three newly developed mass transfer functions for the interactions between fractures and the rock matrix in reservoirs occupied by CO_2 and brine. The first mass transfer function represents conditions during the injection phase, with high CO_2 saturation in the fractures and initially no CO_2 in the rock matrix. In this case, gravity of brine from the rock matrix is the most important driver for fracture – rock matrix interaction. The second mass transfer function is developed to represent the post-injection phase, when free-phase CO_2 has migrated away from the injection site (e.g., due to regional groundwater flow or caprock topography), so that the CO_2 saturation in the fractures is low and the initially CO_2 saturation in the rock matrix is high. Spontaneous imbibition is the driver for mass exchange here, because brine, as the wetting fluid, displaces CO_2 in the rock matrix. These two mass transfer functions are both cases where free-phase CO_2 migrates into or out of the rock matrix. However, high capillary entry pressure or low permeability of the rock matrix may prevent free-phase CO_2 from entering the rock matrix. Even if free-phase CO_2 is excluded from entering the matrix, CO_2 at the fracture – matrix interface can dissolve into brine. Therefore, a third set of mass transfer functions is developed, that is based on diffusion of dissolved CO_2. The development and application of the three newly developed mass transfer functions is discussed below.

2.2.1 Mass transfer function for free-phase CO_2 during injection phase (gravity drainage)

The key achievements discussed in this section are the identification required corrections of time-scales for gravity drainage when the considered fluids are supercritical CO_2 and brine rather than natural gas and oil. Further it illustrates that through appropriate design of injection rate protocols the fraction of CO_2 that resides in fractures and matrix respectively can be altered. Material properties and dominant processes in CO_2 storage differ from the ones in conventional production environments. Simplifying hypotheses that are commonly made in existing transfer functions lead to inaccurate results in the context of CO_2 storage. A transfer function for buoyancy displacement based on the timescale of the one-dimensional equation for immiscible two-phase flow in porous media is developed (March et al., 2018) and compared to current existing mass transfer functions with simple matrix-block geometries. The results are evaluated against high-resolution numerical simulations of matrix blocks considering realistic physical properties of CO_2-brine systems and fractured rocks. Figure 3 (top) compares the transfer of CO_2 into the matrix block from a high-resolution simulation, from the novel time-scale estimates and from the most accurate model available in the literature (Di Donato et al., 2006). The model by Di Donato et al. (2006) assumes infinite mobility of the CO_2 phase. This assumption is worse the lower the end-point relative permeability values are. Figure 3 (top) confirms this by showing three cases with different values of endpoint CO_2 relative permeabilities. While the mismatch between the high-resolution model and Di Donato et al. (2006) increases, the newly developed model performs equally well under the three scenarios. Figure 3 (bottom) shows reconstructed profiles based on the newly developed model and the numerical solution at an intermediate time. Also shown is the equilibrium distribution. The results confirm that in all three cases the reconstruction matches reasonably well with the high-resolution model and hence achieving good performance.

The transfer functions are also implemented in a dual-porosity simulator and different CO_2 injection scenarios are tested. An ideal operation would maximize the amount of CO_2 in the matrix and minimize the spreading of the plume in the fracture system. Figure 4 illustrates the amount of CO_2 stored in total and in the matrix and fracture continua respectively in an idealized rectangular reservoir for a set of injection scenarios that use variable injection rates. Three scenarios are investigated that all inject the same amount of CO_2 (400 m^3) in three different schedules. In the Base Case, the injection rate is set to a constant rate of 50 m^3/d for 8 days. The other two cases, Injection Scenario 1 and Injection Scenario 2, consist of injecting 3/4 of the total amount of CO_2 available for injection at higher initial rates (200 m^3/d and 400 m^3/d, respectively) and then injecting the remaining 100 m^3 in the time left to complete the 8 days of injection. The results show that the constant injection scenario is the one that provides the smallest amount of CO_2 in the matrix at all times. As the initial injection rate increases, so does the amount of CO_2 in the matrix along the injection time. In fact, the shape of the CO_2 plume in the fracture system is the result of an interplay between viscous and buoyancy forces, the first governed by the injection rate and the second by the density difference between both phases. Changing flow rates also change the profile of the buoyant CO_2 plume in the fracture system, which activates a wider region for transfer. The final saturation profiles in the matrix (Figure 4b) shows that the matrix retains a history of the previous locations visited by CO_2. Although the final plume sits at the top of the formation, as a result of a dominant buoyant force, the initial high rates increased the area spanned by the plume and hence the effective transferred amount of CO_2. For more details on the newly developed mass transfer function the reader is referred to March et al. (2018).

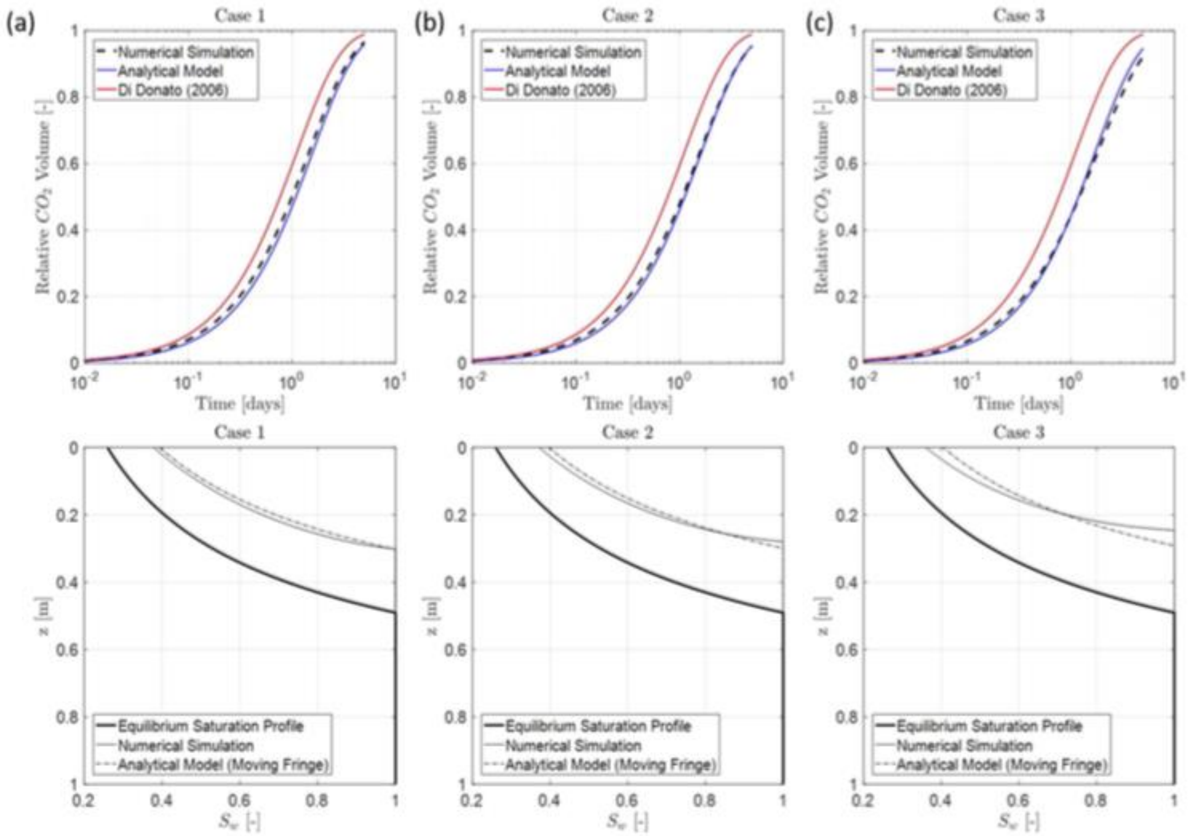

Figure 3: Stored CO_2 volume relative to the equilibrium storage volume (top) and reconstructed saturation profile (bottom) for different end-point values of the relative permeability to CO2 (a) Case 1: $k_{rn}(S_w = 0) = 1$, (b) Case 2: $k_{rn}(S_w = 0) = 0.6$ and (c) Case 3: $k_{rn}(S_w = 0) = 0.3$. Taken from March et al. (2018).

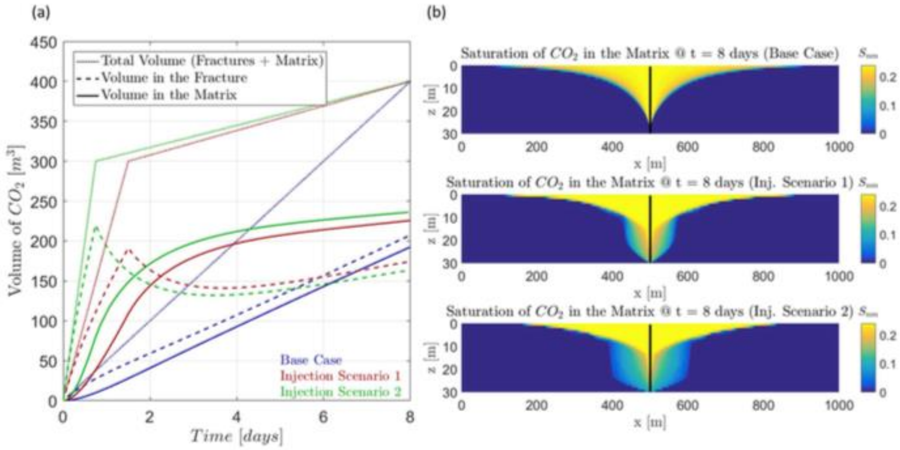

Figure 4: (a) Volumes of CO_2 in the system for different injection scenarios. (b) Final saturation cross-section in the matrix for the Base Case (top), Injection Scenario 1 (middle) and Injection Scenario 2 (bottom). Taken from (March et al., 2018).

2.2.2 Mass transfer function for free-phase CO_2 during post-injection phase (spontaneous imbibition)

In this section the development of a new physically based model for spontaneous imbibition is discussed (March et al., 2016). The model captures transition from early-time to late-time imbibition and it has been validated for different applications.

Spontaneous countercurrent imbibition into a finite porous medium is an important physical mechanism for many applications, included but not limited to CO_2 storage, oil recovery and irrigation. Symmetry considerations that are often valid in fractured porous media allow us to study the process in a one-dimensional (1D) domain. In 1D, for incompressible fluids and homogeneous rocks, the onset of imbibition can be captured by self-similar solutions and the imbibed volume scales with $\sqrt{t}$. At later times, the imbibition rate decreases and the finite size of the medium has to be taken into account. This requires numerical solutions. Figure 5 illustrates the solution of such a numerical simulation. Figure 5a shows the saturation profile at three different times while Figure 5b shows the total amount of imbibed fluid as a fraction of the pore space. The results shows the $\sqrt{t}$-based solution at early times and the deviation from it at later times. Note, however that the $\sqrt{t}$ behavior lasts substantially longer than the time it takes for the imbibition front to reach the boundary.

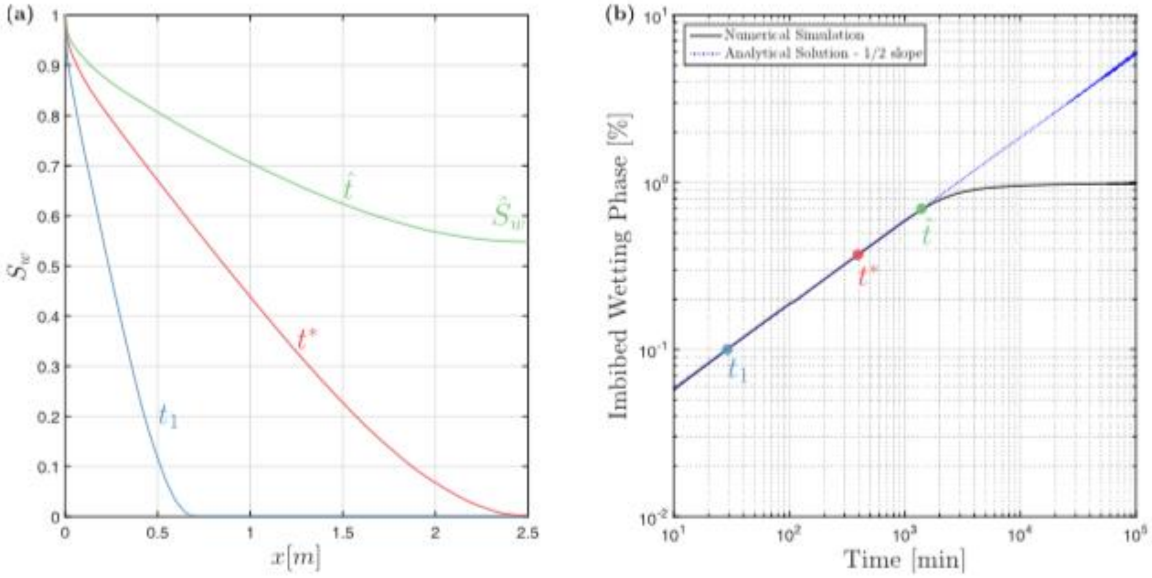

Figure 5: Illustrative example of a high-resolution simulation of an imbibition process into a dry domain. (a) Saturation profiles at different times, and (b) a log-log plot of the imbibed volume fraction. The instants of the three profiles are marked by filled circles. Taken from March et al. (2016).

A new approach was developed to approximate the whole imbibition process semi-analytically including the transition from early to late time. The onset is captured by a semi-analytical solution and an a priori estimate can be made for the time until which the imbibed volume scales with √t. This requires the construction of an approximate solution which is illustrated in Figure 6. The semianalytical solution into a semi-infinite domain is truncated at boundary of cell while filling back the amount of fluid that has left the domain and adding it to the profile to construct a plateau. The remainder of the imbibition process is obtained from a self-similarity solution. The new approach is tested against numerical solutions that employ parametrizations relevant for oil recovery and CO_2 sequestration. The concept improves common first-order approaches that heavily underestimate early-time behavior and it should be noted that it can be readily included into dual-porosity models. Figure 7 illustrates the comparison between reconstructed solutions and the high resolution numerical solutions. While the early time solution is exact by construction the late time behavior shows some mismatch. The difference originates in the nonlinear nature of the diffusion process and the fact that for certain petrophysical parameter the first order approximation does not work even for late times. Further discussions on these difference and other details are presented in March et al. (2016).

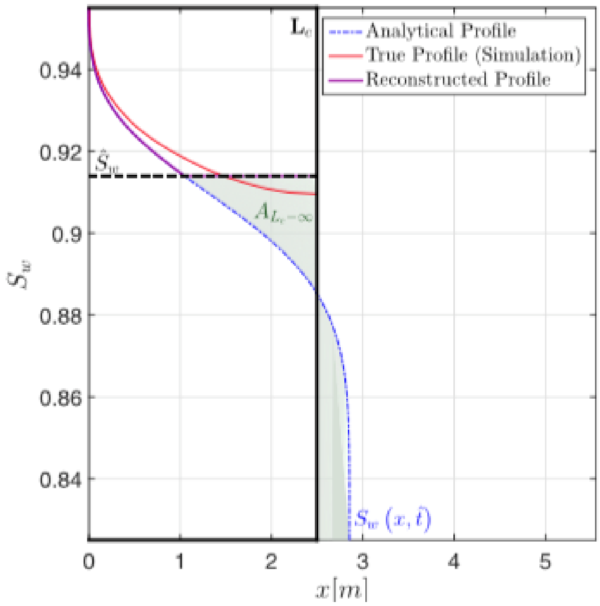

Figure 6: Comparison between the reconstructed saturation profile (purple curve) and the true saturation profile given by high-resolution one-dimensional simulation (red curve). The analytical solution for imbibition into an infinite domain is shown as blue dash-dotted curve. The volume A_L of the analytical solution that left the boundary and has been "filled back" is also shown. Taken from March et al. (2016)

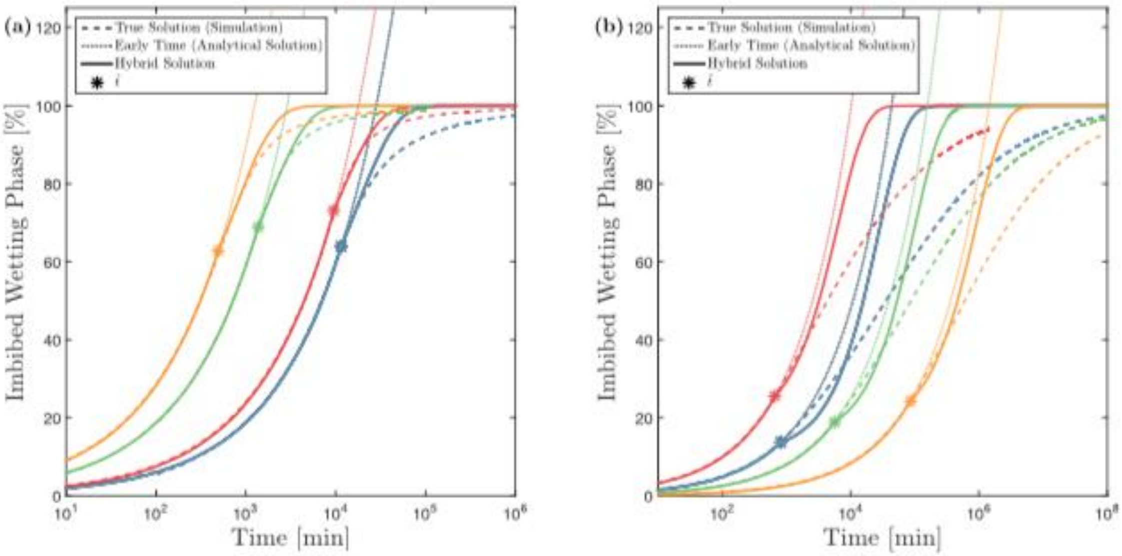

Figure 7: Representative curves for the imbibed volume percentage for (a) high values of μ and σ; (b) low values of μ and σ. Taken from March et al. (2016)

2.2.3 Mass transfer function for dissolved CO_2 (diffusion)

In the case of fractured reservoirs with matrix blocks of low permeability and high entry capillary pressure, injected supercritical CO_2 ($scCO_2$) migrates through fractures and $scCO_2$ dissolves at fracture-matrix interfaces. The dissolved CO_2 (dCO_2) diffuses into the matrix blocks for storage, leading to solubility trapping in fractured reservoirs. Traditional dual-porosity models underestimate the time-dependent storage efficiency of $dsCO_2$.

An analytical solution was developed to calculate the diffusive flux of dCO_2 into matrix blocks of different shapes, sizes, and rock properties. The diffusive flux equation developed is of the same functional form (i.e., three-term polynomial solution for the early-time diffusion regime and exponential solution for the late-time regime) for any regular block shapes (slab, rectangle, rectangular parallelepiped, sphere, cylinder), while the six solution coefficients depend on block shape and aspect ratios for two-dimensional and three-dimensional rectangular blocks (Zhou et al., 2017a; Zhou et al., 2017b).

The diffusive flux equation for isotropic and anisotropic matrix blocks can be written:

$$M_d = \begin{cases} a_1 t_d^{1/2} + a_2 t_d + a_3 t_d^{3/2} + O(\text{ierfc}),\ t_d < t_{d0} & \text{(1a)} \\ \\ 1 - \sum_{j=1}^{N} b_{1j} \exp\left(-b_{2j} t_d\right),\ \ t_d \geq t_{d0} & \text{(1b)} \end{cases}$$

where M_d is the dimensionless cumulative flux or block-average dimensionless mass fraction of dCO_2 in the matrix block, t_d is the dimensionless time, t_{d0} is the switchover dimensionless time, a_1, a_2, a_3, b_1, b_2 are the first-order solution coefficients, $O(\text{ierfc})$ are the higher-order terms that represent multiple reflections, and N is the number of truncated exponential terms.

The solution coefficients for a rectangular parallelepiped can be written as:

$$a_1 = 2(1 + R_{l2} + R_{l3})/\sqrt{\pi},\;\; a_2 = -4(R_{l2} + R_{l3} + R_{l2}R_{l3})/\pi,\;\; a_3 = 8R_{l2}R_{l3}/\pi^{3/2} \tag{2a}$$

$$b_{1j} = \left(\frac{8}{\pi^2}\right)^3 / \left[(2n_{1j}-1)^2(2n_{2j}-1)^2(2n_{3j}-1)^2\right] \tag{2b}$$

$$b_{2j} = \frac{\pi^2}{4}c_j;\; c_j = \left((2n_{1j}-1)^2 + \left(2n_{2j}-1\right)^2 R_{l2}^2 + \left(2n_{3j}-1\right)^2 R_{l3}^2\right) \tag{2c}$$

where R_{l2} and R_{l3} are the aspect ratios, whose values are between 0 and 1. The six solution coefficients for other shapes of matrix blocks are given in Zhou et al. (2017a) and Zhou et al. (2017b).

The development of equation (1) was based on two classic solutions to matrix blocks with different isotropic shapes (slab, cylinder, and sphere): (1) infinite-series exponential solutions with $N = \infty$ in equation (1b), and (2) the first-order error-function solutions with truncated higher-order terms. These fundamental solutions are available in the classic heat conduction book by Carslaw and Jaeger (1959) and the diffusion book by Crank (1975). The exponential series converges very fast in the late-time diffusion region (see Figure 8a) while the error function series converges very fast in the early-time regime. The truncated series of both solutions are combined, resulting in a continuous-in-time solution with a switchover time, and the switchover time for each block shape was determined to minimize the maximum approximation error (see Figure 8b). For isotropic matrix blocks (slab, cylinder, and sphere), the solution in equation (1) with $N = 1$ has an approximation error of less than 0.2% (Zhou et al., 2017b).

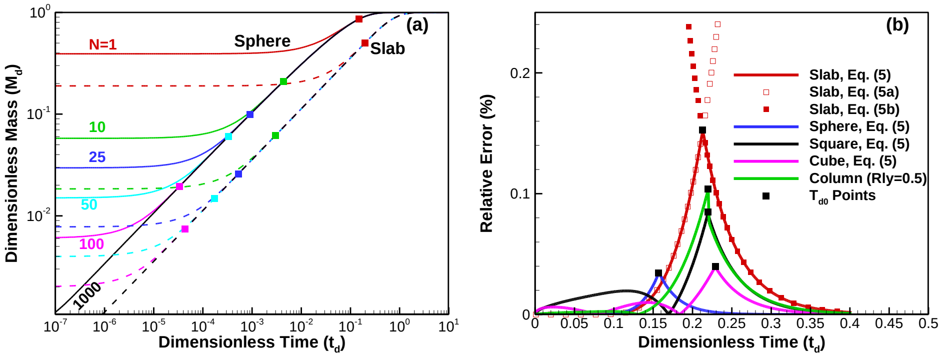

Figure 8: (a) Convergence behavior of the exponential-series solution for slab and sphere, and (b) approximation error of equation (1) for slab, sphere, cube, and square (modified from Zhou et al. (2017b))

For two- and three-dimensional rectangular matrix blocks (square, cube, rectangles, and rectangular parallelepiped) formed by 2 and 3 sets of orthogonal fractures respectively, the infinite-series exponential solutions are available in the literature, but the error-function solutions are not available. The exact exponential solutions to equation (1a) are fitted by assuming that equation (1) is common for any shapes of matrix blocks, and that a_1, a_2, and a_3 are obtained with the same form as equation (2a) and numeric for the π terms (Zhou et al., 2017b). The three solution coefficients are then derived analytically in terms of aspect ratios as shown in equation (2a) (Zhou et al., 2017a). The exact and approximate solutions are calculated for six R_{l2} values for two-dimensional rectangular blocks, and for a number of (R_{ly}, R_{lz}) pairs for rectangular parallelepipeds, with an increment of 0.1 and $0 \leq R_{l2} \leq 1$ and $0 \leq R_{l3} \leq R_{l2}$ for the range of $1.0 \times 10^{-7} \leq t_d \leq 0.2$. As shown in Figure 9 for the comparison between the exact exponential solutions and the approximate solutions in equations (1-2), the approximation error is very small, at less than 0.2%.

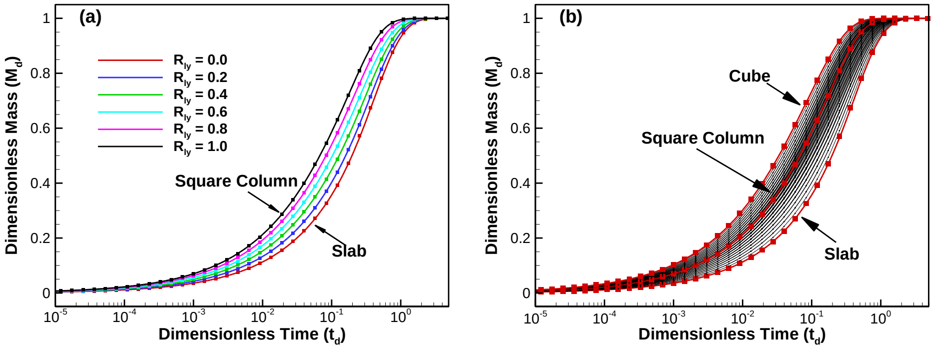

Figure 9: (a) Comparison between the approximate solutions (in symbols) and the exact solutions (in solid lines) for a two-dimensional rectangular block as a function of the aspect ratio R_{l2}, and (b) comparison between the approximate solutions (in black symbols) and the exact solutions (in black solid lines) for a rectangular-parallelepiped block, as a function of the aspect ratios R_{l2} and R_{l3} (modified from Zhou et al. (2017b)).

The diffusive flux equation above and its associated memory function in the Laplace domain, as well as global transfer functions for solute transport, were coded into a Fortran package, referred to as SHPALib (Solute and Heat Transport and Pressure Propagation: An Analytical Solutions Library) (Zhou et al., 2019c).

2.3 *Implementation of mass transfer functions in simulators*

The newly developed mass transfer functions were implemented in existing simulators. A CO_2-brine dual-porosity module was developed for the MATLAB Reservoir Simulation Toolbox (MRST) as part of this project. The module includes mass transfer functions for gravity drainage and spontaneous imbibition and is now part of the regular distribution of MRST. MRST is freely available at the SINTEF website (www.sintef.no/projectweb/mrst/). The mass transfer function based on diffusion of dissolved CO_2 was implemented in the Fortran package SHPALib (Solute and Heat Transport and Pressure Propagation: An Analytical Solutions Library). Access to the library will be granted by Lawrence Berkeley National Lab on a case by case basis. In addition, a new modeling approach was developed as part of this project, coupling a vertically-integrated modeling approach with the dual-continuum concept, so that the fracture continuum is represented by a vertically-integrated model, while the rock matrix is represented by a conventional three-dimensional model. The new modeling approach takes advantage of the high permeability of fractures leading to fast vertical segregation of CO_2 and brine. Therefore, the so-called vertical equilibrium assumption, which is often invoked in vertically-integrated modeling approaches, is likely valid in the fracture continuum. Reconstruction of vertical pressure and saturation profiles, which are necessary to solve the vertically-integrated governing equations and compute mass transfer between fractures and the rock matrix, requires relatively little computational effort, which means that vertically-integrated reservoir simulators are generally much more computationally efficient than conventional three-dimensional reservoir simulators.

2.3.1 Implementation in MRST

Within the project a dual-porosity module was developed and implemented in MRST. MRST is an open-source platform to prototype and develop reservoir simulation algorithms and modeling concepts. Many different approaches of using MRST are possible ranging from using it as a standard reservoir simulator to a scripting environment with various useful routines that can be combined together as needed. It is built with a very slim core and additional features/routines are incorporated as modules. The toolbox is implemented in Matlab, but through the Matlab MEX functionality external routines (in C, C++ or Fortran) can be compiled and plugged into the code for increased performance.

MRST's basic grid structure is fully unstructured with nodes defining faces and faces defining cells, allowing full flexibility in the grid representation. Even Cartesian and corner-point grids are treated as unstructured grids. Hence, an arbitrary mesh refinement is always possible as long as the discretization concept allows for it. Most process-focused modules (such as the Black-Oil model) are thoroughly tested and implemented based on finite volume discretization together with two-point flux approximation (TPFA), but other discretizations such as mimetic finite differences, virtual elements and multi-point flux approximation are available as well and can be adapted.

MRST is implemented as a flexible object-oriented environment, and with a high level of modularity that allows easy reusability of code. The main element of the object oriented approach is an automatic differentiation (AD) framework (Krogstad et al., 2015) that allows for fully implicit rapid prototyping and model-based and equation-based programming.

Physical models are implemented in a model class. Any model class in MRST is inherited from a parent interface called *PhysicalModel*. A class diagram that outlines the model concept in MRST is presented in the left of Figure 10 for a basic two-phase flow model that is inherited from the *ThreePhaseBlackOilModel* which is inherited from the *ReservoirModel* which is inherited from the *PhysicalModel*. The class *ReservoirModel* extends class *PhysicalModel* and provides functionality that is specific to models relevant to reservoir simulation. This class has two important attributes: the fluid and the rock structures. These structures define fluid properties, such as viscosities and densities, and rock properties, such as porosity, permeability, relative permeabilities and capillary pressures. Saturation-dependent petrophysical functions are defined as function handles. This class also calls *setupOperatorsTPFA*, that calculates transmissibilities using the two-point flux approximation (Krogstad et al., 2015). Model-specific classes such as *ThreePhaseBlackOilModel* and *TwoPhaseOilWaterModel* implements the equations that are specific to these models. In our dual-porosity module, these equations are extended by another set of conservation equations for the matrix, and source terms that model the transfer. We have introduced a class named *DualPorosityReservoirModel* that defines extra structures for holding matrix properties, as well as extra variables to represent saturations and pressures of the matrix (see right part of Figure 10). This class also has a variable that holds a generic instance of a transfer function that represents the generic concept of a transfer model between the continua. The *TransferModel* interface defines a dummy method that is called by all the derived classes: *calculateTransfer*. This method receives structures containing matrix and fracture fields and calculates the transfer for all phases. As shape factors are a research topic by themselves the module provides a generic *ShapeFactor* interface with a method *calculateShapeFactor* that can be overloaded with specific models for the shape factor. We also provide several traditional transfer functions (e.g., Kazemi et al. (1976) and Gilman (1986)) and shape factors (e.g., Coats (1989) and Lim and Aziz (1995)) in the dual-porosity module. Further details are available in March (2018) or in the dual-porosity module of MRST.

Figure 11 illustrates the solution of a two-phase test case of the module. It models a quarter five spot problem of water flooding using the Kazemi shape factor and the standard Eclipse transfer function. The example illustrates how the water saturation in the matrix lacks behind the saturation in the matrix and how the water transfer rate is the negative of the oil transfer rate due to the incompressibility assumption. The script that runs this example is provided in Appendix 6.2. Further examples are included in the MRST module folder.

Figure 12 shows a comparison of the CO_2 plumes in the fracture and matrix continua after 120 years of injection into the Johanson formation using the transfer function developed in this project (left) and a conventional transfer function (right). The case is discussed in greater detail in March (2018).

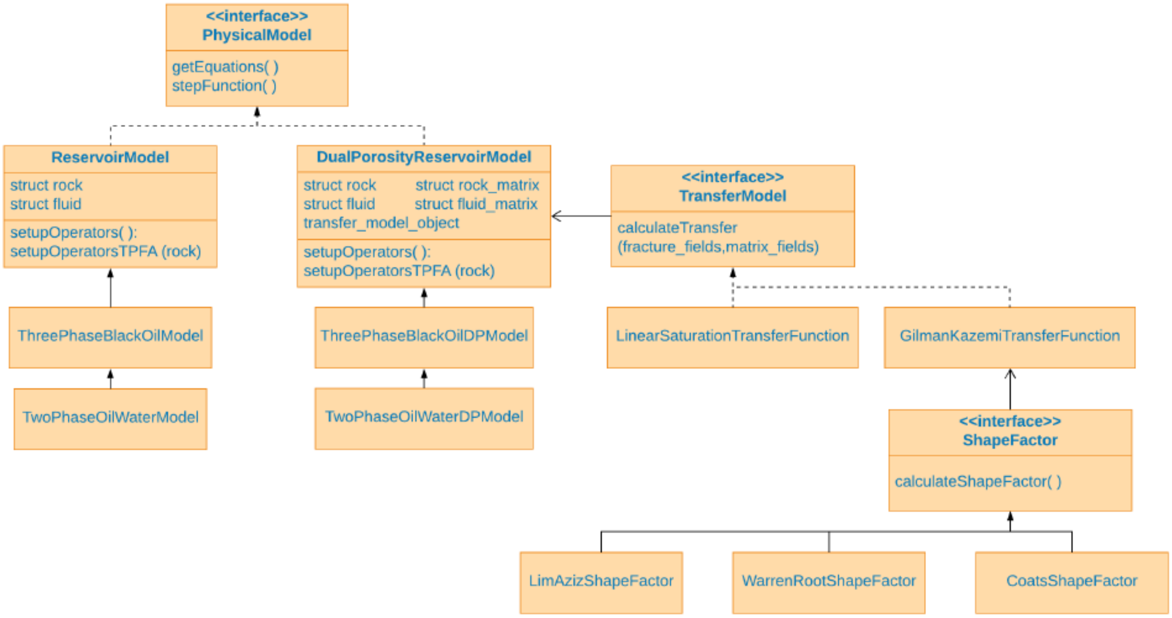

Figure 10: Simplified class diagram of the model structure of MRST with the dual-porosity module. Taken from March (2018).

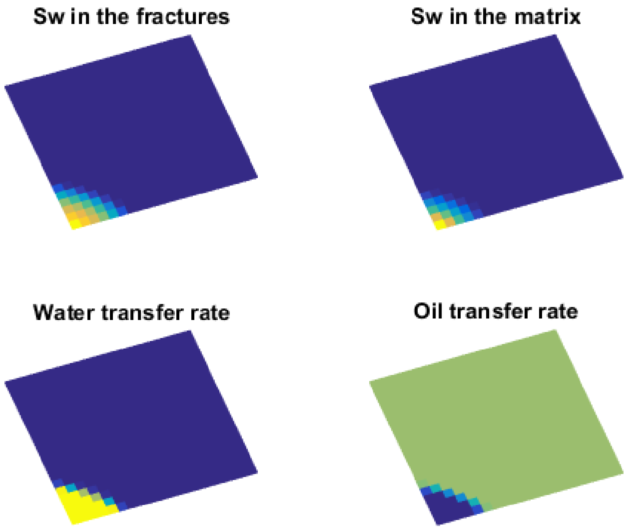

Figure 11: Illustration of a solution of the dual-porosity simulator. The panels show the solution of a quarter five spot problem for water flooding.

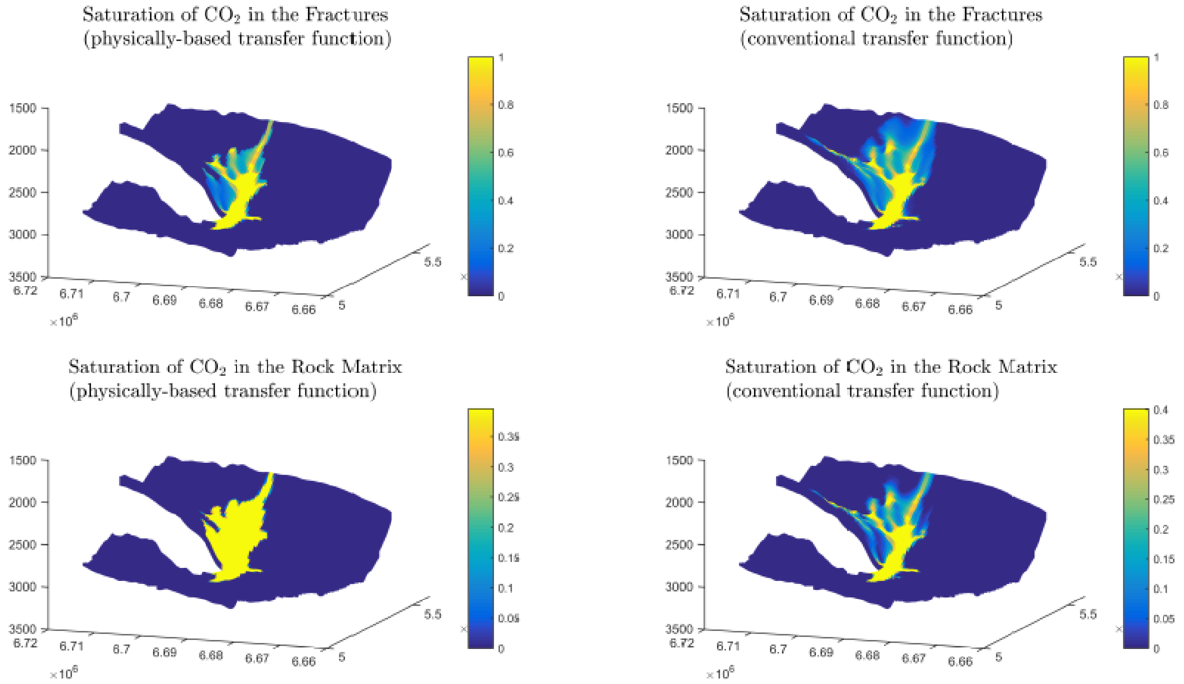

Figure 12: CO_2 plumes in the fracture and matrix continua after 120 years of injection using the physically-based transfer function (left) and the conventional transfer function (right) using the dual-porosity module of MRST. Taken from March (2018).

2.3.2 Implementation of SHPALib

The developed diffusive flux equation in equations (1a-b) and (2a-c) was coded in a FORTRAN subroutine file, ZhouAnaModels_2DiffusiveFlux_SolutionSubs.f90. This file includes three subroutines for calculating concentration inside a matrix block, three subroutines for calculating cumulative mass flux, and three subroutines for calculating transient mass flux. In each of the nine subroutines, all seven regular shapes of matrix blocks (slab, sphere, cylinder, square, rectangle, cube, and rectangular parallelepiped) are considered. The details of this FORTRAN file is included as a PDF attachment to this report (see Appendix B.2). The direct applications of these subroutines are documented in Zhou et al. (2017a) and Zhou et al. (2017b).

For example, the subroutine CFLUX3_ZHOU_SOLUTION(MD, IBLOCK, N, TD, RLXYZ, IS_PRODUCT) is for the newly developed cumulative flux equations, with input IBLOCK for the shape index of matrix blocks, input N for the number of the truncated exponential terms in equation (1b), input TD for the dimensionless time, input RLXYZ for the aspect ratios in X, Y, and Z directions, and input IS_PRODUCT for whether a product-form or non-product-form is used for solution. The subroutine output is MD for the dimensionless cumulative flux or dimensionless average matrix-block mass fraction.

This subroutine file is part of SHPALib, which also includes a subroutine file for analytical models for mass transport (as well as heat transport and pressure propagation). Key to the analytical models is the generalized memory function, which is the Laplace transform of the transient diffusive flux equation developed for this project. The details of the memory function and analytical models for heat transport are documented in Zhou et al. (2019c).

2.3.3 Development of vertically-integrated dual-continuum model

Within the dual-continuum modeling framework, we develop models that use the vertical-equilibrium (VE) assumption in the fracture continuum and traditional multi-dimensional formulations in the matrix continuum. VE models are one type of simplified models that have been used to model fluid migration in unfractured geological formations. They assume rapid and complete buoyant segregation of the two fluid phases, resulting in vertical pressure equilibrium and allowing relatively easy integration of the governing equations in the vertical dimension. This reduction in dimensionality makes VE models computationally much more efficient than a fully three-dimensional (3D) model, but the associated assumptions restrict the applicability of VE models to subsurface systems in which the time scales of the buoyant segregation are small relative to the time scales of the horizontal transport processes (Court et al., 2012). Because of the large density difference between CO_2 and brine (on the order of 500 kg/m^3) and large permeability associated with fractured systems, we are motivated to apply the VE concept to the fracture continuum.

The transfer of fluid mass between rock matrix and fractures is a key process in dual-continuum models. It is represented by a mass transfer function, which typically depends on variables from both the fracture and matrix continua, and accounts for physical mechanisms such as viscous forces, capillary pressure, and gravity drainage. The transfer function for the VE-dual porosity model is modified from the original three-dimensional transfer function through vertical integration. The governing equations for the CO_2-brine system in the fracture and matrix continua are solved with an IMPES-type (Implicit Pressure Explicit Saturation) time stepping algorithm applied to a cell-centered finite volume spatial discretization.

2.3.3.1 VE-dual porosity sugar cube model

In this section a new dual-porosity modeling approach is described where the fracture continuum is modeled using a vertically-integrated approach and the rock matrix continuum is conceptualized as sugar cubes (Tao et al., 2018). The vertically-integrated model of the fracture continuum assumes vertical equilibrium (VE) of CO_2 and brine, which means that the two fluids have completely segregated in the vertical direction, so that there is no more vertical flow and the two fluid phases are thus at pressure equilibrium. The VE assumption is likely valid in the fracture continuum of CO_2 – brine systems, due to expected high permeability of the fracture continuum and the strong density difference between CO_2 and brine at injection formation conditions; supercritical CO_2 is approximately 500 kg/m^3 less dense than the resident brine.

In vertically-integrated models, vertical profiles of fluid saturation need to be reconstructed to compute the integrated fluid mobility – an important parameter in the vertically-integrated governing equations. In the newly developed modelling approach coupling a vertically-integrated fracture continuum to a sugar cube conceptualization of the rock matrix continuum – termed VE-sugar-cube – the reconstructed saturation and capillary pressures are also used to calculate the mass transfer fluxes. The mass transfer function from Ramirez et al. (2009) is adopted here. It considers both capillary forces, represented by the difference of the capillary pressure in the two continua, and gravitational force, represented by the difference in local fluid saturation in the two continua. The vertically-integrated mass transfer term (Qc) in the VE-sugar-cube model is computed by vertically integrating the local mass transfer terms (qc), which are based on the reconstructed saturation and capillary pressure values, from the bottom to the top of the geological formation. This integration is implemented by summing up the qc values in each vertical column of sugar cubes.

The governing equations for the CO_2-brine system in the fracture and matrix contiuna are solved with an IMPES-type (Implicit Pressure Explicit Saturation) time stepping algorithm applied to a cell-centered finite volume spatial discretization. In each time step, the vertically-integrated governing equations are solved for pressures at a reference elevation and the vertically averaged saturations in the fracture continuum, based on integrated mobilities and mass transfer fluxes from the previous time step. Those variables are then used to reconstruct local fluid pressures and saturations in the fracture continuum algebraically, based on the vertical equilibrium assumption. The reconstructed saturation values are used to update the integrated mobilities and mass transfer fluxes.

The accuracy and computational efficiency of the VE-sugar-cube model are assessed by comparison to a conventional three-dimensional dual-porosity sugar cube model – termed 3D-subar-cube. The model domain of the test case is a horizontal slice (x, z) through a storage formation (Figure 13), with a length of 1500 m and a height of 50 m. A two-dimensional slice was chosen instead of a three-dimensional domain to reduce the computational effort for the 3D-sugar-cube model. The model domain is discretized into 300 cells in the x-direction (constant Δx of 50 m) and 100 cells in the z-direction (constant Δz of 0.5 m) for both modeling approaches, but the VE-3D model for the fracture continuum has no discretization in the z-direction, as it vertically integrated. The top (z = 50 m) and bottom (z = 0 m) boundaries are no-flow boundaries. The left (x = 0 m) boundary represents the CO_2 injection with a constant volumetric source in the first cell of the VE-sugar-cube model and distributed over the first column of cells in the 3D-sugar-cube model; the left boundary is set to no-flow conditions due to symmetry. The right (x = 1500 m) boundary is set to a constant brine pressure (hydrostatic distribution) and constant zero CO_2 saturation. Initially both rock matrix and fracture continua contain no CO_2 and brine pressure in the fracture continuum is set to a hydrostatic profile. A Brooks-Corey expression is used to calculate the relative permeability in the rock matrix and fracture continua for both approaches. The injection rate is 1.8×10^{-3} kg CO_2 per second. Density of CO_2 and brine is 710 kg/m^3 and 1000 kg/m^3, respectively. Viscosity of CO_2 and brine is 4.25×10^{-5} Pa s and 3×10^{-4} Pa s, respectively. For simplicity, capillary pressure and compressibility are neglected in this test case. The porosities of the fracture and rock matrix continua are 0.03 and 0.15, respectively. The intrinsic permeability of the rock matrix is set to 10 mD (1 mD $\approx 10^{-15}$ m^2), while the intrinsic permeability of the fracture continuum is varied from 100 to 1,000 mD, with 100 mD as the base case. The two modeling approaches were compared based on CO_2 saturation plots and ratio of predicted CO_2 mass in the rock matrix continuum as compared to the fracture continuum.

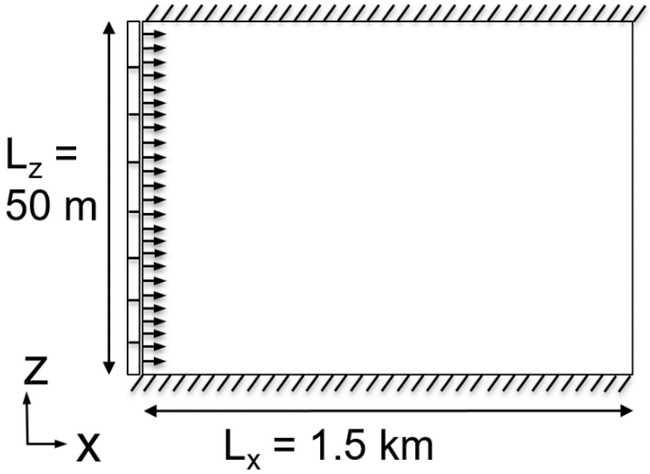

Figure 13: Schematic of the injection formation slice used as modeling domain for the comparison test cases. Taken from Tao (2017).

In a first set of comparisons models were run with fracture continuum permeabilities of 100, 500 and 1,000 mD using both VE-sugar-cube and 3D-sugar-cube models. The CO_2 saturation graphs produced by 3D-dual porosity and VE-dual porosity models are generally comparable, and the saturations become more and more similar as fracture permeability increases. When fracture permeability is 1000 mD, saturation distribution predicted by the two models are almost identical (Figure 14). Both models predict the thickness of the CO_2 plumes at the injection wells to be around 6m and the leading edges of the CO_2 plumes to be around 950 m. The VE-sugar-cube model shows a slightly longer leading edge and thinner plume than the 3D-sugar-cube model due to the sharp interface assumption. The 3D-sugar-cube and VE-sugar-cube models predict that 80.6% and 80.0% of CO_2 mass is stored in the rock matrix, respectively, while the rest remains in the fractures.

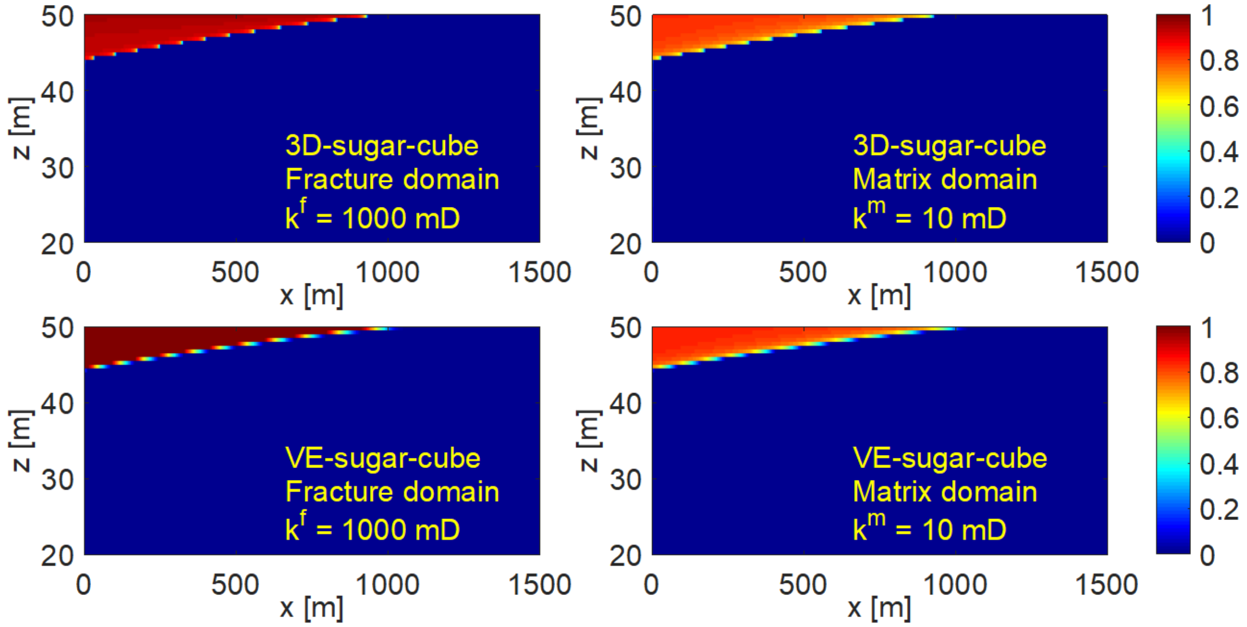

Figure 14: Comparison of CO_2 saturation distribution from the 3D-sugar-cube model (top) and VE-sugar-cube model (bottom) after 5 years of continuous CO_2 injection with fracture permeability of 1000 mD and matrix permeability of 10 mD. The color scale represents the magnitude of CO_2 saturation. Modified from (Tao et al., 2018).

The computational advantage of VE-sugar-cube model increases as the fracture permeability increases. When fracture permeability is high, the 3D-sugar-cube model requires small time steps to capture the vertical migration of CO_2, leading to long run times. However, the time steps of the VE-sugar-cube model are less dependent on the fracture permeability. In addition to allowing larger time steps, the VE-sugar-cube model runs faster in each step than the 3D-sugar-cube model due to the reduction in dimensionality. The combination of these two advantages results in significantly shorter run time for the VE-sugar-cube model. For the three test cases, the VE-sugar-cube model produces a time savings of roughly a factor of 20 as compared to the 3D-sugar-cube model. Faster models allow more simulations, which enables optimization and Monte-Carlo based risk assessments.

The two modeling approaches were also tested using non-zero capillary pressure in the matrix continuum and the simulation results from VE-sugar-cube and 3D-sugar-cube models match well (Figure 15). For a wide range of capillary entry pressure values, the difference between the predicted CO_2 mass fraction in the matrix continuum from the two models remains less than 1%.

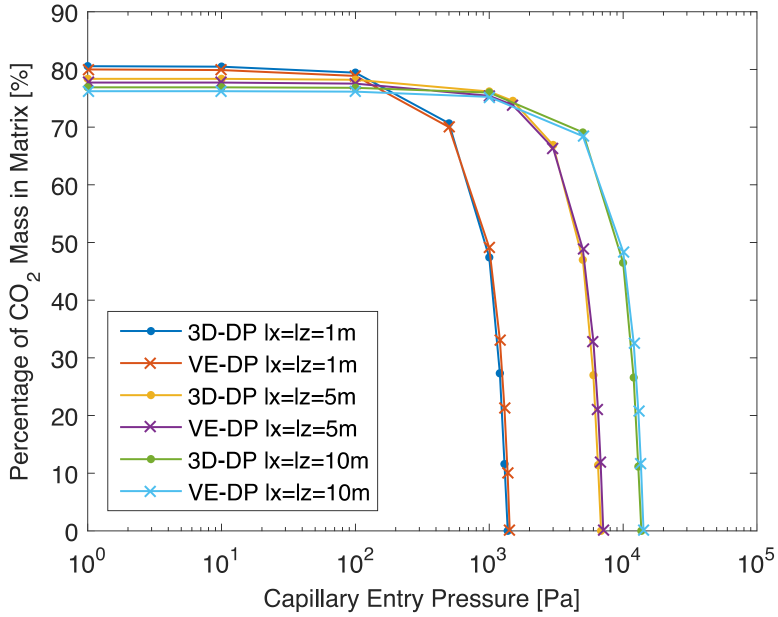

Figure 15: Predicted CO$_2$ mass fractions in the matrix continuum from VE-sugar-cube (VE-DP) and 3D-sugar-cube (3D-DP) models as a function of capillary entry pressure. Results shown are after 5 years of continuous CO$_2$ injection with fracture and matrix permeability being 1000 mD and 10 mD, respectively. Taken from Tao et al. (2018).

Overall, the simulation results show that the VE-sugar-cube model can be effective and efficient for modeling CO$_2$ migration in fractured saline aquifers when the properties of the formation allow for the VE assumption in the fracture continuum. The vertically-integrated dual-continuum modeling framework should be generally applicable to a wide range of fracture-matrix systems, providing an efficient computation approach to model multiphase flow in fractured rocks.

2.3.3.2 VE-dual porosity matchstick model

As discussed above, the matchstick conceptualization is a different dual-porosity approach, where fluid can migrate vertically along the matchsticks. The VE-matchstick model has a similar set of governing equations in the matrix continuum as the VE-sugar-cube model, except that one term (spatial derivative of the phase flux in the vertical direction, $\frac{\partial u^m_{\alpha,z}}{\partial z}$) is added to each phase's mass balance equation. In the implementation, we assume that the top and bottom of the geological formation is impermeable, so that the total vertical fluxes of CO$_2$ and brine in the matchstick sum to zero. As a result, the VE pressure equation for the fracture continuum is exactly the same as the one in the VE-sugar-cube model. For the VE transport equation, CO$_2$ flux in the vertical direction, $u^m_{c,z}$, is computed using the fraction flow formulation without explicit presence of CO$_2$ or brine pressure.

In this implementation of the VE-matchstick model, the mass transfer term in the governing equation is represented by the same mass transfer function as the one used in the VE-sugar-cube model. However, because the matchstick conceptualization allows vertical stacks of sugar cubes to be in hydraulic contact with their vertical neighbors, the sugar cube mass transfer function, which was derived based on sugar cube geometry, might not be suitable under all conditions.

Therefore, a set of numerical experiments is used to investigate conditions under which the sugar cube mass transfer function is applicable for the matchstick model.

The focus is on a single tall matrix block that is surrounded by fractures along all faces and two numerical models are constructed: one models the matrix block as a vertical stack of sugar cubes while the other models the matrix block as a single vertical matchstick. The height of the domain is fixed at 50 m and the width of the domain changes in each test case. For the "single matchstick" model, the domain is evenly divided into 10 grid cells in the x-direction and is evenly divided into 3000 grid cells in the z-direction. For the "sugar cube column" model, there are 50 sugar cubes stacked vertically in a sugar cube column (height of each sugar cube is 1 m). Each sugar cube is evenly divided into 10 grid cells in the x-direction and 50 grid cells in the z-direction. Overall, the domain of the "sugar cube column" model is divided into 10 grid cells in the x-direction and 2500 (=50×50) grid cells in the z-direction. The permeability and porosity of the matrix continuum are 10 mD and 0.15, respectively. Compressibility and fine-scale capillary pressure are neglected in all test cases for simplicity. The initial conditions for both "single matchstick" model and "sugar cube column" model are full brine saturation in the domain. The boundary conditions are CO_2 moving downward from the top of the domain along the left and right boundaries of the domain with constant velocity – this is meant to approximate CO_2 filling of the domain. Brine pressure is fixed at the bottom of the domain and hydrostatic vertical pressure profiles are assumed at the lateral sides of the domain. Numerical experiments were conducted using the two models, varying parameters such as matrix permeability, CO_2 downward velocity along the lateral boundaries, and the aspect ratio (width divided by height) of the matrix block one at a time, and simulation results from the two models were compared based on average CO_2 saturation in the domain.

The results show that the sugar cube conceptualization always estimates more CO_2 in the matrix block than the matchstick conceptualization (Figure 16). This is because CO_2 can enter the sugar cube from the top, bottom, and lateral boundaries once the sugar cube is fully surrounded by CO_2. However, for the matchstick conceptualization, CO_2 can only enter the matrix block through the lateral sides because the matchstick has no slices cutting through horizontally. Also, simulation results from the sugar cube model and the matchstick model become progressively more different as the aspect ratio of the matrix block increases. For a narrow sugar cube column, most CO_2 enters a sugar cube from the lateral sides, making the sugar cube column similar to a matchstick. When the sugar cube column becomes wider, a growing percentage of the total CO_2 influx comes from the top and bottom boundaries of the sugar cubes, so the simulation results are less similar.

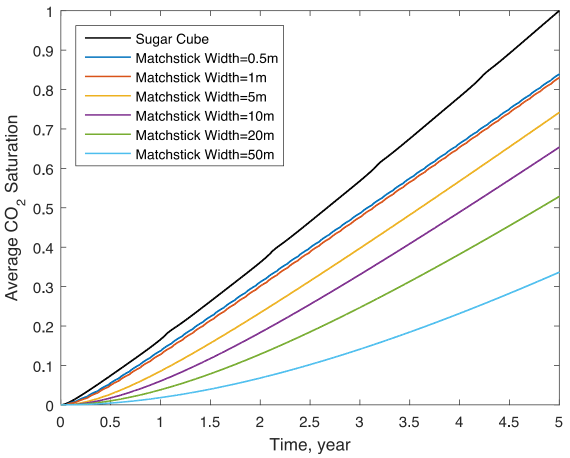

Figure 16: Average CO_2 saturations in the domain predicted by the "sugar cube column" model and the "single matchstick" model. In all plots, curves are scaled by the end value of the black curve. CO_2 moves downward along the left and right boundaries of the domain at constant velocity of 3×10^{-8} m/s.

The study also found that the sugar cube and matchstick conceptualizations produce similar results when the matrix permeability is high. When matrix permeability is fixed, the sugar cube and matchstick conceptualizations produce similar results when CO_2 downward velocity is small at the lateral boundaries of the domain. This means CO_2 plume thickness grows slowly in the fractures and could happen when CO_2 injection rate is low or when fractures have large horizontal permeability. High permeability of the matrix block and small downward CO_2 velocity in the fractures both imply that the timescale of CO_2 saturation change in the matrix block is closer (but still smaller) to the timescale of CO_2 saturation change at the lateral boundaries of the matrix block. In this case, the surfaces that cut a matchstick through horizontally (the top and bottom surfaces of a sugar cube), play a less important role in allowing CO_2 entering the matrix block. As a result, the sugar cube column behaves more like a single matchstick.

In summary, we studied a single tall matrix block and observed that modeling the matrix block as a sugar cube column and a matchstick could lead to similar modeling results for cases where the matrix block has high permeability, the CO_2 downward velocity in the fractures is small, and the aspect ratio of the matrix block is small. In those cases, the sugar cube mass transfer function may be used for the VE dual-porosity matchstick model.

2.3.3.3 VE-dual permeability model

The vertically integrated approach was also coupled with a dual-permeability conceptualization of the rock matrix (Guo et al., 2017; Tao, 2017). The overall approach is the same as for the VE – dual porosity models, where pressure and saturation profiles in fracture continuum need to be reconstructed based on the vertically-integrated values from the fracture continuum equations. The reconstructed values are then used to compute the mass transfer functions. Unlike the dual-porosity conceptualizations, the dual-permeability conceptualization allows for three-dimensional flow in the rock matrix continuum as well as in the fracture continuum. Therefore, the three-dimensional governing equations for multi-phase flow need to be solved for the rock matrix continuum. Also, the mass transfer function is expanded to include the phase pressure difference between the rock matrix and fracture continua. The algorithm proceeds as follows: the discretized pressure equations are solved numerically for the fracture continuum (two-dimensional grid) and the rock matrix continuum (three-dimensional grid) separately using phase relative permeability values and mass transfer fluxes based on the previous time step; the pressure equation are solved for both continua, incorporating the updated pressure values; the pressure and saturation profiles in the fracture continuum are reconstructed; relative permeability values are updated in both continua; and the mass transfer fluxes are updated based on updated pressures and saturations. For a detailed description of the governing equations and solution algorithm, the reader is referred to Tao (2017).

The newly developed vertically-integrated dual-permeability model, termed VE-3D model, was compared to a conventional dual-permeability model, where both the rock matrix continuum and the fracture continuum are represented by three-dimensional models, termed Full-3D model. The model domain of the test case is a horizontal slice (x, z) through a storage formation (Figure 13), with the same geometry and parameters as for the VE-sugar-cube model in section 2.3.3.1. A linear relative permeability expression is used for the fracture continua for both approaches, due to the very narrow capillary transition zone expected in the fractures. The intrinsic permeability of the rock matrix is set to 10 mD (1 mD $\approx 10^{-15}$ m^2), while the intrinsic permeability of the fracture continuum is varied from 10 to 100,000 mD, with 100 mD as the base case. The two modeling approaches were compared based on CO_2 saturation plots and ratio of predicted CO_2 mass in the rock matrix continuum as compared to the fracture continuum.

In a first set of simulations, the two modeling approaches were compared for the base case with 100 mD fracture permeability after one and five years of constant injection. A comparison of saturation plots after one (Figure 17) and five years (Figure 18) of injection show very close agreement between the two modeling approaches. These saturation plots also indicate that CO_2 migration from the fractures into the rock matrix is relatively slow process, as the CO_2 saturation in the rock matrix is lower after one year than after 5 years, even in locations where the CO_2 saturation in the fracture stays constant (e.g., close to the injection well and close to the top of the domain). The agreement between the two approaches is confirmed by the ratios of CO_2 residing in the rock matrix as compared to the fractures. After one year the Full-3D model predicts that 25.62% of the injected CO_2 remains in the fractures, while the VE-3D model predicts 25.54%. The difference is about the same after 5 years of injection, with 21.83% and 21.74% of the injected CO_2 residing in the fractures for the Full-3D and VE-3D models, respectively. Comparisons of pressure transects at different depths in the model domain also show good agreement.

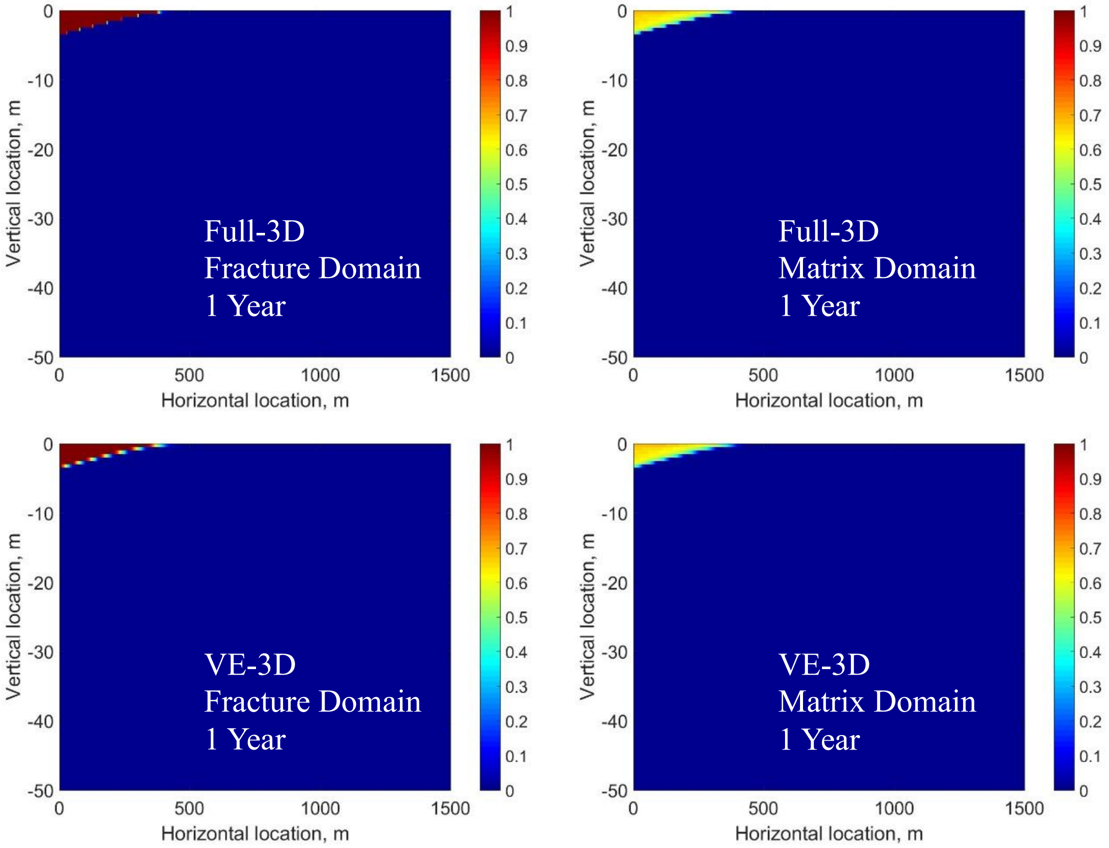

Figure 17: CO_2 saturation plots after one year of injection for the fracture and rock matrix continua based on the Full-3D and VE-3D models. Taken from Tao (2017).

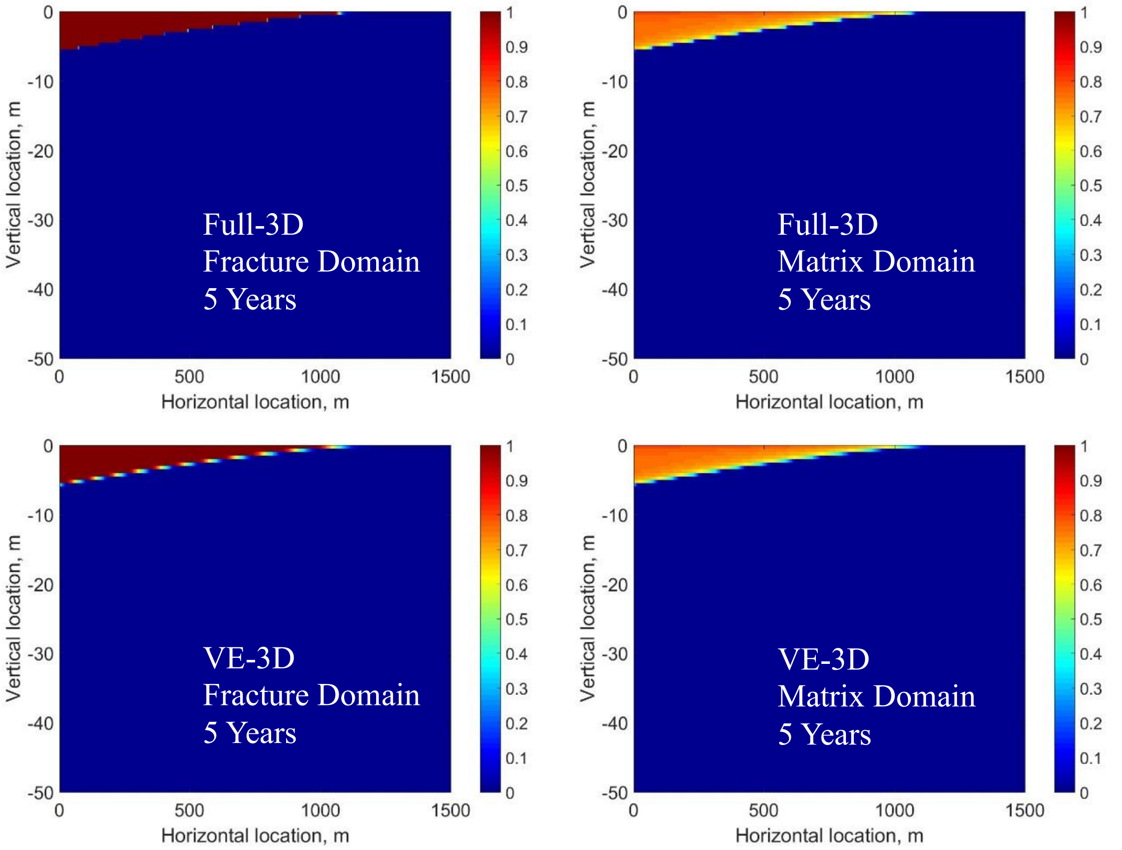

Figure 18: CO_2 saturation plots after five years of injection for the fracture and rock matrix continua based on the Full-3D and VE-3D models. Taken from Tao (2017).

A second set of results investigated the impact of the intrinsic permeability of the fracture continuum on the applicability of the VE-3D model. The fracture permeability is important, because the validity of the vertical equilibrium depends on the time scale of vertical segregation, and lower permeabilities lead to longer segregation time scales. The test case was run for a set of fracture permeabilities ranging from 10 to 100,000 mD. As shown in Figure 19 for the case of fracture continuum permeability of 10 mD the CO_2 saturation in the fracture continuum are very different for the Full-3D and VE-3D models, because CO_2 and brine have not yet fully segregated, as indicated by the wide distribution and thicker plume in the Full-3D model. Correspondingly, the CO_2 saturations in the rock matrix continua are also quite different. Results from model runs with permeabilities of 100 mD and higher (not shown) show very close agreement between the two modeling approaches, both from saturation plots and ratios of CO_2 residing in the rock matrix as compared to the fractures. This is consistent with an earlier study by Court et al. (2012) that also found a 100 mD validity threshold for single-continuum vertically-integrated models.

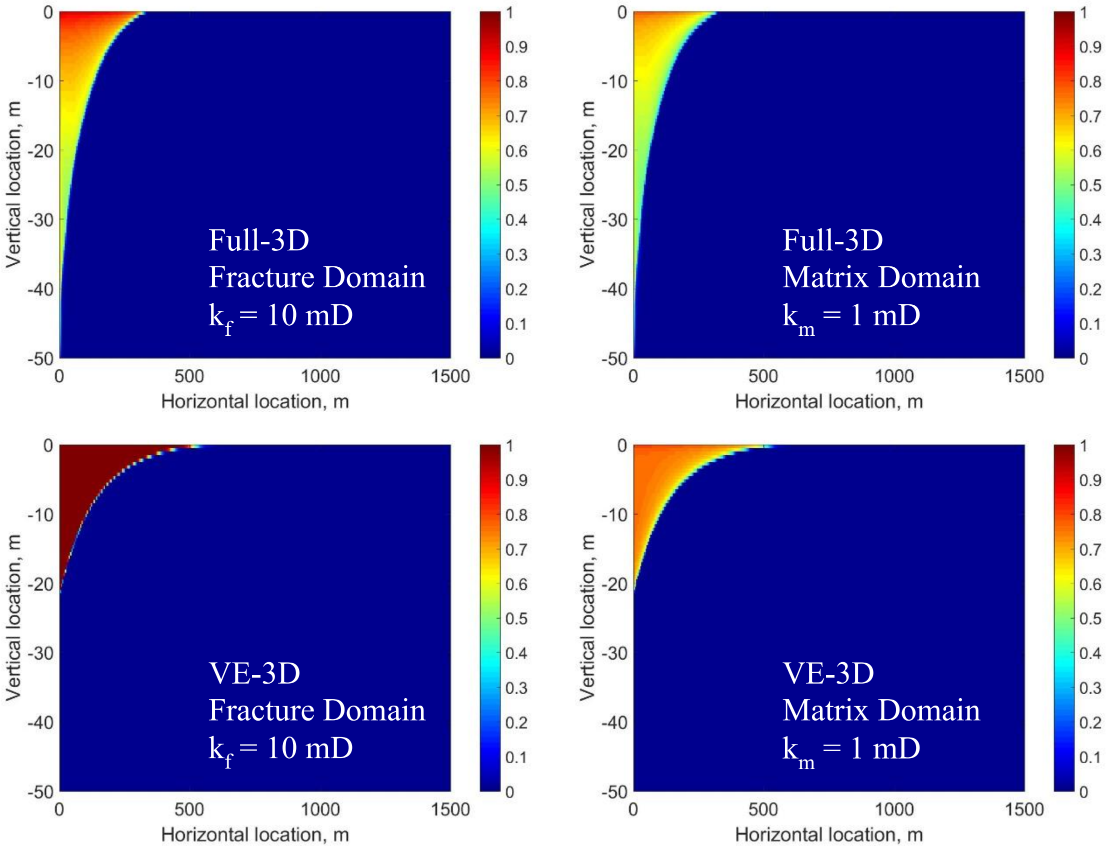

Figure 19: CO_2 saturation plots after five years of injection for the fracture and rock matrix continua based on the Full-3D and VE-3D models for the case of 10 mD fracture continuum permeability. Taken from Tao (2017).

The relative importance of the driving forces – gravitational and viscous – for mass transfer between rock matrix and fractures was also investigated. Three model cases are compared using the VE-3D model: mass transfer function with both viscous and gravitational forces, mass transfer only due to viscous forces, and mass transfer only due to gravitational forces. CO_2 saturation plots for the three cases are shown in Figure 20 and show a complex interplay between viscous and gravitational mass transfer drives. When only one driving force is acting, both viscous and gravitational forces lead to CO_2 migrating from the fracture continuum to the rock matrix continuum. However, the gravitational drive is much stronger than the viscous drive, leading to 98% of the injected CO_2 migrating into the rock matrix, while only 71% migrates for the case of only viscous drive and 78% for the case with a combination of gravitational and viscous drives. These results suggest that the two mass transfer drives counteract each other, with viscous forces moving some CO_2 from the rock matrix continuum back to fracture continuum.

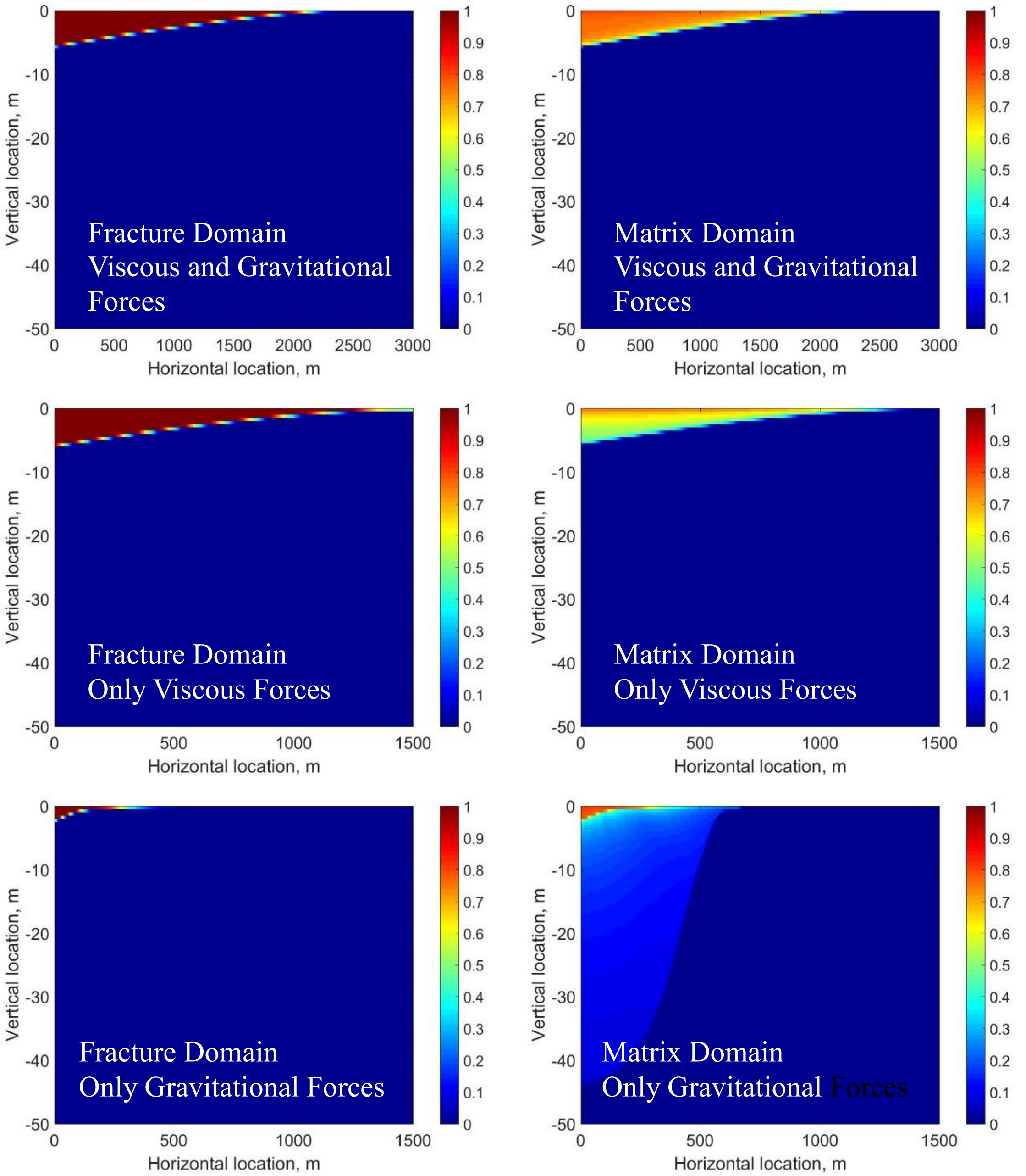

Figure 20: CO_2 saturation plots after five years of injection for the fracture and rock matrix continua based on the VE-3D model highlighting the impact of the two mass transfer driving forces. Taken from Tao (2017).

The results in this section show, that a vertically-integrated model for the fracture continuum can be coupled with a three-dimensional model for the rock matrix continuum to construct an accurate dual-permeability modeling approach. The applicability of the VE-3D modeling depends on the validity of the vertical equilibrium assumption in the fracture continuum, which appears to be valid for fracture permeabilities of 100 mD and higher in the context of GCS modeling. One advantage of the VE-3D model is that the computational effort for solving the governing equations is reduced, because the VE-3D model uses a two-dimensional grid for the fracture continuum, instead of a three-dimensional grid. Additional details about the VE-3D model can be found in Tao (2017) and Guo et al. (2017).

2.4 Application of site-scale models and sensitivity analysis

Several sensitivity analyses were conducted using the newly implemented reservoir simulators to investigate how reservoir properties and operational conditions impact storage capacity in fractured reservoirs. The first investigation involves so-called capillary bridges, where a vertical stack of rock matrix blocks may act as a continuous column. Capillary bridges have a strong impact on storage capacity, because the storage volume excluded by capillary entry pressure of the rock matrix is much smaller in a column than in a stack of separate blocks. Another set of analyses compared storage capacities for a fractured and unfractured hypothetical anticlinal structure, as well as determined the importance of the mass exchange rate in relation to the CO_2 injection on the storage capacity. The impact of ambient pressure and temperature conditions in the storage reservoir on storage capacity was also studied. An additional study investigated the potential for CO_2 storage through migration of dissolved CO_2 into the rock matrix. This study investigated how the shape and size of a single rock matrix impacts the mass of dissolved CO_2 that can be stored in that block, along with how the mass of stored CO_2 changes over time. The same study also looked at the storage capacity of a fractured storage formation for three cases of rock matrix blocks: cubes of uniform size, mixture of cubes with four different sizes, parallelepipeds of uniform size.

2.4.1 Capillary bridges

A first set of analyses is used to estimate the effective storage efficiency, E_e, under gravity-capillarity equilibrium conditions for (1) an isolated matrix block with different fracture spacing in the vertical direction and (2) a vertical column of connected matrix blocks with different reservoir thickness. The equilibrium effective storage efficiency is defined as $E_e = E/(1 - S_{lr})$, where E is the equilibrium storage efficiency of the rock matrix or the average sCO_2 saturation (i.e., the volumetric fraction of the matrix pore volume that is occupied by sCO_2), and S_{lr} is the residual water saturation. E_e is not dependent on residual water saturation and is relevant to the matrix pore volume potential for CO_2 storage. It is assumed that the matrix block and column are surrounded by fractures completely filled with sCO_2, with a constant density difference of 400 kg/m^3 between brine and CO_2. To investigate the impact of capillary entry pressure and reservoir thickness, the capillary entry pressure, P_{ce}^{m}, of the matrix blocks varies from 0.1 to 2.0 bar with an increment of 0.01 bar, and the reservoir thickness (B) varies from 1 to 64 m with an increment of 1 m. Numerical integration of effective CO_2 saturation with vertical discretization of 0.02 m was used along with the van Genuchten function and model parameter $m = 0.457$ (van Genuchten, 1980).

Figure 21 shows the equilibrium effective storage efficiency of sCO_2, as a function of reservoir height (or block height for unconnected matrix blocks) and matrix entry capillary pressure. For moderate matrix permeability and low capillary entry pressure, the equilibrium effective storage efficiency is as high as 60% for a 40 m thick reservoir, indicating that the rock matrix can be very effective for $scCO_2$ storage in fractured reservoirs. In the case without matrix-matrix connectivity, the height of matrix blocks is the key factor for such calculations, and the storage efficiency is significantly smaller than that for the entire thickness of the reservoir that is assumed to have matrix-matrix connectivity, because the capillary entry pressure needs to be overcome in each block. The equilibrium effective storage efficiency shown in Figure 21 indicates the importance of matrix-matrix connectivity and matrix capillary continuity.

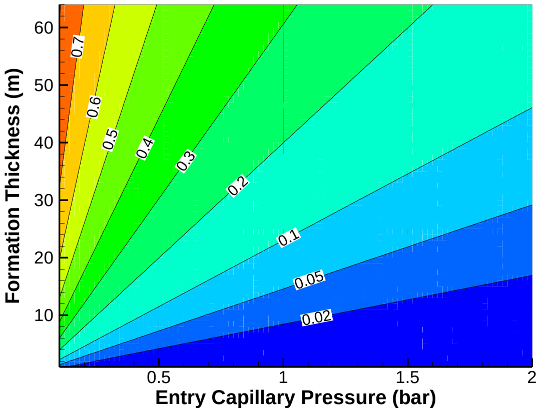

Figure 21: Equilibrium effective storage efficiency of $scCO_2$, as functions of reservoir height in the case with connected matrix blocks (or height of unconnected matrix blocks) and matrix entry capillary pressure.

A discrete fracture-matrix (DFM) approach was used with TOUGH2 as the simulator to investigate the dynamic storage efficiency as comparison with the equilibrium storage efficiency. Two model domains were investigated: a single vertical column and a 100 m long reservoir section consisting of multiple columns. For the single column study, the vertical column consists of 10 homogeneous matrix blocks, each of which is 3.9 m high and 2 m wide, and 11 horizontal fractures with an aperture of 1 mm, separating the blocks. The column is bounded by two vertical fractures with an apertures of 1 mm. The matrix blocks and horizontal fractures are initially saturated with brine and the vertical fractures are fully saturated with CO_2 for all time. The bottom fracture is of a fixed pressure at 200 bar. The density of CO_2 is 700 kg/m^3 at a pressure of 200 bar and a temperature of 64 °C and the brine density is 1100 kg/m^3; a density difference of 400 kg/m^3. The rock properties of the fractures and matrix blocks are listed in Table 1.

Table 1: Rock properties of the fractures and matrix blocks in the column setup

Rock properties	Fractures	Matrix
Porosity	0.9	0.25
Permeability (md)	100	1
Capillary entry pressure (bar)	0.001	0.05, 0.1, 0.5, 1.0, 5
V-G parameter m	0.457	0.457
Residual water saturation	0.05	0.30
Residual scCo2 saturation	0.05	Drainage only
Pore compressibility (Pa^{-1})	4.28×10^{-10}	4.28×10^{-10}

Three cases with 0%, 30%, and 100% matrix-matrix connectivity are used to investigate the importance of the matrix-matrix connectivity. For 0% connectivity, horizontal fractures perfectly separate matrix blocks, while for 100% connectivity, the apertures of the internal horizontal fractures is set to zero, so that the neighboring matrix blocks touch each other. For 30% connectivity, the parameters of central portion of internal horizontal fractures are set to matrix values instead of fractures values, to create connectivity between matrix blocks. Figure 22 shows the saturation distribution of $scCO_2$ in the discrete fractures and matrix blocks for the three cases of matrix-matrix connectivity and three cases of matrix entry capillary pressure (0.1, 0.5, and 1.0 bar). The results show that higher capillary entry pressures strongly reduce the amount of CO_2 that can enter blocks for the case of 0% matrix-matrix connectivity, severely limiting the storage capacity of such systems. The results also show that the cases with 30% and 100% matrix-matrix connectivity act very similar to each other. This suggests that 30% matrix-matrix connectivity is sufficient for the matrix blocks to act as a column instead of single blocks.

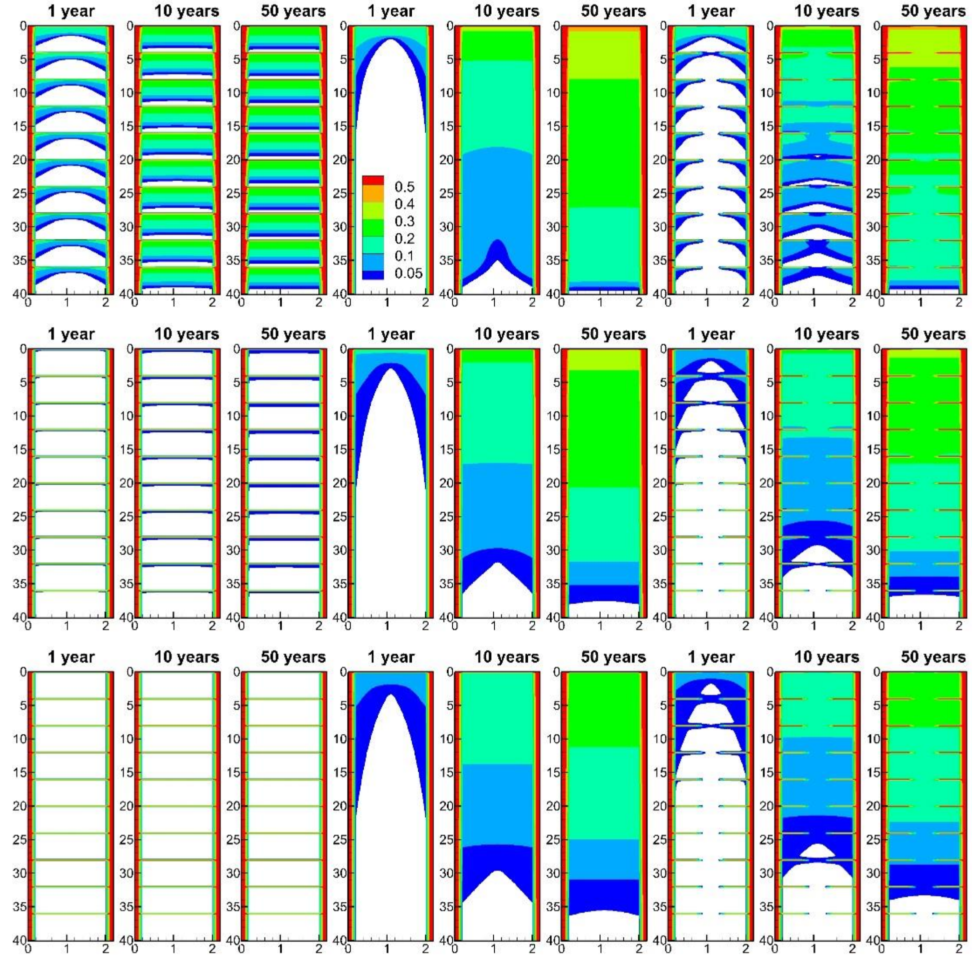

Figure 22: Distribution of CO_2 saturation in the discrete fractures and matrix blocks at 1, 10, and 50 years with 0% (first three columns), 100% (middle three columns), and 30% (last three columns) matrix-matrix connectivity for the case of 0.1 bar (top panel), 0.5 bar (middle panel), and 1.0 bar (bottom panel) of matrix capillary entry pressure.

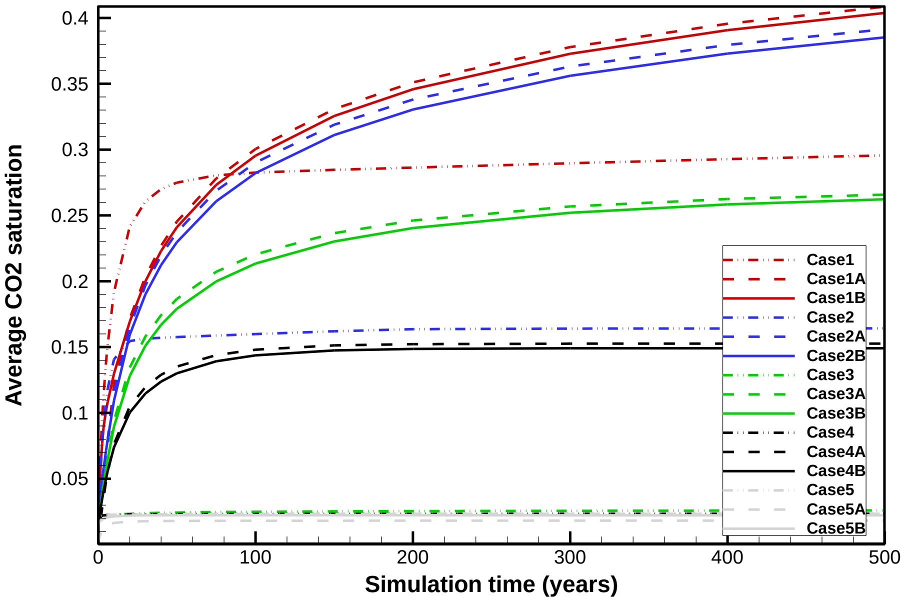

Figure 23: Average matrix CO_2 saturation, as a function of time, for 0% (denoted by no letter), 100% (denoted by A), and 30% (denoted by B) matrix-matrix connectivity in the case of 0.05 bar (Case 1) through 5.0 bar (Case 5) of matrix entry capillary pressure.

Figure 23 shows the average matrix CO_2 saturation, as a function of time for the three matrix-matrix connectivities and five matrix capillary entry pressures. For the matrix capillary entry pressure of 0.05 bar, individual matrix blocks reach equilibrium faster in the case of no matrix-matrix connectivity (dash-dot red line) than the two cases with 30% (solid red line) and 100% connectivity (dashed red line), because each matrix block works independent of other matrix blocks, so that CO_2 enters through the top and the sides. For the other two cases, CO_2 predominantly invades the matrix blocks downward and to a less extent from the sides, taking a longer time to reach equilibrium. The time scale to reach equilibrium will be shorter in the case of higher matrix permeability and smaller fracture spacing. On the other hand, the equilibrium storage efficiency – denoted by a lower average CO_2 saturation – in the absence of matrix-matrix connectivity is smaller than in the presence of matrix-matrix connectivity. For a higher matrix capillary entry pressures (0.5 (green) and 1.0 bar (black)), the storage efficiency is very small in the absence of matrix-matrix connectivity, but is still more than 10% in the presence of matrix-matrix connectivity.

The column-scale simulations show the importance of matrix-matrix connectivity, in particular for a rock matrix with low permeability and high capillary entry pressure. When $P_{ce}^{m} \geq \Delta\rho g H_m$, (with H_m the height of a matrix block) the effect of a capillary barrier in the absence of matrix-matrix connectivity will prevent any CO_2 from entering matrix blocks with a height of H_m or less, leading to negligible storage efficiency. In the presence of matrix-matrix connectivity, the effect of a capillary barrier occurs only immediately above the CO_2-brine interface in the fracture continuum, because of the capillary continuity between matrix blocks out of the capillary transition zone.

Next, the simulations are extended to cover multiple columns with transient CO_2 saturation in the fractures to investigate the impact of matrix-matrix connectivity at the plume scale. Only the case with 30% matrix-matrix connectivity is simulated. It should be pointed out that these simulations are also use a DFM approach and are therefore not based on the dual-continuum approach. To allow for full connectivity of all vertical fractures, two 1 m thick sections in the y-direction are connected; the back section has 0% matrix-matrix connections, while the front section has 30% matrix-matrix connectivity. In this way, the matrix blocks are partially connected with each other to maintain matrix capillary continuity. The vertical sections are an extension of the vertical column discussed above by adding 50 columns together. The injection rate of CO_2 is 0.001 kg/s at the top-left corner, the downstream boundary is open for scCO_2 and brine flow, and the top/bottom/upstream boundary are no-flow boundaries. Again, the sensitivity analysis of matrix capillary entry pressure with 0.05, 0.1, 0.5, 1.0, and 5 bar is conducted. Figure 24 shows the CO_2 saturation in fractures and matrix blocks at different times for two cases with matrix capillary entry pressure of 0.1 and 0.5 bar.

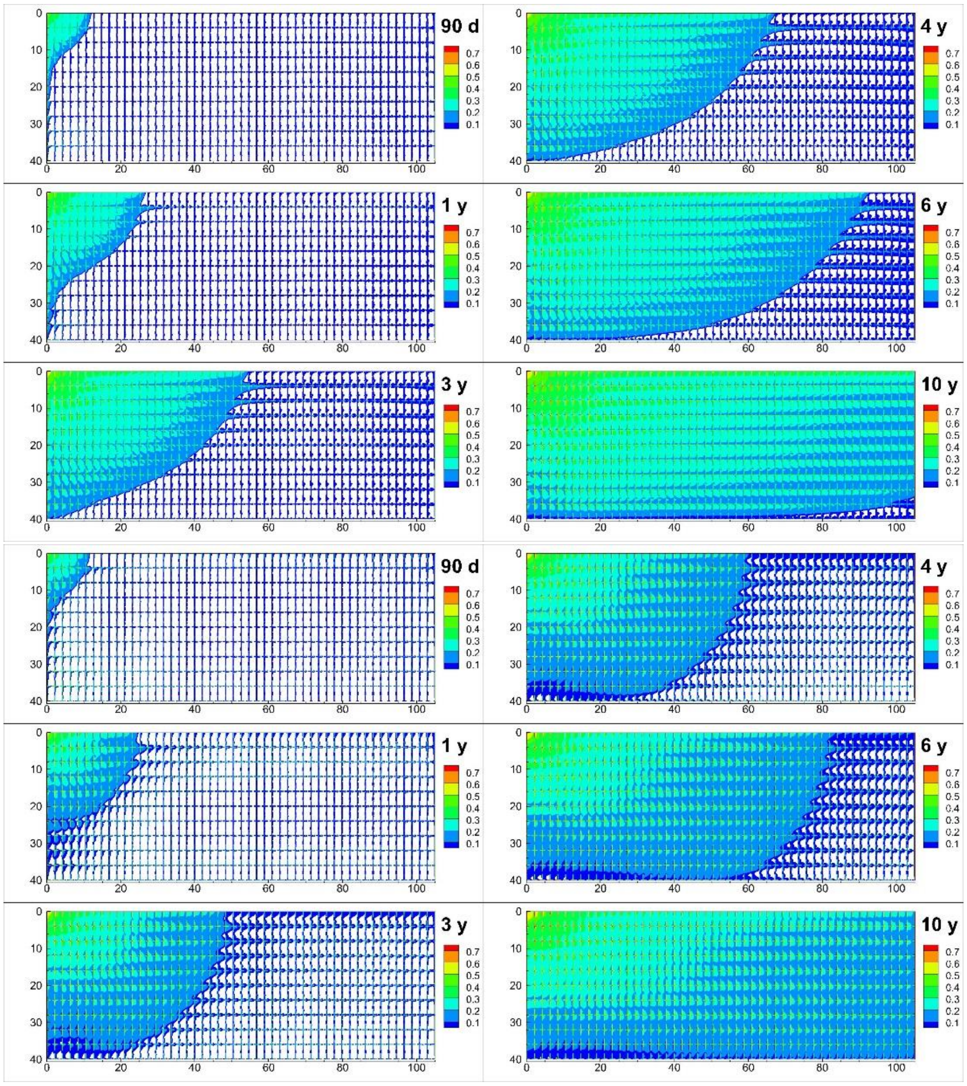

Figure 24: Saturation of CO_2 in discrete fractures and matrix blocks simulated for the 100 m long reservoir section at 90 days, 1, 3, 4, 6, and 10 years in two cases with matrix entry capillary pressure of 0.1 (top six plumes) and 0.5 bar (bottom six plumes).

The reservoir section simulation results show that (1) the storage in the reservoir section is significant and dominant in the rock matrix, and (2) the bulk storage in the rock matrix is coupled with preferential migration of CO_2 in fractures. The modeling accuracy achieved in this study can be attributed to (1) the matrix-matrix connectivity and matrix capillary continuity considered in these simulations, and (2) the high-resolution discretization of discrete fractures and matrix blocks. More details of the simulations above in this section and additional simulations will be published in Zhou et al. (2019b) and Zhou et al. (2019a).

2.4.2 Injection into fractured vs unfractured reservoirs

An additional study investigated the impact of CO_2 storage in an anticline structure in a fractured reservoir as compared to an unfractured one (March et al., 2018). The model domain is 1000 x 1000 m in the horizontal and 100 m in the vertical. The anticline has its center in the center of the domain ($x = y = 500$ m) and dips at an angle of about 2.8°. The reservoir properties of the unfractured model and the rock matrix continuum of the fractured model are set to the same values to simulate the case of encountering unexpected fractures. CO_2 is injected into the center of the anticline for 1000 days. Once CO_2 reaches the domain boundary (i.e., the spill points of the anticline), containment of the plume is considered lost. Simulations are conducted with MRST with the newly developed dual-porosity module.

Figure 25 shows results of the numerical simulations on the conceptual anticline and contrasts the behavior of the fractured and unfractured reservoirs. In the fractured reservoir CO_2 migrates to the top of the anticline along the fractures and only spreads laterally once it reaches the caprock (Figure 25c), while the CO_2 plume in the unfractured model shows the common inverted bell shape (Figure 25b). The flat plume leads to a loss plume containment after about 400 days in the fractured reservoir, while the plume is still fully contained at the end of injection in the unfractured reservoir. The overall storage volume of the anticline is reduced by about 33% compared to the case of the unfractured reservoir. However, if the anticline alone is the storage reservoir, injection would have to cease after 400 days to ensure that no CO_2 escapes the storage complex. This would mean a reduction of stored CO_2 by about 66%. Additional anticline simulations are discussed in March et al. (2018).

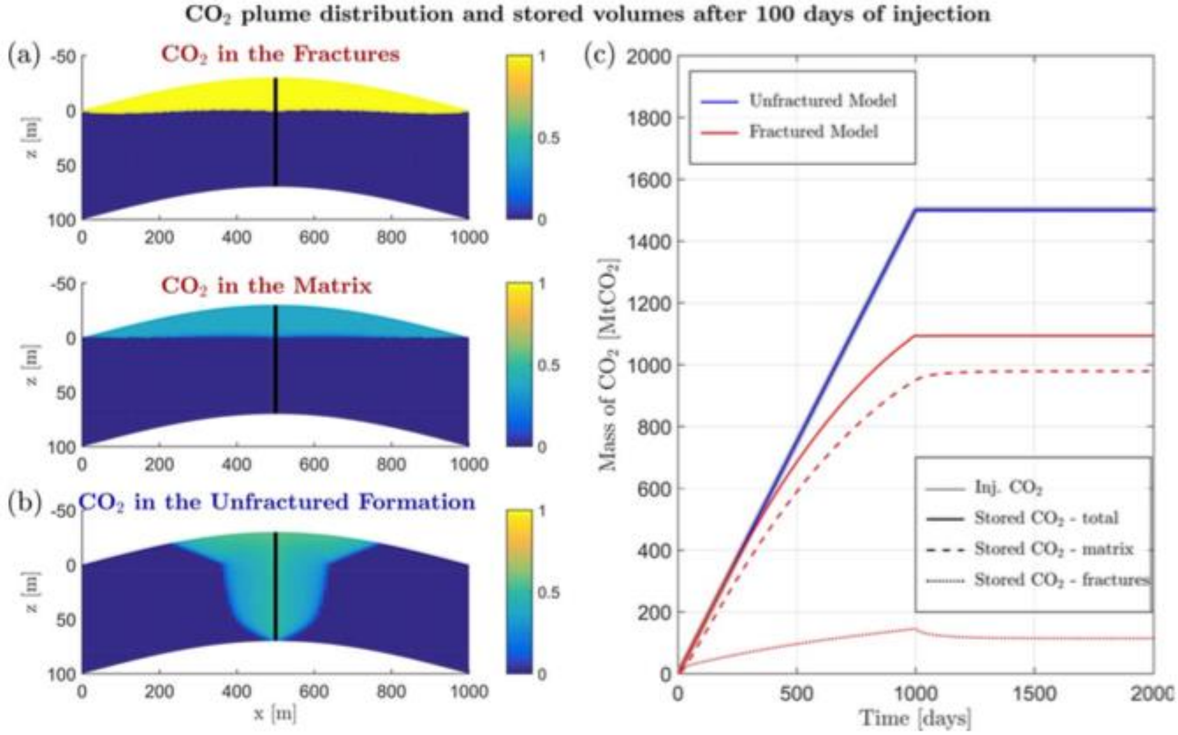

Figure 25: CO$_2$ saturation distributions for (a) the fractured anticline (top fractures, bottom matrix) and (b) the unfractured anticline. (c) Injected and stored mass of CO$_2$ for both simulation cases (lines for injected CO$_2$ mass and CO$_2$ mass stored in the unfractured reservoir coincide). Taken from March et al. (2018).

2.4.3 Impact of injection rate

The same model of an anticline in a fractured reservoir as used in section 2.4.2 was used to investigate the impact of injection rate on storage capacity. Four different injection rates were chosen, defined by the time it takes to fill the storage volume available in the anticline in an unfractured reservoir (PV^{eff}). Figure 26 shows that for the three higher injection rates, the stored mass (dashed line) diverges from the injected mass (solid line), meaning that CO$_2$ reaches the spill point before the entire storage volume has been accessed. At the higher injection rates CO$_2$ migrates along the fractures to the spill point in a short time, thus not allowing a significant mass of CO$_2$ to transfer from the fractures to the rock matrix, where the majority of the storage volume is. As the injection rate is reduced, the CO$_2$ takes longer to reach the spill point and there is more time for CO$_2$ to migrate into the rock matrix. For the lowest injection rate chosen, the entire storage volume is accessed before CO$_2$ reaches the spill point (i.e., the stored mass and injected mass remain the same during the entire injection timeframe). The lowest injection rate can be considered an optimal injection rate, as the maximum storage volume is achieved in the shortest possible time. For additional simulation results and a discussion on estimating the optimal injection rate the reader is referred to March et al. (2018).

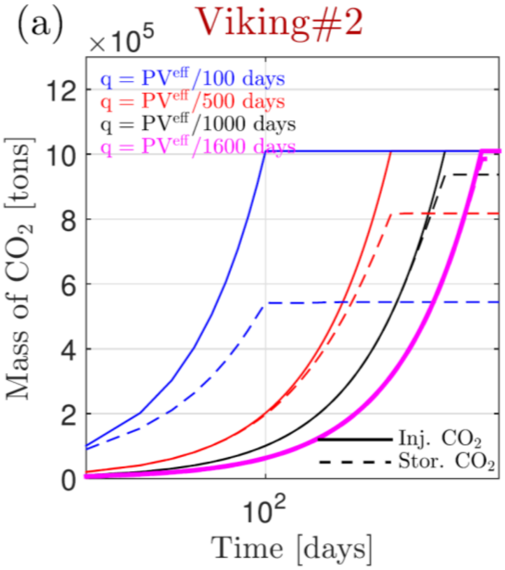

Figure 26: Mass of CO_2 injected (solid) and stored in the anticline (dashed) for four different injection rates defined by the time to fill the anticline storage volume in an unfractured reservoir (PV^{eff}). Taken from March et al. (2018).

2.4.4 Impact of storage formation conditions on storage capacity

This section presents an assessment of CO_2 storage potential in naturally fractured reservoirs (NFR) using dual-porosity models. The impact of a system of fractures on storage in a saline aquifer is investigated by analyzing the time scales of brine drainage by CO_2 in the matrix blocks and the maximum CO_2 that can be stored in the rock matrix.

Figure 27 shows the results of the numerical simulations for one matrix block with parameters from a range of different formations considered for CO_2 storage (Bennion & Bachu, 2008). The parameters are summarized in Table 2. Figure 27a shows the absolute mass stored in an example matrix block of size $L_x = L_y = L_z = 10$ m; Figure 27b shows the volume fraction filled with CO_2 against the time it takes to reach 95% of the equilibrium value (t_{95}). The circles are inversely scaled according to the capillary pressure (P_c): small circles correspond to high P_c and large circles correspond to low P_c. The circle fill colors correspond to different environments (shown in the legend of the figure), while the color of the edges correspond to different samples (shown in the figure). The drainage time t_{95} shows a large variation across the different cases, ranging from approximately 10 days to approximately 365 days. It is therefore an important metric to be observed during storage operations. In the low-P_c cases, the largest drainage times are seen in the Viking#2 and Nisku#1 samples, due to their larger effective pore volume and lower permeability. The shallow-cold environment leads to higher times compared to the deep-cold, which is more evident for the Nisku#1 sample (355 days vs 150 days). This is due to the larger viscosity ratio between CO_2 and brine in deep-cold compared to shallow-cold environments ($\mu_n / \mu_w = 0.157$ vs $\mu_n / \mu_w = 0.06$). The deep-warm environment shows the largest value of viscosity ratio, which explains why the yellow circles are concentrated on the left half of the plot ($\mu_n / \mu_w = 0.2$).

Then, the new transfer function as well as the one by Gilman (1986) are assessed against the fine scale simulations carried out for the parameter space given by Table 2 is explored. Figure 28 shows a comparison of different transfer models for a match-stick geometry, i.e. when only vertical fractures are assumed to be present. Here the block has the dimensions of $L_x = L_y$ =1 m and L_z = 20. The sugar cube analysis as well as the definition of the error is provided in March et al. (2017). Figure 28a shows the results for all assessed parameters, while Figure 28b shows the evolution of CO_2 in the matrix with time for selected cases and different mass transfer models as well as the high resolution simulation. Figure 28 shows that the proposed model provides much more accurate results compared to Gilman (1986) in all cases. While the error of the newly developed model is mostly less than 10%, the Gilman (1986) model heavily overestimates the transfer (Figure 28b), leading to mismatches of up to 325%(Figure 28a). The figure also shows results for the transfer model by Di Donato et al. (2006) which improves the behavior substantially, but underestimates the transfer in most cases.

Table 2 Physical parameters used to evaluate gravity drainage on a block scale. Modified from March et al. (2018).

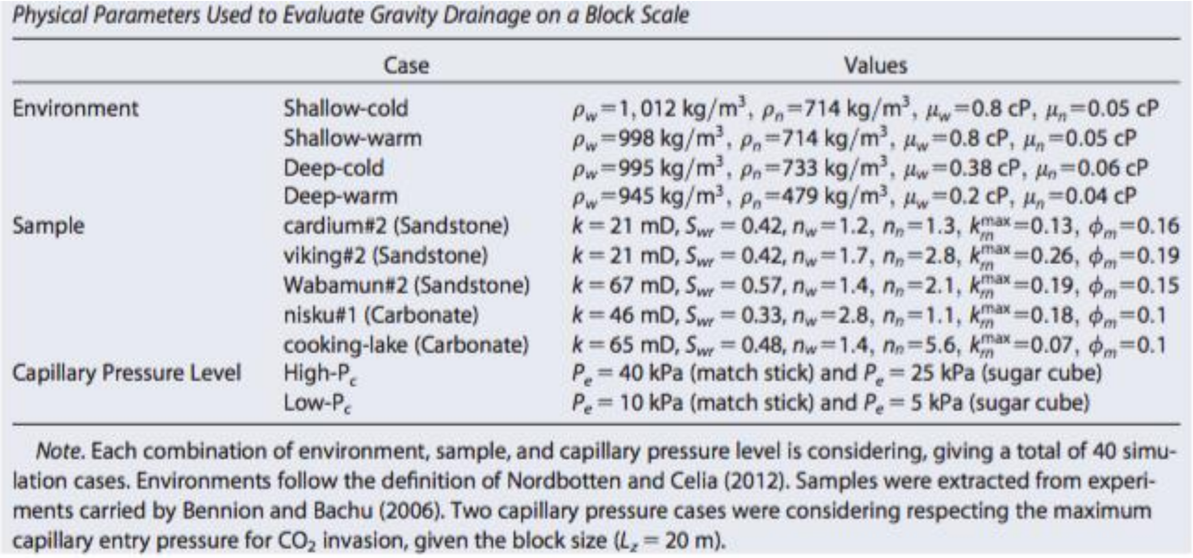

Physical Parameters Used to Evaluate Gravity Drainage on a Block Scale

	Case	Values
Environment	Shallow-cold	ρ_w=1,012 kg/m^3, ρ_n=714 kg/m^3, μ_w=0.8 cP, μ_n=0.05 cP
	Shallow-warm	ρ_w=998 kg/m^3, ρ_n=714 kg/m^3, μ_w=0.8 cP, μ_n=0.05 cP
	Deep-cold	ρ_w=995 kg/m^3, ρ_n=733 kg/m^3, μ_w=0.38 cP, μ_n=0.06 cP
	Deep-warm	ρ_w=945 kg/m^3, ρ_n=479 kg/m^3, μ_w=0.2 cP, μ_n=0.04 cP
Sample	cardium#2 (Sandstone)	$k = 21$ mD, $S_{wr} = 0.42$, n_w=1.2, n_n=1.3, k_{rn}^{max}=0.13, ϕ_m=0.16
	viking#2 (Sandstone)	$k = 21$ mD, $S_{wr} = 0.42$, n_w=1.7, n_n=2.8, k_{rn}^{max}=0.26, ϕ_m=0.19
	Wabamun#2 (Sandstone)	$k = 67$ mD, $S_{wr} = 0.57$, n_w=1.4, n_n=2.1, k_{rn}^{max}=0.19, ϕ_m=0.15
	nisku#1 (Carbonate)	$k = 46$ mD, $S_{wr} = 0.33$, n_w=2.8, n_n=1.1, k_{rn}^{max}=0.18, ϕ_m=0.1
	cooking-lake (Carbonate)	$k = 65$ mD, $S_{wr} = 0.48$, n_w=1.4, n_n=5.6, k_{rn}^{max}=0.07, ϕ_m=0.1
Capillary Pressure Level	High-P_c	P_e = 40 kPa (match stick) and P_e = 25 kPa (sugar cube)
	Low-P_c	P_e = 10 kPa (match stick) and P_e = 5 kPa (sugar cube)

Note. Each combination of environment, sample, and capillary pressure level is considering, giving a total of 40 simulation cases. Environments follow the definition of Nordbotten and Celia (2012). Samples were extracted from experiments carried by Bennion and Bachu (2006). Two capillary pressure cases were considering respecting the maximum capillary entry pressure for CO_2 invasion, given the block size (L_z = 20 m).

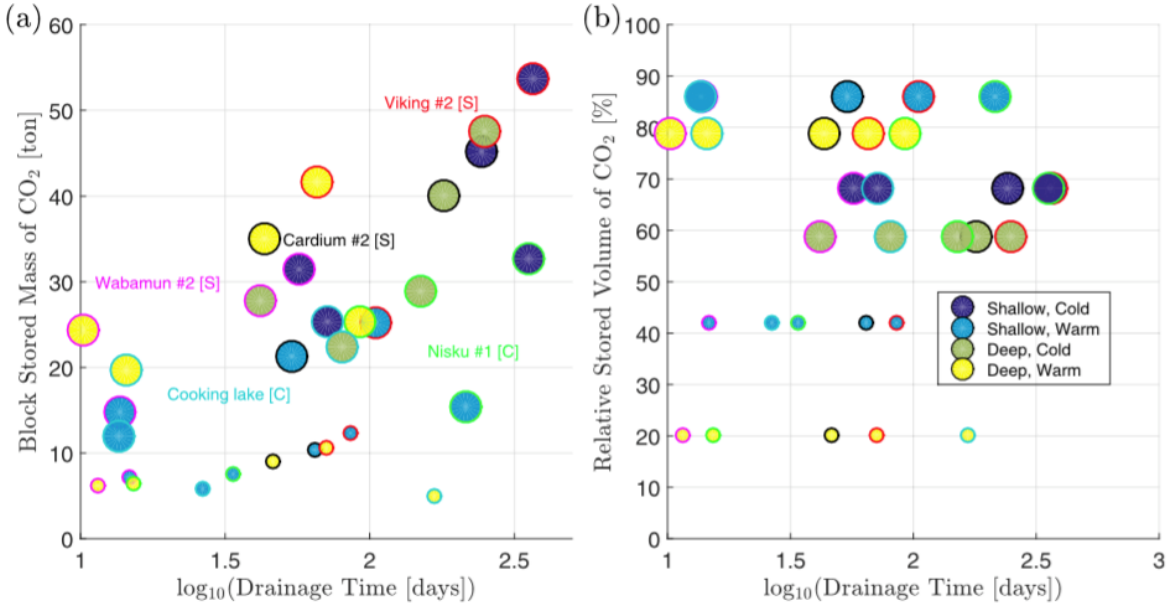

Figure 27 Analysis of the maximum CO_2 storage and drainage time scales on a single block for the sugar cube geometry. (a) Drainage time versus stored mass of CO_2; (b) Drainage time versus relative stored volume of CO_2. The relative volume provides a percentage measure of the pore volume not effectively used for storage due to the presence of a fracture system. Small circles correspond to high-P_c cases. Taken from March et al. (2018).

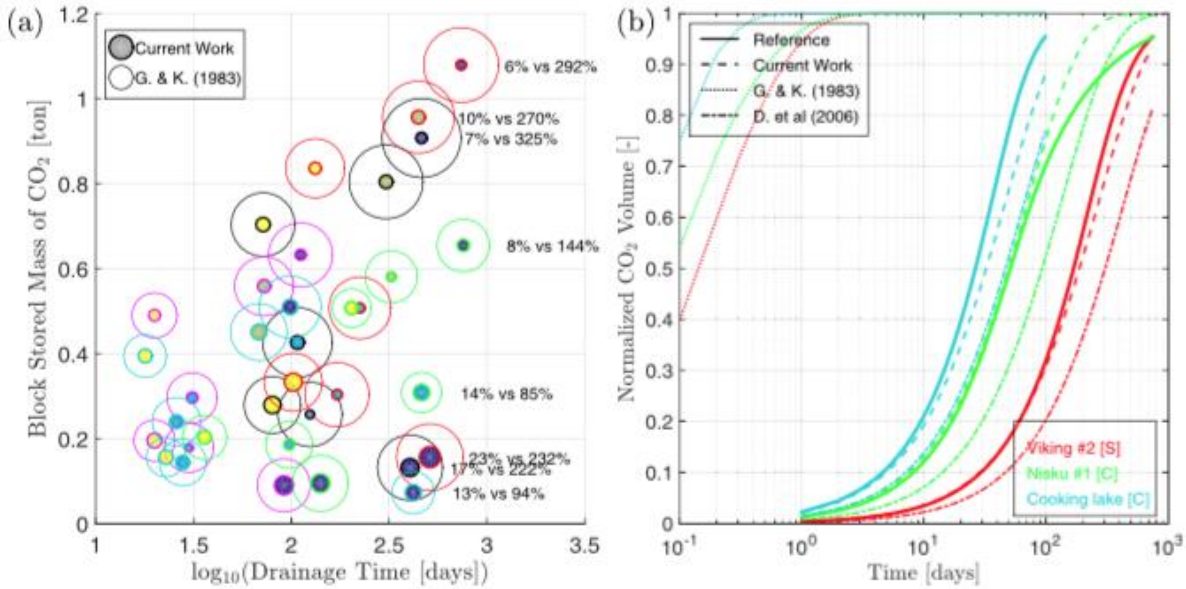

Figure 28 Evaluation of transfer functions for the matchstick matrix conceptualization. Circle edges and fills are colored following the pattern in Figure 27. (a) The size of the circle is proportional to the error when using Gilman (1986) (nonsolid circles) and the transfer function proposed in this work (solid circles) to model the drainage process, relative to a three-dimensional numerical reference model. (b) Representative drainage curves showing the reference solution, given by high-resolution simulations of a single block (solid lines), the

Gilman (1986) transfer function (dotted line), the Di Donato et al. (2006) transfer function (dash-dotted line) and the transfer function proposed in this work dashed line). Taken from March et al. (2018).

2.4.5 Impact of fractures on storage

The main objective of this section is to evaluate the impact of a fracture network in the target formation on the storage capacity. In other words, how detrimental are fractures for storage? The general prevailing understanding at the moment is that a system of interconnected fractures would make CO_2 storage infeasible due to very early breakthrough of the CO_2 plume in the highly permeable fracture network and low storage capacity, because the CO_2 does not enter the matrix at any significant rate, if at all. As is shown in this section this is not necessarily the case. In fact, fractures can even boost storage – if the plume migration is considered – due to increased injectivity. The newly developed models to evaluate CO_2 storage potential in large aquifers (March et al., 2018; March et al., 2017) are applied to understand the key geological conditions that are favorable for storage. The transfer function is incorporated in a vertically-integrated model with a simple first order dual-porosity (VIDP) model implemented using the MRST-AD framework. Details of the implementation are given in the appendix of March (2018). The model is based on four assumptions:

1. The fluid distribution in the fractures is in vertical equilibrium.
2. The Vertically-integrated plume migration domain is one-dimensional.
3. Capillary continuity across horizontal fractures.
4. Sharp interface between CO_2 and brine inside the matrix.

The model is used to investigate the sensitivity towards basin temperature, depth i.e. pressure of the formation and its petrophysical properties in storage. The results show that temperature and pressure affect storage in a more intricate way than it does for unfractured formations. In an unfractured formation a higher CO_2 density increases the storage capacity for a given rock volume. In fractured formation, however, a density difference is required to drain the matrix against the capillary forces. Since a higher CO_2 density causes a smaller density difference ($\Delta\rho$) between CO_2 and brine, less CO_2 can migrate into the rock matrix, leading to a lower storage capacity. Hence, storage capacity can also decrease with density depending on which aspect dominates. The basic petro-physical parameters for the simulations are given in Table 3. Further, for this study a depth of 1000 m is considered shallow and a depth of 3500 m deep. A warm basin has a surface temperature T_s = 20° C and a geothermal gradient of G_T = 45° C/km, while a cold basin has a surface temperature T_s = 10° C and a gradient of. G_T = 25° C/km. Figure 29 illustrates the change in storage with respect to depth for a warm and cold basin. Note that the storage drops in the cold basin due to the reduced density difference. Two additional parameters were identified to assess storage potential in NFRs: (1) the minimum thickness ($L_{CO_2}^{min}$) of the CO_2 plume in the fractures that is required for CO_2 to overcome the capillary entry barrier and drain the matrix and (2) the mass ($M_{CO_2}^{a}$) of CO_2 per horizontal aquifer area. These parameters can help ranking fractured aquifers according to storage potential. At a distance from a well the CO_2 plume tends to be relatively thin due to buoyancy. Hence, a large minimum thickness will prevent the CO_2 from entering the matrix. The mass stored per horizontal aquifer area accounts further for the shape of the capillary pressure saturation relationship and the density of CO_2 as well as the aquifer height. Both quantities are static and are quickly calculated without simulations. Figure 30 shows the behavior of those parameters with respect to depth. Figure 30a shows how the minimum thickness increases with depth, because of the reduction of buoyancy. This increase is stronger in colder environments. Figure 30b shows that for the warm basin the mass stored increases with depth as expected for unfractured media. However, for cold basins, the behavior is non-monotonic with depth and at greater depth less CO_2 can be stored per aquifer area keeping everything else unchanged, because the reduced buoyancy requires a larger minimum thickness and the capillary fringe is spread over a larger distance.

Table 3 Parameters for the sensitivity analysis

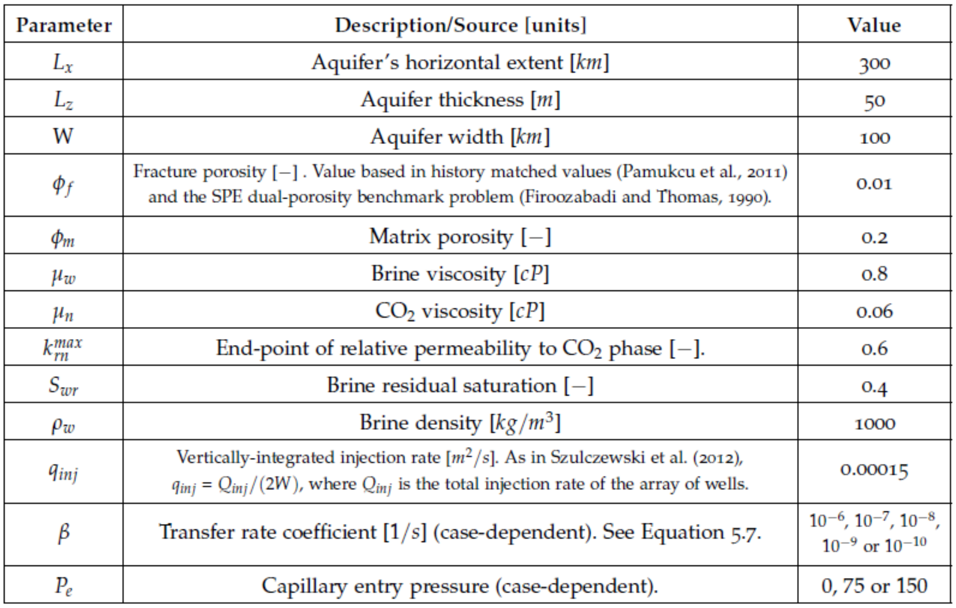

Parameter	Description/Source [units]	Value
L_x	Aquifer's horizontal extent [km]	300
L_z	Aquifer thickness [m]	50
W	Aquifer width [km]	100
ϕ_f	Fracture porosity [$-$] . Value based in history matched values (Pamukcu et al., 2011) and the SPE dual-porosity benchmark problem (Firoozabadi and Thomas, 1990).	0.01
ϕ_m	Matrix porosity [$-$]	0.2
μ_w	Brine viscosity [cP]	0.8
μ_n	CO_2 viscosity [cP]	0.06
k_{rn}^{max}	End-point of relative permeability to CO_2 phase [$-$].	0.6
S_{wr}	Brine residual saturation [$-$]	0.4
ρ_w	Brine density [kg/m^3]	1000
q_{inj}	Vertically-integrated injection rate [m^2/s]. As in Szulczewski et al. (2012), $q_{inj} = Q_{inj}/(2W)$, where Q_{inj} is the total injection rate of the array of wells.	0.00015
β	Transfer rate coefficient [$1/s$] (case-dependent). See Equation 5.7.	10^{-6}, 10^{-7}, 10^{-8}, 10^{-9} or 10^{-10}
P_e	Capillary entry pressure (case-dependent).	0, 75 or 150

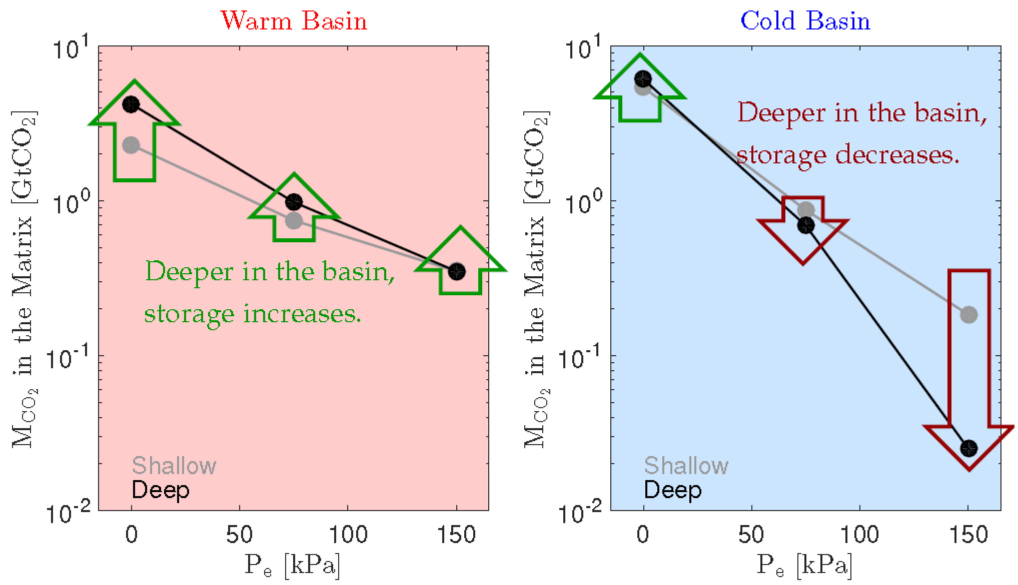

Figure 29: the mass M_{CO_2} of CO2 stored for shallow and deep reservoirs in warm (left) and cold basins against capillary entry pressure (P_e).

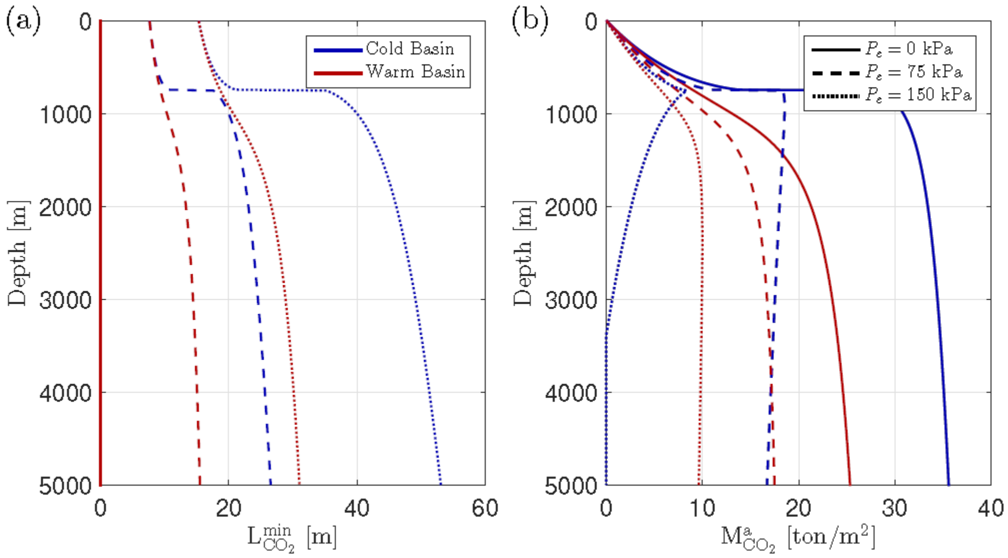

Figure 30 Depth profiles of (a) $L^{min}_{CO_2}$ and (b) $M^a_{CO_2}$ for warm basins (red curves) and cold basins (blue curves) for different capillary entry pressures (solid curves correspond to $P_e = 0$ kPa, dashed curves to $P_e = 75$ kPa and dotted curves to $P_e = 150$ kPa).

In addition, the impact that a system of fractures would have on storage is evaluated, based on realistic aquifer parameters taken from the literature. This analysis is based on the work of Szulczewski et al. (2012), where the CO2 storage potential in the U.S. was evaluated by considering a set of large aquifers that were identified in sedimentary basins across the country.

While there is no evidence of fractures in these aquifers, they represent a set of aquifers with different properties and are located in different geological environments that can be used to understand the impact of fractures on industrial scale storage of CO_2. Due to the increased permeability of fractures the maximally possible injection rate in the given scenarios increases. Figure 31 illustrates the change in terms of percentage for the considered aquifers. The relative improvement depends on the specific circumstances. The shape and magnitude of the pressure profile and hence the nature of the limitation depends on the interplay of aquifer geometry, permeability, porosity and caprock features. In particular aquifers with a low injectivity can benefit from fractures. However, if the fracturing pressure is only slightly larger than the reservoir pressure as seen in Madison (a) the relative improvement is not as strong.

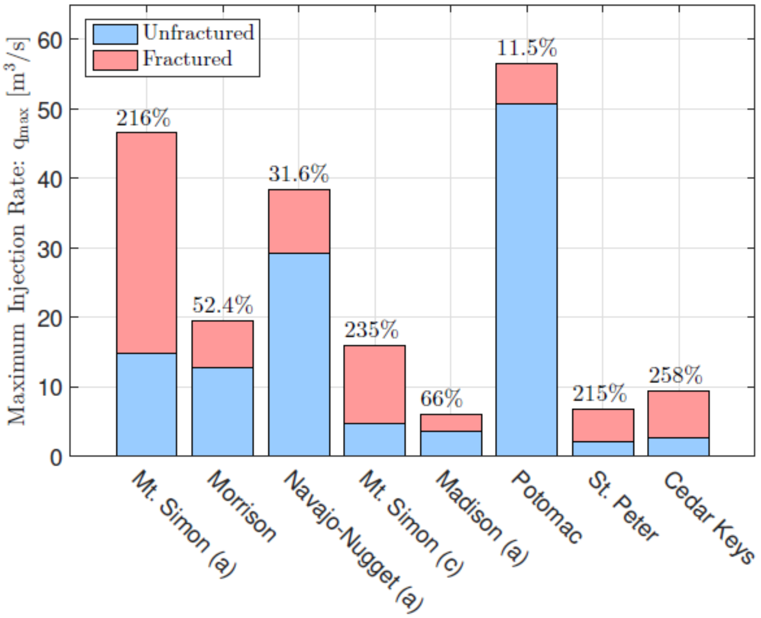

Figure 31 Maximum injection rate for the fractured (red) and unfractured (blue) models of each aquifer. Percentage increase caused by fractures in injectivity is seen at the top of each bar.

However, the increased injection rate does not translate into increased storage. Due to the fractures only a fraction of the pore-space is accessible for the CO_2, because of the adverse effects of capillarity that keep CO_2 preferentially in the matrix. To assess this impact three simulations were run for each aquifer. In all cases the injection rates have been calculated using a simulator developed in MRST and presented in the appendix of March (2018).

- Unfractured model: a single-porosity simulation of an unfractured aquifer with pressure-limited injection rates q_{PL}^{u}.
- Fractured model with pressure-limited injection rates: a dual-porosity simulation with pressure-limited injection rates q_{PL}^{f}.
- Fractured model with migration-limited injection rates: a dual-porosity simulation with migration-limited injection rates (q_{ML}^{f}). Injection rate is reduced from q_{PL}^{f} so that the CO_2 plume tip in the fractures does not reach the boundary of the aquifer at the end of the

injection period, that is, there is no CO2 lost through the boundary during the injection phase. However, after the injection has stopped some CO2 can be lost due to the redistribution of the plume. The pressure-limited rates serve as a maximum for calculating the migration-limited rates.

Two key variables that determine the efficiency of storage in each model are analyzed: the fraction of mass ($M_{CO_2}^{\%}$) of CO2 that is safely stored in the aquifer and the mass stored in the aquifer (M_{CO_2}).

Figure 32 shows $M_{CO_2}^{\%}$ plotted against M_{CO_2} for all the models considered. Many of the aquifers show an expected trend (see, for instance, the Potomac aquifer): the unfractured model has a higher M_{CO_2} with the pressure-limited model coming reasonably close. The high M_{CO_2} for the pressure-limited model is achieved at the cost of spilling some CO2 through the boundary (note the green square close to the circle, but slightly below the $M_{CO_2}^{\%} = 100\%$ line).

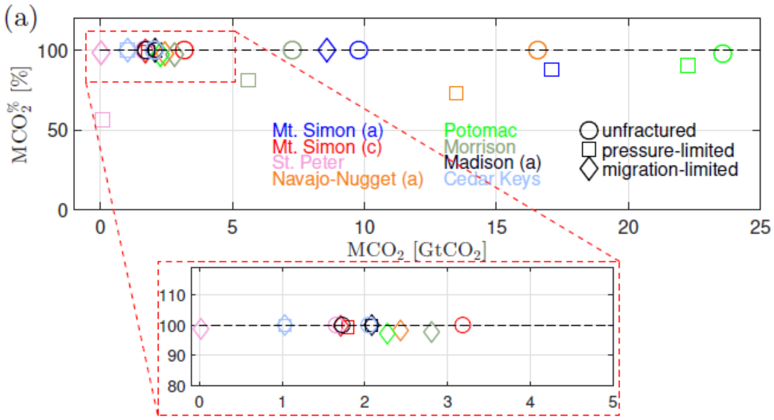

Figure 32 Summary of storage results for each case (unfractured, pressure-limited and migration-limited) and each aquifer. The fraction $M_{CO_2}^{\%}$ of mass of CO2 that is safely stored in the aquifer is plotted against the mass M_{CO_2}. The difference has escaped the domain through the boundaries due to the increased mobility. A zoom-in on the clustered points below.

When injection rates are injection-limited, the plume tends to be thinner in the fractures. This significantly reduces the buoyant force that drives CO2 into the matrix and, hence, M_{CO_2} (note that for Potomac the migration-limited M_{CO_2} is approximately a factor of 10 smaller). It is interesting to see, however, that most of the pressure-limited rates lead to a small spill, and hence, the pressure-limited rates could be explored if there is a reasonable confidence about a sealing aquifer boundary. The improved injectivity compensates for the loss in accessible pore space in most of the considered cases. Hence, for Potomac, Madison (a), Navajo-Nugget (a) and Mt. Simon aquifers, fractures do not significantly impact the storage (squares are close to the circles for these aquifers and just slightly below the 100% line).

Mt. Simon and Madison are interesting cases that show, that fractures can be beneficial for CO2 storage depending on the geological scenario and rock properties. For the Madison aquifer, simulations show that storage is slightly higher for the fractured models than for the unfractured model. This aquifer has one of the lowest injection rates. Hence, the increase in injectivity caused by the presence of a system of fractures leads to a wider plume in the fracture with an increased storage in the matrix. A deep CO_2 penetration depth, due to large aquifer thickness and high $\Delta\rho$ helps the drainage of the matrix. A similar behavior is seen for the Mt. Simon aquifer, where the fractured model with pressure-limited rates leads to a storage that is 150% higher than the unfractured model. The migration-limited case shows a stored mass only slightly smaller than the unfractured model, but leads to no spill through the boundary.

In summary, this section provides tools for a quick assessment of storage potential in large fractured aquifers. These tools were used to investigate the impact of fractures in real aquifers taken from the literature, with interesting findings. Although fractures will typically lead to a decrease in storage, this decrease will not generally exceed one order of magnitude. Therefore, large fractured aquifers seem to be suitable for storage and should be evaluated on a case-by-case basis.

2.4.6 Impact of rock matrix block shape and size on storage of dissolved CO_2

The diffusive flux equation, described by equations (1a-b) and (2a-c), was used to calculate dissolved CO_2 (dCO_2) storage efficiency, as function of time and space, at the representative elementary volume (REV) and reservoir scale. The REV may contain a collection of identical matrix blocks or matrix blocks with different shapes, sizes, and properties. The details of the modeling setup and results can be found in Zhou et al. (2017b). Figure 33 shows the normalized storage efficiency of dCO_2, as function of time and minimum fracture half-spacing, in REVs with uniform matrix blocks or collection of blocks with different sizes. For fracture half-spacing of 0.5 m, the dCO_2 storage can reach quasi-equilibrium in 10 years, indicating that solubility trapping is effective in such fractured reservoirs. Figure 34 shows the dCO_2 plume at 5, 25, 50 years in a one-dimensional radial fractured reservoir with the rock matrix represented by single-size cubes, four-size cubes, and single-size rectangular parallelepipeds with $R_{l2} = 0.5$ and $R_{l3} = 0.2$, with the minimum half-fracture spacing of 0.25, 0.50, and 1.0 m. Figure 34 also shows the comparison of the time-dependent ratio between dCO_2 mass stored in the rock matrix and the free-phase CO_2 mass stored in the fractures for all the nine scenarios, as well as the dual-porosity model with optimal rate coefficient for the four-cube case with $l = 1.0$ m.

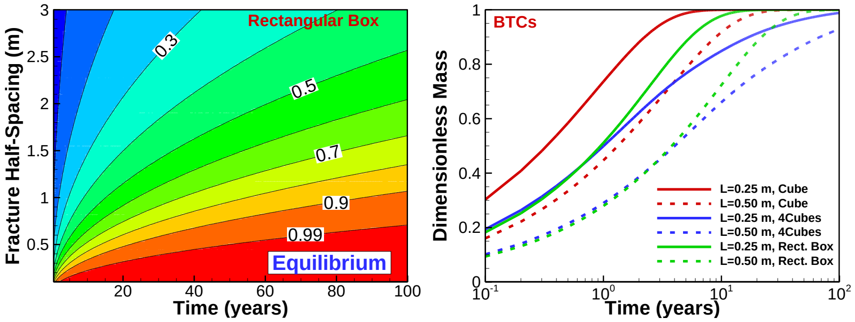

Figure 33: Dimensionless mass fraction of dCO_2 as a function of time and minimum fracture half-spacing for a rectangular parallelepiped (left), and the time profile of normalized storage efficiency (right) for three cases (1 cubical matrix block, 4 cubical blocks, and 1 3-D rectangular block) and two different minimum fracture half-spacing. Modified from Zhou et al. (2017b).

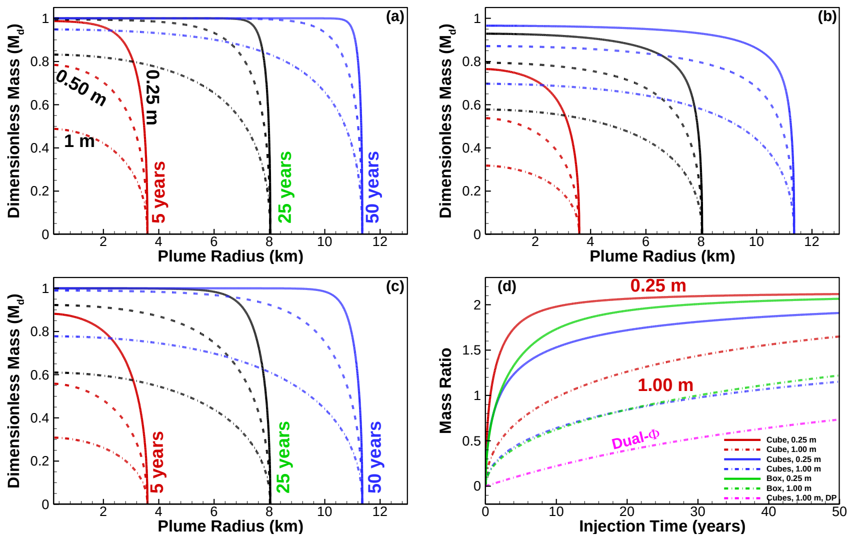

Figure 34: Profiles of dCO_2 dimensionless mass at 5, 25, 50 years in the rock matrix with (a) single-size cubes, (b) four-size cubes, and (c) single-size anisotropic rectangular parallelepipeds with $R_{l2} = 0.5$ and $R_{l3} = 0.2$, with the minimum half-fracture spacing of 0.25, 0.50, and 1.0 m, and (d) comparison of the time-dependent ratio between dCO_2 mass stored in the rock matrix and the free-phase CO_2 mass stored in the fractures for all the scenarios with 0.25 m and 1.0 m fracture half-spacing, as well as the dual-porosity model with optimal rate coefficient for the four-cube case with $l = 1.0$ m. Taken from Zhou et al. (2017b).

By comparison, the dual-porosity model significantly underestimates the dynamic storage efficiency of dCO_2. The dual-porosity model is represented by $M_d = 1 - \exp(-b_{21}t_d)$ and cannot capture the large diffusive mass flux in the early-time regime. Unlike the $\sqrt{t_d}$-behavior of the cumulative flux in equation (1a) in the very-early time regime with $t_d < 0.01$, the dual-porosity model predicts the t_d-behavior (see Figure 35). The optimal rate coefficient used in the dual-porosity model is b_{21} in equations (1b) and (2c).

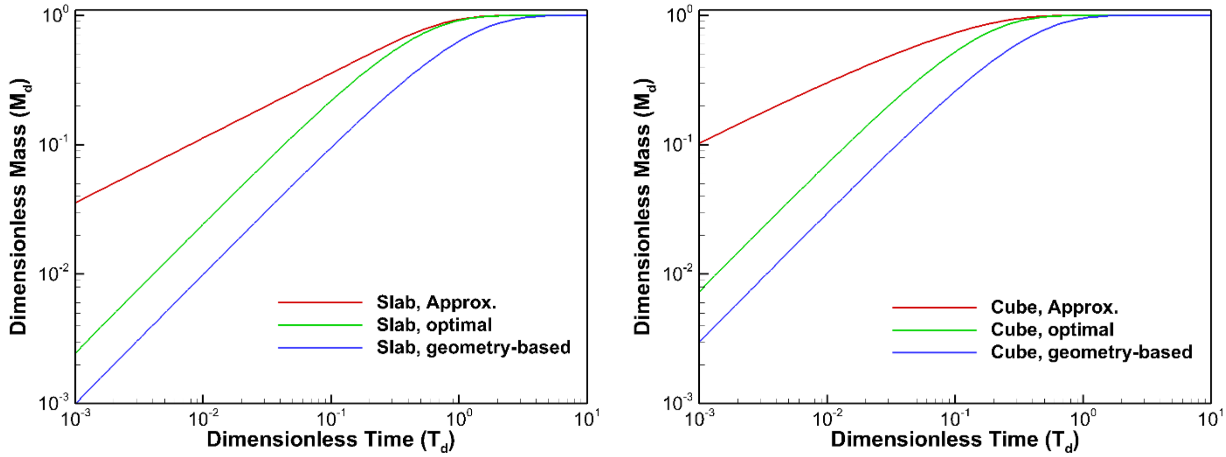

Figure 35: Comparison of the approximate solutions to two first-order dual-porosity models (in green and blue) with geometric-based and optimal rate coefficients for a slab-like and cubical block. Taken from Zhou et al. (2017b).

The developed diffusive flux equation in equations (1-2) can accurately calculate the time-dependent storage efficiency of dCO_2. The calculations for the REV and reservoir-scale storage efficiency indicates that solubility trapping can be effective in fractured reservoirs with low matrix permeability and high entry capillary pressure, as long as the fracture spacing is smaller than 1.0 m. More details of the solution development and example demonstration can be found in Zhou et al. (2017b), Zhou et al. (2017a) and Zhou et al. (2019c).

2.5 Modeling at the In Salah site

At the In Salah CO_2 storage site, the storage formation is a fractured reservoir with both natural fractures (Iding & Ringrose, 2010) and newly induced fractures caused by CO_2 injection from 08/2004 to 06/2011 (Rucci et al., 2013). Large amounts of characterization data (e.g., well logs, core permeability and porosity measurements, measured capillary pressure and relative permeability functions) and the most recent geologic model (developed using 3D seismic survey data) with spatial distribution of matrix porosity and permeability are available. Figure 36 shows the region with three horizontal wells (KB-501, 502, and 503) for CO_2 injection, the surface deformation (induced by CO_2 injection) between 9/18/2010 and 11/29/2003, the natural gas field, the other horizontal gas production wells and vertical wells, and faults.

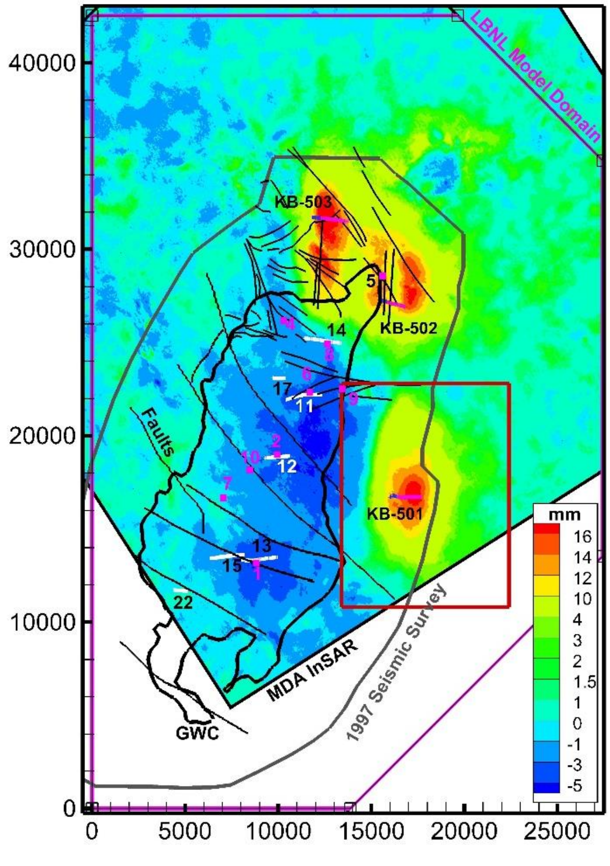

Figure 36: The region with three CO_2 injection wells (KB-501, 502, and 503 in pink lines) and nearby natural gas field with horizontal production wells (11, 12, 13, 14, 15, 17, and 22 in while lines), vertical wells with core data (in pink squares), faults (in thin black lines), gas-water

contact (GWC, in thick black line), the edge of the 1997 seismic survey domain (in gray line), the boundary of the site-scale model domain, and the flooded contour of surface deformation between 09/18/2010 and 11/29/2003, as well as the InSAR data boundary (MDA InSAR). The length unit is meter, and the relative coordinates are transformed by rotating 45° in the clockwise direction. The red rectangle is the model domain for this study with a focus on KB-501.

Figure 37 shows the top and bottom elevation of the storage reservoir (i.e., C10.2) in terms of the true vertical depth below sea level and Figure 38 shows the distribution of matrix porosity and permeability for 6 geological layers of storage reservoir C10.2 based on the 2012 BP geological model. The resolution of matrix porosity and permeability is 400 m × 400 m. The matrix permeability around the three wells varies from less than 5 mD to 45 mD and the matrix porosity varies from 0.15 to 0.20.

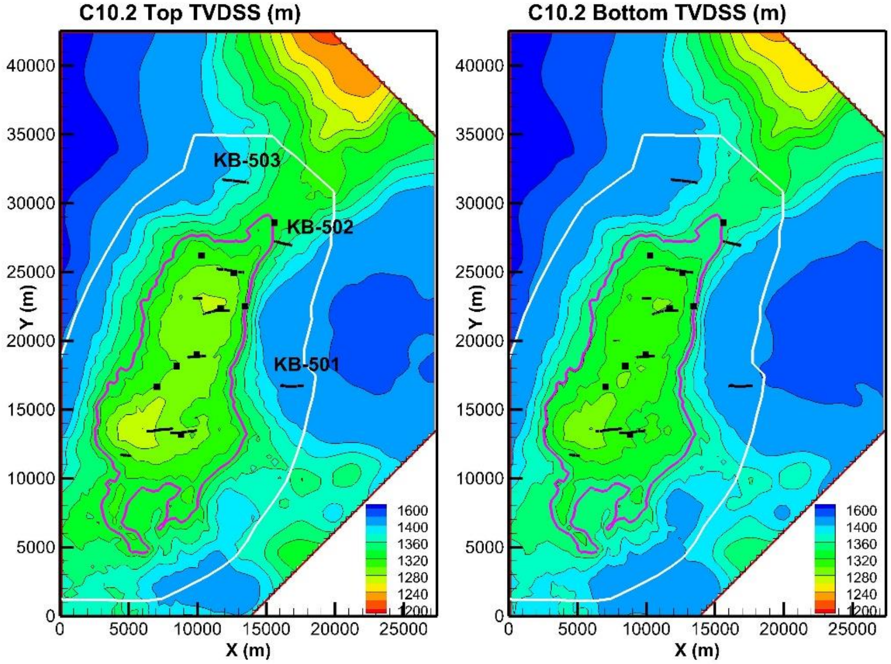

Figure 37: Top and bottom elevation of storage reservoir C10.2 in terms of the true vertical depth below sea level (TVDSS).

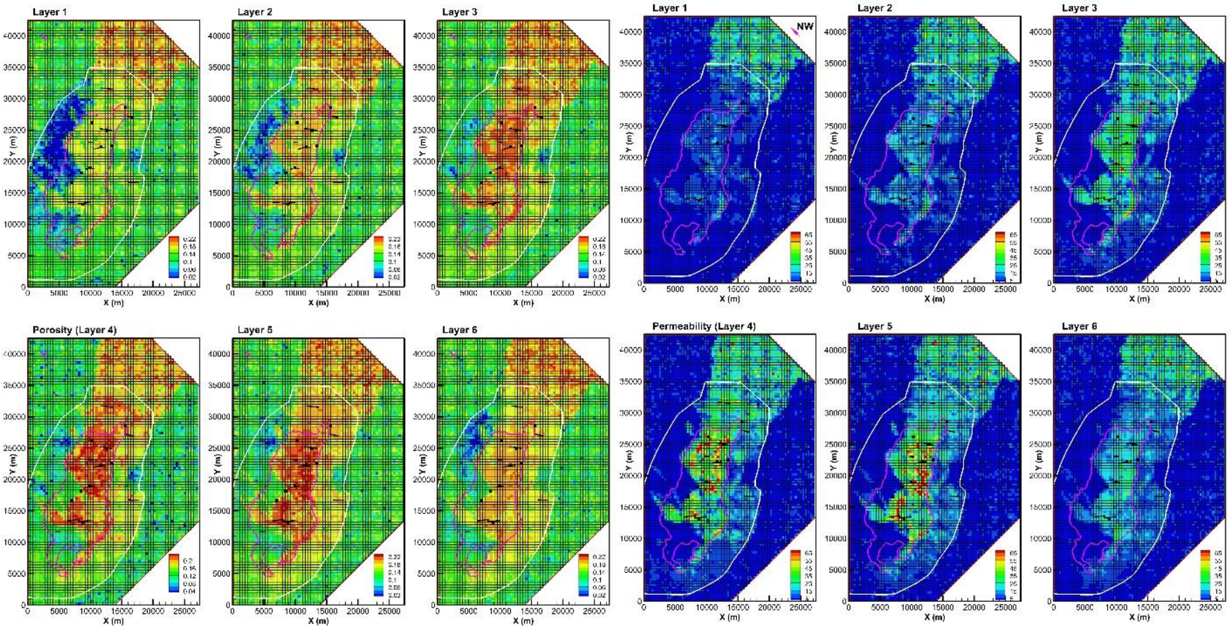

Figure 38: Distribution of matrix porosity (left six panels) and permeability (right six panels) for six geological layers of storage reservoir C10.2 based on the 2012 BP geological model.

This study focuses on CO_2 injection and storage at KB-501, one of the three horizontal injection wells. Figure 39 shows the hourly injection rate and wellhead pressure monitored at KB-501. For this modeling study, a step-rate injection scheme approximates the strong temporal variations. The total injected CO_2 mass for KB-501 is 1.072 million metric tons. The monitoring data available include snapshots of monthly surface deformation obtained by the InSAR technique and wellhead pressure and temperature at KB-501.

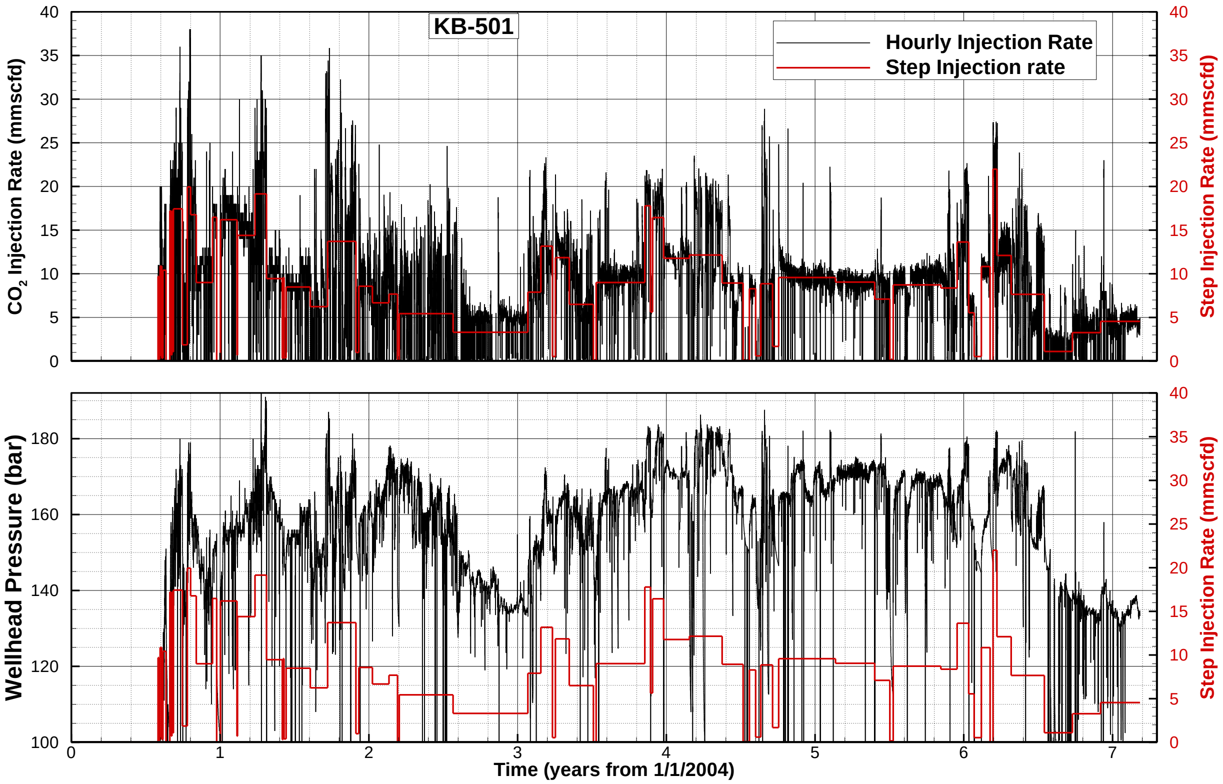

Figure 39: Hourly CO_2 injection rate (10^6 scfd, or standard cubic feet per day) and wellhead pressure (bar) monitored for injection well KB-501, and step-rate injection rate used in the modeling.

A TOUGH2 model was developed to focus on the KB-501 region, where injection-induced geomechanical damage was limited. The model domain shown by the red rectangle in Figure 36 is 12 km × 14 km. Figure 40a shows the plan view unstructured mesh with 2,539 cells whose size varies from 800 m × 1200 m along the model boundary to 50 m × 5 m along the horizontal well. The horizontal injection well is 1,350 m long and is represented by 27 cells in the x (transformed easting) direction. Figure 40b shows the three-dimensional mesh covering the six layers of storage reservoir C10.2, two layers of caprock C10.3 and one layer of baserock D70, as well as one reservoir layer for the injection well, leading to a total of 33804 three-dimensional cells.

The primary three-dimesional mesh was used to generate the three-dimensional mesh for the fracture and matrix continua. For each primary cell there are one fracture cell and four matrix subcells. The four matrix subcells are nested to more accurately simulate the intra-matrix block flow for each matrix block. The volume fraction of the matrix subcells from the outmost to the innermost one is 0.08, 0.2, 0.35, and 0.36, while the volume fraction of the fracture cell is 0.01. The generated MINC mesh with fracture cells and matrix subcells was further modified to allow for CO_2 and brine flow between matrix blocks by adding a connection between two neighboring innermost matrix subcells. In this way, the flow of displaced brine between matrix blocks was simulated and the matrix-matrix connectivity and capillary continuity were maintained. As a result, the CO_2 storage in the matrix continuum is more realistic than the traditional MINC model.

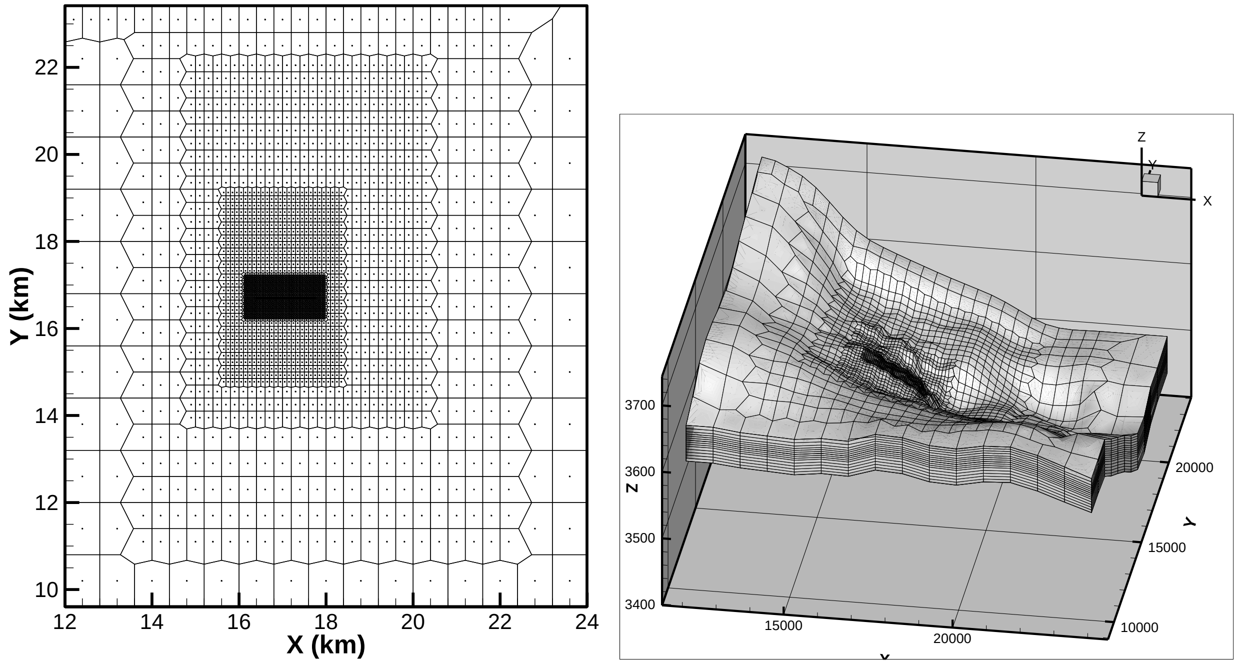

Figure 40: (Left, a) plan view of unstructured mesh with local refinement along the horizontal injection well, and (right, b) three-dimensional mesh. Note that the z coordinate in the 3-D mesh is elevation + 2000 m.

The spatially distributed rock-matrix properties from the geologic model and the historic injection rate were directly used. A set of fracture-matrix geometric parameters (i.e., fracture spacing of 1 m) was used. The simulations were conducted for six years of CO_2 injection and four years after the injection. Figure 41 shows the CO_2 saturation in the fracture continuum during the injection and post-injection periods. The fracture CO_2 plume migrates to the west, following the spatially varying top elevation of the storage formation (see Figure 37 and Figure 40b), and reaches the left boundary, which is located in the natural gas field. CO_2 saturation can be as high as 60% as the fracture residual saturation of 0.30 was used to represent the filling of fractures. After the injection stops, the fracture CO_2 plume further migrates to the left boundary. Indeed, field observations show that the CO_2 injected at KB-502 arrived at KB-14, a gas production well (see Figure 36), by the end of CO_2 injection. Even though the fracture CO_2 plume is large, the total mass in the fracture continuum is relatively small, accounting for 18.5% of the total injected CO_2 mass by the end of CO_2 injection. The remaining injected CO_2 mass (81.5%) is stored in the rock matrix of the storage formation, even though the matrix CO_2 plume (Figure 42) is much smaller than the fracture CO_2 plume. This is because the intrinsic matrix porosity is on the order of 0.20 and the volume fraction of the matrix continuum is 0.99. The maximum matrix CO_2 saturation is ~0.40 around the horizontal injection well. Outside of the main matrix plume, the matrix CO_2 saturation is relatively small, depending on the time scale when fracture CO_2 arrives and CO_2 invasion into the matrix continuum starts to occur. Around the injection well, CO_2 invasion becomes stronger with time, and matrix CO_2 saturation increases. The details of multiple simulations and comparison with single-continuum (matrix) simulations will be documented in (Zhou et al., 2019a).

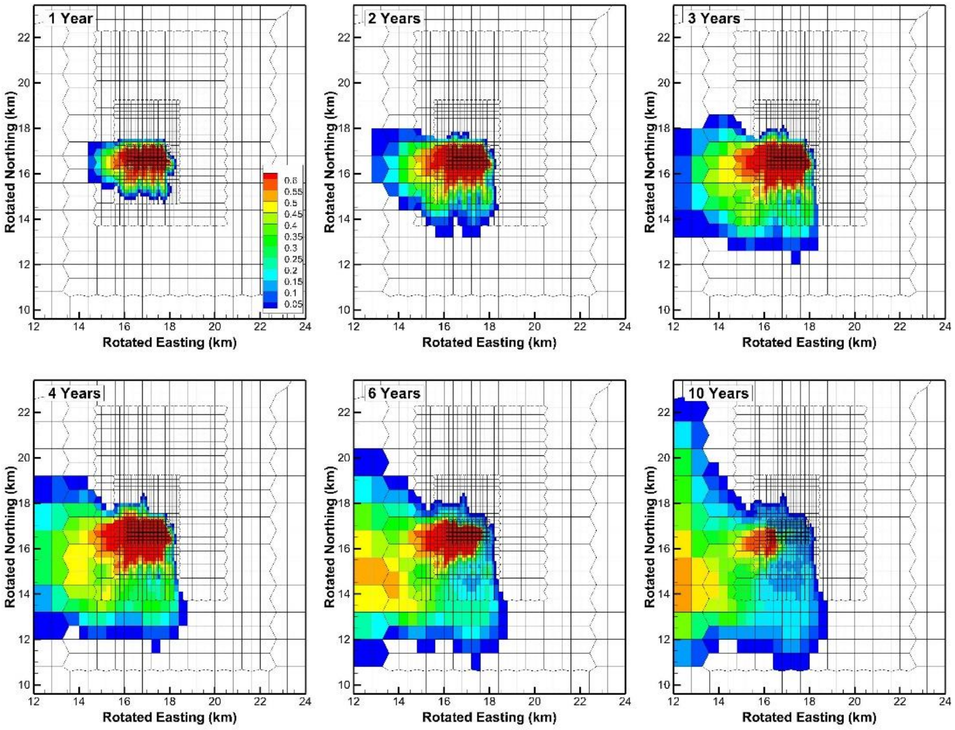

Figure 41: CO_2 saturation in the fracture continuum during the first six years of CO_2 injection and four post-injection years.

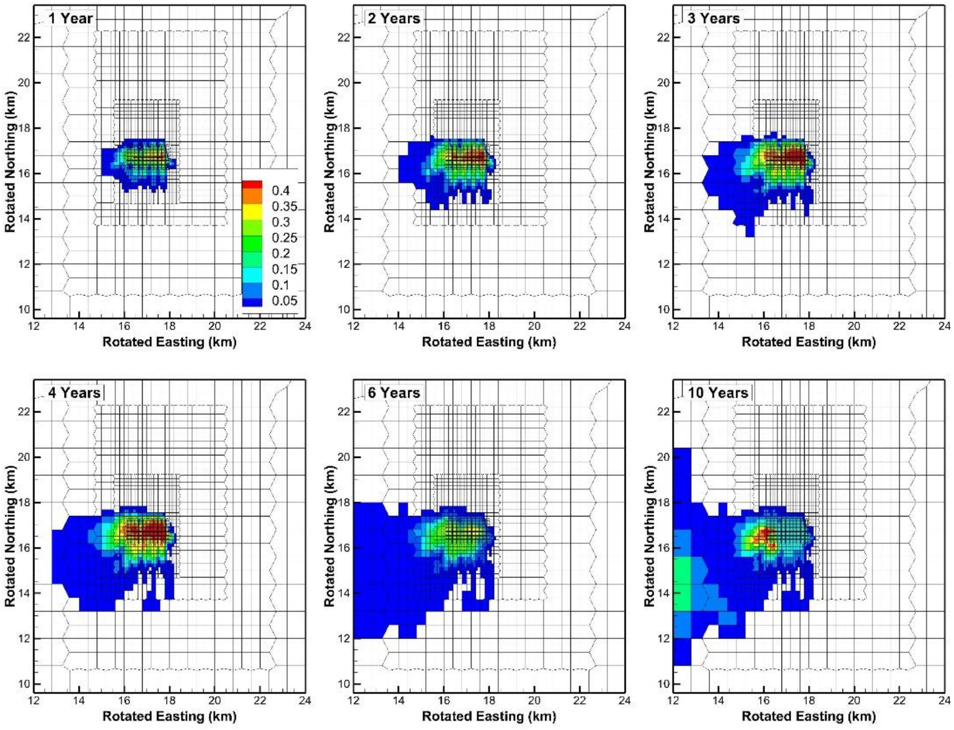

Figure 42: CO_2 saturation in the matrix continuum during the first six years of CO_2 injection and four post-injection years.

2.6 Conclusion

This report documents the successful completion of the project titled "Multiscale Modeling of CO_2 Migration and Trapping in Fractured Reservoirs with Validation by Model Comparison and Real-Site Applications" funded thought the National Energy and Technology Laboratory of the US Department of Energy. Fractured reservoirs are increasingly being investigated for geologic carbon storage, due to the wide distribution of carbonate reservoirs, which are often naturally fractured. Modeling of fractured reservoirs has a long history in the context of petroleum engineering. Directly representing the fractures is usually not possible due to prohibitively high computational efforts. Therefore, the dual-continuum approach is usual employed for modeling of fractured reservoirs. In this approach, the model is split into two continua: one representing the fractures and one representing the rock matrix. The two continua are connected by mass transfer between the two continua.

In this project new mass transfer functions were developed, both for free-phase and dissolved CO_2, to enable dual-continuum approaches to be applied to CO_2-brine systems. The mass transfer functions for free-phase CO_2 include gravity drainage and spontaneous imbibition as mass transfer processes. Gravity drainage of rock matrix blocks is relevant during the CO_2 injection phase, when the rock matrix blocks will be filled by brine and the fractures will be filled by CO_2. The mass transfer function is based on vertical displacement of brine by CO_2, and comparisons of the new mass transfer function to highly resolved model results show good agreement.

A second mass transfer function – based on spontaneous imbibition – was developed for the post-injection period, when the CO_2 plume has migrated away from the injection site, so that rock matrix blocks with high CO_2 saturation are surrounded by fractures with high brine saturation. In this case, brine will displace CO_2 in the matrix blocks due to capillary forces, as the pores in the rock matrix are much smaller than in the fractures and brine is the wetting phase in this system. A hybrid mass transfer function was developed based on spontaneous imbibition, with the early-time solution based on $\sqrt{t}$ scaling and the late-time solution based on a self-similar solution. The switchover time is determined based on reservoir properties. A comparison of this newly developed model showed good agreement with highly resolved numerical experiments. Both of the newly development mass transfer functions were implemented in the Matlab Reservoir Simulation Toolbox (MRST).

In addition to the mass transfer functions for free-phase CO_2, mass transfer functions were also developed for the migration of dissolved CO_2 into matrix blocks, which may be an important storage mechanism in fractured reservoirs with low permeability or high capillary entry pressure of the rock matrix. The form of the new dissolved mass transfer functions are based on existing series solutions for diffusion into blocks with simple geometries (e.g., spheres). Research conducted during this project found that for the case of CO_2 diffusing into brine-filled matrix blocks, the solutions can be significantly simplified by only using the first three terms for the early-time behavior and an exponential solution for the late-time regime. It was also found, that diffusion into more complex shapes can also be described by this form of solution, although the coefficients for these solutions may need to be determined numerically for some shapes. This new solution has been shown to give good results for the following rock matrix block shapes: slab, rectangle, rectangular parallelepiped, sphere, cylinder, and two- and three-dimensional rectangular blocks. These new solutions were implemented the Fortran library SHPALib (Solute and Heat Transport and Pressure Propagation: An Analytical Solutions Library).

In addition to developing new mass transfer functions, a new vertically-integrated dual-continuum modeling approach was developed. This modeling approach takes advantage of the large density difference between CO_2 and brine (~500 kg/m^3) and the expected high permeability of the fractures. This combination results in fast vertical segregation of CO_2 and brine, so that the vertical equilibrium assumption is likely valid in the fracture continuum. Therefore, the fracture continuum is represented by a vertically-integrated model, while the rock matrix continuum is represented by conventional three-dimensional models. The mass transfer functions needed to be vertically-integrated to allow for coupling of the vertically-integrated fracture continuum to the vertically-distributed rock matrix continuum. Implementations of sugar cube and dual-permeability conceptualizations of the rock matrix coupled to the vertically-integrated fractures show very good agreement for cases where the vertical equilibrium assumption is valid in the fracture continuum. The matchstick conceptualization was also implemented, however developing an integrated mass transfer function for this case was beyond the scope of this project; using the mass transfer function developed for the matchstick conceptualization led to good results for narrow matchsticks with higher permeabilities.

Newly developed and existing models were used to conduct several sensitivity analyses to better understand geologic carbon storage in fractured reservoirs and to investigate conditions favorable for CO_2 storage in fractured reservoirs. One study investigated the impact of continuous capillary connections of stacks of matrix blocks and showed that storage is much higher if the matrix blocks have capillary connections than if they are separated, especially for short matrix block with high capillary entry pressures. The results also showed that matrix blocks did not need to be connected over their entire interface, as models with 30% connectivity had very similar results to models with full connectivity. Another study looked at how much the storage capacity of an anticline would be reduced if fractures had not been detected during site characterization. The storage volume was reduced by about 33% compared to the unfractured case, mainly because CO_2 migrated quickly along the highly permeable fractures to the top of the anticline, significantly reducing the sweep of the pore space. The same anticline model was used to study the impact of CO_2 injection rate on storage capacity of fractured reservoirs. It was found, that low injection rates lead to slower moving CO_2 plumes, which allows more time for CO_2 to be transferred to the rock matrix, before CO_2 reached the spill-point. Storing CO_2 in the rock matrix is better than in the fractures, because the rock matrix has a larger storage volume and lower permeability. The impact of different storage conditions (temperature and pressure) and different rock properties (permeability, porosity, residual saturation, …) on CO_2 storage was investigated based on values from the literature, and it was shown that the time needed to drain 95% of the resident brine out of a matrix block is a good predictor of storage potential, with longer times correlating to larger storage amounts. An additional study showed that while fractures often reduce storage capacity due to fast CO_2 migration through the fractures, the high permeability of the fractures can also be beneficial for injection operations, because higher injection rates are possible before fracture pressure is reached. A study of storage of dissolved CO_2 showed that smaller matrix blocks reach their storage potential faster. This is different from storage of free-phase CO_2, where capillary forces may reduce storage potential of smaller rock matrix blocks.

The newly developed modeling capabilities were demonstrated by simulating CO_2 migration at the In Salah site, where CO_2 was injected into a fractured reservoir for six years. To better represent matrix-matrix interaction, the MINC matrix block representation in TOUGH2 was enhanced to allow for interactions between the innermost subcells of neighboring matrix blocks. The model domain focused on well KB-501 and covered an area of 12 x 14 km, with a total of 33804 three-dimensional cells. The results show that CO_2 migrates quickly along the fractures following the caprock topography. This migration pattern is consistent with observations at the site. However, less than 20% of the injected CO_2 mass resides in the fractures, suggesting that safe storage can be achieved in fractured reservoirs.

Overall, the results of this project show that dual-continuum modeling approaches are well suited for modeling of geologic carbon storage in naturally fractured reservoirs. The newly developed mass transfer functions – both for free-phase and dissolved CO_2 – are able to accurately predict the mass transfer of CO_2 and brine between fractures and the rock matrix. Application of the models showed that industrial-scale CO_2 storage is feasible in fractured reservoir under the right reservoir and operational conditions.

3 List of Figures

4 List of tables

5 References

Barenblatt, G., Zheltov, I. P., & Kochina, I. (1960). Basic concepts in the theory of seepage of homogeneous liquids in fissured rocks [strata]. *Journal of applied mathematics and mechanics, 24*(5), 1286-1303.

Bennion, D. B., & Bachu, S. (2008). Drainage and imbibition relative permeability relationships for supercritical CO2/brine and H2S/brine systems in intergranular sandstone, carbonate, shale, and anhydrite rocks. *Spe Reservoir Evaluation & Engineering, 11*(3), 487-496.

Carslaw, H. S., & Jaeger, J. C. (1959). *Conduction of Heat in Solids* (2nd ed.). Oxford, UK: Clarendon.

Coats, K. H. (1989). *Implicit compositional simulation of single-porosity and dual-porosity reservoirs.* Paper presented at the SPE Symposium on Reservoir Simulation.

Court, B., Bandilla, K. W., Celia, M. A., Janzen, A., Dobossy, M., & Nordbotten, J. M. (2012). Applicability of vertical-equilibrium and sharp-interface assumptions in CO_2 sequestration modeling. *International Journal of Greenhouse Gas Control, 10*, 134-147. doi:10.1016/j.ijggc.2012.04.015

Crank, J. (1975). *The Mathematics of Diffusion* (2nd ed.). New York: Oxford University Press.

Di Donato, G., Tavassoli, Z., & Blunt, M. J. (2006). Analytical and numerical analysis of oil recovery by gravity drainage. *Journal of Petroleum Science and Engineering, 54*(1-2), 55-69.

Gilman, J. R. (1986). An efficient finite-difference method for simulating phase segregation in the matrix blocks in double-porosity reservoirs. *SPE Reservoir Engineering, 1*(4), 403-413.

Gilman, J. R., & Kazemi, H. (1988). Improved Calculations for Viscous and Gravity Displacement in Matrix Blocks in Dual-Porosity Simulators. *Journal of Petroleum Technology, 40*(1), 60-70.

Guo, B., Tao, Y. H., Bandilla, K., & Celia, M. (2017). Vertically integrated dual-porosity and dual-permeability models for CO_2 sequestration in fractured geological formation. *13th International Conference on Greenhouse Gas Control Technologies, Ghgt-13, 114*, 3343-3352. doi:10.1016/j.egypro.2017.03.1466

Iding, M., & Ringrose, P. (2010). Evaluating the impact of fractures on the performance of the In Salah CO_2 storage site. *International Journal of Greenhouse Gas Control, 4*(2), 242-248.

Kazemi, H., Merrill, L. S., Porterfield, K. L., & Zeman, P. R. (1976). Numerical-Simulation of Water-Oil Flow in Naturally Fractured Reservoirs. *Society of Petroleum Engineers Journal, 16*(6), 317-326.

Krogstad, S., Lie, K. A., Møyner, O., Nilsen, H. M., Raynaud, X., & Skaflestad, B. (2015). *MRST-AD–an open-source framework for rapid prototyping and evaluation of reservoir simulation problems.* Paper presented at the SPE reservoir simulation symposium.

Lim, K. T., & Aziz, K. (1995). Matrix-Fracture Transfer Shape Factors for Dual-Porosity Simulators. *Journal of Petroleum Science and Engineering, 13*(3-4), 169-178.

March, R. (2018). *Modelling of CO_2 Storage in Naturally Fractured Reservoirs.* (PhD), Heriot-Watt.

March, R., Doster, F., & Geiger, S. (2016). Accurate early-time and late-time modeling of countercurrent spontaneous imbibition. *Water Resources Research, 52*(8), 6263-6276.

March, R., Doster, F., & Geiger, S. (2018). Assessment of CO_2 Storage Potential in Naturally Fractured Reservoirs With Dual-Porosity Models. *Water Resources Research, 54*(3), 1650-1668. doi:10.1002/2017WR022159

March, R., Elder, H., Doster, F., & Geiger, S. (2017). *Accurate Dual-Porosity Modeling of CO_2 Storage in Fractured Reservoirs.* Paper presented at the SPE reservoir simulation conference.

Metz, B., Davidson, O., De Coninck, H., Loos, M., & Meyer, L. (2005). *International Panel on Climate Change Special Report on Carbon Dioxide Capture and Storage*. Cambridge: Cambridge University Press.

Pruess, K., & Narasimhan, T. N. (1985). A Practical Method for Modeling Fluid and Heat-Flow in Fractured Porous-Media. *Society of Petroleum Engineers Journal, 25*(1), 14-26.

Ramirez, B., Kazemi, H., Al-Kobaisi, M., Ozkan, E., & Atan, S. (2009). A Critical Review for Proper Use of Water/Oil/Gas Transfer Functions in Dual-Porosity Naturally Fractured Reservoirs: Part I. *Spe Reservoir Evaluation & Engineering, 12*(2), 200-210. doi:Doi 10.2118/109821-Pa

Rucci, A., Vasco, D. W., & Novali, F. (2013). Monitoring the geologic storage of carbon dioxide using multicomponent SAR interferometry. *Geophysical Journal International, 193*(1), 197-208.

Szulczewski, M. L., MacMinn, C. W., Herzog, H. J., & Juanes, R. (2012). Lifetime of carbon capture and storage as a climate-change mitigation technology. *Proceedings of the National Academy of Sciences of the United States of America, 109*(14), 5185-5189.

Tao, Y. (2017). *Vertically-Integrted Dual-Continuum Models for CO_2 Injection in Fractured Geological Formations.* (Master of Science), Princeton University.

Tao, Y., Guo, B., Bandilla, K. W., & Celia, M. A. (2018). Vertically-integrated Dual-continuum Models for CO_2 Injection in Fractured Geological Formations. *Computational Geosciences, accepted.*

van Genuchten, M. T. (1980). A Closed-Form Equation for Predicting the Hydraulic Conductivity of Unsaturated Soils. *Soil Science Society of America Journal, 44*(5), 892-898.

Warren, J. E., & Root, P. J. (1963). The Behavior of Naturally Fractured Reservoirs. *Society of Petroleum Engineers Journal, 3*(3), 245-255.

Zhou, Q., Oldenburg, C. M., & Birkholzer, J. T. (2019a). A hybrid discrete-continuum model for modeling supercritical CO_2 storage in fractured reservoirs. *Water Resources Research, to be submitted.*

Zhou, Q., Oldenburg, C. M., & Birkholzer, J. T. (2019b). Multirate invasion of supercritical CO_2 in fractured reservoirs: Effects of buoyancy and matrix capillary continuity. *Water Resources Research, to be submitted.*

Zhou, Q., Oldenburg, C. M., & Rutqvist, J. (2019c). Revisiting the analytical solutions of heat transport in fractured reservoirs using a generalized multirate memory function. *Water Resources Research, submitted.*

Zhou, Q. L., Oldenburg, C. M., Rutqvist, J., & Birkholzer, J. T. (2017a). Revisiting the Fundamental Analytical Solutions of Heat and Mass Transfer: The Kernel of Multirate and Multidimensional Diffusion. *Water Resources Research, 53*(11), 9960-9979.

Zhou, Q. L., Oldenburg, C. M., Spangler, L. H., & Birkholzer, J. T. (2017b). Approximate solutions for diffusive fracture-matrix transfer: Application to storage of dissolved CO_2 in fractured rocks. *Water Resources Research, 53*(2), 1746-1762.

6 Appendix

6.1 Journal publications, book chapters and presentations resulting from this project

6.1.1 Journal publications

1. March, R., F. Doster, and S. Geiger (2016). Accurate early and late time modelling of counter-current spontaneous imbibition, *Water Resources Research,* 52 (8), pages 6263–6276*,* DOI: 10.1002/2015WR018456.
2. Zhou, Q., C.M. Oldenburg, L.H. Spangler, and J.T. Birkholzer (2016). Approximate Solutions for Diffusive Fracture-Matrix Transfer: Application to Storage of Dissolved CO_2 in Fractured Rocks. *Water Resources Research,* 53*,* 1746–1762.
3. Guo, B., Tao, Y., Bandilla, K.W., Celia, M.A. (2017). Vertically integrated dual-porosity and dual-permeability models for CO_2 sequestration in fractured geological formations. *Energy Procedia*, 114, 3343–3352.
4. Zhou, Q., Oldenburg, C.M., Rutqvist, J., Birkholzer, J.T. (2017). Revisiting the fundamental analytical solutions of heat and mass transfer: The Kernel of multirate and multidimensional diffusion. *Water Resources Research,* 53(11), pp. 9960–9979.
5. March, R., Elder, H., Doster, F., Geiger, S.: SPE-182646-MS Accurate Dual-Porosity Modeling of CO_2 Storage in Fractured Reservoirs.
6. March, R., F. Doster, and S. Geiger (2018). Assessment of CO_2 Storage Potential in Naturally Fractured Reservoirs with Dual-Porosity Models. *Water Resources Research*, 54(3), pp. 1650-1668, doi: 10.1002/2017WR022159.
7. Tao, Y., B. Guo, K.W. Bandilla, and M.A. Celia (2018). Vertically-integrated Dual-porosity Model for CO_2 Injection in Fractured Geological Formations. *Computational Geosciences* (accepted).
8. March, R., F. Doster, and S. Geiger (2018). CO_2 Storage Potential in Naturally Fractured Reservoirs. In preparation.
9. Zhou, Q., Oldenburg, C.M., Birkholzer, J.T. (2018). Buoyancy-driven invasion of supercritical CO_2 with matrix capillary continuity. In preparation.

6.1.2 Books or other non-periodical, one-time publications (2)

1. Bandilla, K.W., and Celia, M.A. (2018). Numerical modelling of fluid flow during geologic carbon storage. Chapter in "Science of Carbon Storage in Deep Saline Formations: Process Coupling Across Time and Spatial Scales", P. Newell and A. Ilgen, editors.

6.1.3 Other publications, conference papers and presentations (29)

1. Bandilla, K.W. (2015). Multiscale Modeling of Carbon Dioxide (CO_2) Migration and Trapping in Fractured Reservoirs with Validation by Model Comparison and Real-Site Applications. Presented at the Carbon Storage R&D Project Review Meeting in Pittsburgh, Pa (8/18-8/20/15).

2. Doster, F. (2015). Multi-scale multi-physics modelling of multi-phase flow phenomena in porous media. Presented at the Non-linearities and Upscaling in Porous Media (NUPUS) Conference in Freudenstadt, Germany (9/8 – 9/12/2015).
3. March, R. (2015). Analytical Solutions and Numerical Models for Early- and Late-time Imbibition in Fractured Reservoirs. Presented at the Foundation CMG Summit in Calgary, Canada (9/15 - 9/16/2015).
4. March, R. (2015). Analytical Solutions and Numerical Models for Early- and Late-time Imbibition in Fractured Reservoirs. Presented at the Challenges and Advancement in Reactive Flow and Carbonate Reservoir Simulation workshop at Heriot-Watt University.
5. March, R. (2015). Imbibition in multiple continuum representations of fractured porous media: Early and late time behavior. Presented at the 2015 American Geophysical Union Fall Meeting in San Francisco, CA (12/14-12/18/2015).
6. Zhou, Q. (2015). A Hybrid Continuum-Discrete Scheme for Simulating CO_2 Migration and Trapping in Fractured Sandstone Reservoirs. Presented at the 2015 American Geophysical Union Fall Meeting in San Francisco, CA (12/14-12/18/2015).
7. Doster, F. (2015). Full Pressure Coupling for Geo-mechanical Multi-phase Multi-component Flow Simulations. Presented at the Scottish Carbon Capture and Storage conference in Edinburgh, Scotland (10/28/2015).
8. March, R. (2015). Modelling CO_2-Storage in Fractured Porous Media: Early and Late Time Behaviour during Imbibition in Dual-Continua Representations. Presented at the Scottish Carbon Capture and Storage conference in Edinburgh, Scotland (10/28/2015).
9. March, R. (2016). Geological Storage of CO_2, Fractured Reservoirs and much more…. Presented at Penn State University in State College, PA (4/20/2016).
10. March, R. (2016). Group Meeting Princeton. Presented at Princeton University in Princeton, NJ (5/6/2016).
11. March, R. (2016). Modelling and Simulation of Geological Storage of CO_2 in fractured formations. Presented at the Institute of Petroleum Engineering Workshop in Edinburgh, UK (6/28/2016).
12. Bandilla, K.W. (2016). Multiscale Modeling of Carbon Dioxide Migration and Trapping in Fractured Reservoirs with Validation by Model Comparison and Real-Site Applications. Talk presented at DOE National Energy Technology Laboratory's Mastering the Subsurface Through Technology, Innovation and Collaboration: Carbon Storage and Oil and Natural Gas Technologies Review Meeting in Pittsburgh, PA (8/16-8/18/2016).
13. Geiger, S. (2016). Talk presented at the Foundation CMG summit in Calgary, Canada
14. Guo, B. (2016). Vertically-integrated Dual-porosity and Dual-permeability Models for CO_2 Sequestration in Fractured Reservoirs. Poster presented at the Flow & Transport in Permeable Media Gordon Research Conference in Girona, Spain (7/31-8/5/2016).
15. March, R., Doster, F., Geiger, S. (2016). Assessment of Fractured Reservoirs as Potential Candidates for Geological Storage of Carbon. Poster presented at the 2016

American Geophysical Union Fall Meeting in San Francisco, CA (12/12 – 12/16/2016).

16. Guo, B., Tao, Y., Bandilla, K., Celia, M. (2016). Vertically-integrated dual-porosity and dual-permeability models for CO_2 sequestration in fractured geological formations. Poster presented at the 13th Conference on Greenhouse Gas Control Technologies (GHGT-13) in Lausanne, Switzerland (11/14 – 11/18/2016).
17. March, R., Doster, F., Geiger, S. (2017). Accurate Dual-porosity Modelling of CO_2-Storage in Fractured Reservoirs. Talk presented at the Society of Petroleum Engineers Reservoir Simulation Conference in Montgomery, TX (2/20 – 2/22/2017).
18. R. March, F. Doster, D. Wong, H. Elder, S. Geiger (2017). Improved Dual Porosity Modelling of Multiphase Flow Phenomena. Talk presented at the Modeling and benchmarking of fractured porous media: flow, transport and deformation workshop in Bergen, Norway (6/8-6/9/2017).
19. R. March, F. Doster, D. Wong, H. Elder, S. Geiger (2017). CO_2 Storage in Naturally Fractured Reservoirs. Poster presented at the Modeling and benchmarking of fractured porous media: flow, transport and deformation workshop in Bergen, Norway (6/8-6/9/2017).
20. K. Bandilla (2017). Multiscale Modeling of Carbon Dioxide Migration and Trapping in Fractured Reservoirs with Validation by Model Comparison and Real-Site Applications. Talk presented at the Mastering the Subsurface through Technology, Innovation and Collaboration: Carbon Storage and Oil and Natural Gas Technologies Review Meeting in Pittsburgh, PA (8/1-8/3/2017).
21. K. Bandilla (2017). Vertically Integrated Models for Carbon Storage Modeling in Heterogeneous Domains. Poster presented at the American Geophysical Union 2017 Fall Meeting in New Orleans, LA (12/11-12/15/2017).
22. Y. Tao (2017). Vertically-Integrated Dual-Continuum Models for CO_2 Injection in Fractured Aquifers. Poster presented at the American Geophysical Union 2017 Fall Meeting in New Orleans, LA (12/11-12/15/2017).
23. C. Oldenburg (2017). Fundamental flux equations for fracture-matrix interactions with linear diffusion. Poster presented at the American Geophysical Union 2017 Fall Meeting in New Orleans, LA (12/11-12/15/2017).
24. C. Oldenburg (2017). Modeling CO_2 storage in fractured reservoirs: Fracture-matrix interactions of free-phase and dissolved CO_2. Poster presented at the American Geophysical Union 2017 Fall Meeting in New Orleans, LA (12/11-12/15/2017).
25. R. March (2017). Modelling and Simulation of Geological Storage of CO_2 in Fractured Formations. Talk presented at the Energi Simulation Meeting in Edinburgh, GB (11/9/2017).
26. R. March (2017). CO_2 Storage in Naturally Fractured Reservoirs. Poster presented at the Energi Simulation Meeting in Edinburgh, GB (11/9/2017).
27. Zhou, Q. (2018). Modeling CO_2 storage in fractured reservoirs: fracture-matrix interactions of supercritical and dissolved CO_2. Talk presented at the 2018 InterPore Conference in New Orleans (5/14-5/17/2018).

28. Zhou, Q. (2018). Benchmark analytical solutions to advection-dispersion in discrete fractures coupled with multirate diffusion in matrix blocks of varying shapes and sizes. Talk presented at the 2018 InterPore Conference in New Orleans (5/14-5/17/2018).
29. Tao, Y. (2018). Vertically-Integrated Dual-Continuum Models for CO_2 Injection in Fractured Saline Aquifers. Talk presented at the 2018 InterPore Conference in New Orleans (5/14-5/17/2018).

6.2 Code for example of dual-porosity code in MRST

```
%% quarterSpotDP - This example outlines the basic usage of the
% two-phase dual-porosity model. We inject the first phase on
% one corner and produce at the opposite one.
clc;
close all;

%% Include the essential modules. dual-porosity model has the functionality
% we need.
mrstModule clear
mrstModule add ad-props ad-core ad-blackoil ad-fi blackoil-sequential

%% Create the grid: a simple cartesian grid, 100m x 100m and 50 blocks on x
% and y directions.

% Two layer grid
x_size = 100;
y_size = 100;
z_size = 1;

Nx = 20;
Ny = 20;
Nz = 1;

G = cartGrid([Nx Ny Nz],[x_size y_size z_size]);
G = computeGeometry(G);

%% We need two rock structures for the dual-porosity model: one for the fracture
% system and one for the non-fractured rock matrix. Fractures usually will
% have high permeability and low pore volume, while matrix usually will
% have a higher porosity and decreased permeability. Therefore,
% interconnected fractures generally serves as a "highway" for fluid flow,
% while the fluid transfer with the matrix will happen at a larger
% timescale
kf = 10000*milli*darcy;
phif = 0.01;

km = 1*milli*darcy;
phim = 0.1;

% Rock Structures
rock_fracture = makeRock(G, kf, phif);
rock_matrix = makeRock(G, km, phim);

%% Pressures of injector and producer wells
pres = 0*psia;
pprod = pres - 1000*psia;
pinj = pres + 1000*psia;

%% We also need two fluid structures for the dual-porosity model. Fractures
% are usually set as having zero capillary pressure, but we don't define any
fluid_matrix = initSimpleADIFluid('mu', [1 2], 'rho', [1 1 1], 'n', [2 2 1]);
fluid_fracture = fluid_matrix;

b = 1/1.2; %reciprocal of formation vol factor.
c = 1e-07/barsa;
fluid_fracture.bW = @(p) b*exp((p - pres)*c);
fluid_fracture.bO = @(p) b*exp((p - pres)*c);

%% We set pc = 0 in the fractures and a linear
% capillary pressure in the matrix. When injecting water in a fractured
% reservoir, the main mechanim of oil recovery is spontaneous imbibition
```

```
% of the water in the fractures into the matrix.
Pcscale = 50*kilo*Pascal;
fluid_fracture.pcOW=@(swm)0;
fluid_matrix.pcOW=@(swm)-Pcscale*swm + Pcscale;

%% Add the wells
W = addWell([],G,rock_fracture,Nx*Ny,'type','bhp','Val',pprod,'Comp_i',[1,1]);
W = addWell(W,G,rock_fracture,1*1,'type','bhp','Val',pinj,'Comp_i',[1,0]);

%% Create the model. TwoPhaseOilWaterDPModel is a modified version of
% TwoPhaseOilWaterModel that adds dual porosity behaviour gravity off

%% Model definition
model = TwoPhaseOilWaterDPModel(G, rock_fracture, fluid_fracture,...
                               rock_matrix, fluid_matrix, []);

% The shape factor and transfer function
fracture_spacing = repmat([1,1,1],G.cells.num,1);
shape_factor_name = 'KazemiShapeFactor';
model.transfer_model_object =
EclipseTransferFunction(shape_factor_name,fracture_spacing);

%% Initialize the field with a constant pressure and fully saturated by oil
state0.pressure = ones(G.cells.num,1)*pres;
state0.s = repmat([0 1],G.cells.num,1);
state0.swm = zeros(G.cells.num,1);
state0.pom = ones(G.cells.num,1)*pres;

%% Initialize the well solution
state0.wellSol= initWellSolAD(W, model, state0);
state = state0;

solver = NonLinearSolver();

%% Handles to pictures that are going to be plotted at each timestep
fig1 = figure(1);

%% Source
src_val = 0.0001*sum(poreVolume(G,rock_fracture))/day;
src = addSource([], 200, src_val, 'sat', [0,1]);

%% Simulate the models
dT = 0.1*day;
n = 20;
for i = 1:n
    %% Advancing fields
    state = solver.solveTimestep(state, dT, model, 'W', W, 'src', src);
    disp(i)

    %% Plotting fields
    figure(fig1)
    subplot(2,2,1)
    title(sprintf('Sw in the fractures'))
    p = plotCellData(G,state.s(:,1));
    p.EdgeAlpha = 0;
    axis equal tight off
    view(-20, 50)

    figure(fig1)
    subplot(2,2,2)
    title(sprintf('Sw in the matrix'))
    p = plotCellData(G,state.swm(:,1));
    p.EdgeAlpha = 0;
```

```
    axis equal tight off
    view(-20, 50)

    figure(fig1)
    subplot(2,2,3)
    title(sprintf('Water transfer rate'))
    p = plotCellData(G,state.Twm(:,1));
    p.EdgeAlpha = 0;
    axis equal tight off
    view(-20, 50)

    figure(fig1)
    subplot(2,2,4)
    title(sprintf('Oil transfer rate'))
    p = plotCellData(G,state.Tom(:,1));
    p.EdgeAlpha = 0;
    axis equal tight off
    view(-20, 50)

    drawnow;
end
```

6.3 Code for example for calling SHPALib

```
!*****************************************************************************************************
!                                   SHPALib  V1.0
! Solute and Heat Transport and Pressure Propagation in the Subsurface: An Analytical Solutions Library
!                                 (revised on 9/21/2018)
!====================================================================================================
!                                    Quanlin Zhou
!                                Energy Geosciences Divison
!                             Lawrence Berkeley National Laboratory
!                                   Berkeley CA 94506
!                           Tel: 510-486-5748, Email: qzhou@lbl.gov
!====================================================================================================
!                             (0) SHPALib2018_0WRRPaper1Main.f90
!====================================================================================================
! Zhou, Q., C.M. Oldenburg, J. Rutqvist, and J.T. Birkholzer (2019c). Revisiting the analytical
!    solutions of heat transport in fractured reservoirs using a multirate memory function.
!    Water Resources Research, 54
!====================================================================================================
! ICASE=1: FIGURE 2    FOR CALCULATED TRANSIENT FLUX (1) USING DIFFUSIVE FLUX EQUATIONS AND
!                      (2) NUMERICALLY INVERTING THE GENERALIZED MEMORY FUNCTION IN THE LAPLACE DOMAIN
!=====================================================================================================
   PROGRAM ZhouAnaModels_2019Flux
   USE SHPALib
   USE DIFFUSIVEFLUX

   IMPLICIT DOUBLE PRECISION (A-H,O-Z)
   INTEGER         IBLOCK        !BLOCK TYPE
   INTEGER         NN            !NN FOR LATE-TIME EXP SOLUTIONS
   INTEGER         IS_PRODUCT    !PRODUCT-FORM SOLUTIONS OR NOT
   DOUBLE PRECISION XYZD(3)      !X-Y-Z/LX-LY-LZ RELATIVE TO THE HALF-SPACING
   DOUBLE PRECISION RLXYZ(3)     !X-Y-Z ASPECT RATIO
   DOUBLE PRECISION CD           !DIMENSIONLESS CONCENTRATION/TEMPERATURE
   DOUBLE PRECISION MD           !DIMENSIONLESS CUMULATIVE FLUX
   DOUBLE PRECISION TDD          !DIMENSIONLESS TIME

   DOUBLE PRECISION TD(600)      !DIMENSIONLESS TIME

   INTEGER         N_TD          !NUMBER OF TIME STEPS
   DOUBLE PRECISION TD0          !STARTING DIMENSIONLESS TIME
   DOUBLE PRECISION TD1          !END DIMENSIONLESS TIME
   DOUBLE PRECISION D_LOGTD      !INCREMENT OF LOG DIMENSIONLESS TIME

   DOUBLE PRECISION FD1(600, 20, 4)  !TRANSIENT FLUX

   CHARACTER*64     PATH
   CHARACTER*120    FILEF(30)

   DOUBLE PRECISION RLY(3), RLZ(3)

   PATH = "C:\4ZhouCodes\0ZhouAnaSolCode\ZhouSolution2018_WRRPaper1\Output\"

   FILEF(1) = PATH//"FLUX_COMPARISON.OUT"

!*****************************************************************************************************
! ICASE-1: COMPARE TRANSIENT FLUX BETWEEN DIRECTLY CALCULATED BY ZHOU'S DIFFUSIVE FLUX EQUATION AND
!        LAPLACE-INVERTED WITH MULTIRATE MEMORY FUNCTION G*(S)
!        WITH RESULTS SHOWN IN FIGURE 2 IN ZHOU ET AL. (WRR, 2018)
!=====================================================================================================
! IBLOCK= 0 FOR 1D DIFFUSION IN SEMI-INFINITE
!      = 1 FOR 1D DIFFUSION IN LAYERS/SLABS FOR PLANE SHEET
!      = 2 FOR 1D DIFFUSION IN RADIAL CYLINDARS
!      = 3 FOR 1D DIFFUSION IN SPHERES
!      = 4 FOR 2D DIFFUSION IN SQUARE COLUMNS OR SQUARES
!      = 5 FOR 3D DIFFUSION IN CUBES
!      = 6 FOR 2D DIFFUSION IN RECTANGULAR COLUMN OR RECTANGLES
!      = 7 FOR 3D DIFFUSION IN RECTANGULAR PARALLELEPIPED
!*****************************************************************************************************
    N_TD = 201
    TD0 = 1.0E-6        !RANGE OF DIMENSIONLESS TIME
    TD1 = 10.0D0
    D_LOGTD = (LOG(TD1)-LOG(TD0))/FLOAT(N_TD-1)
    DO I = 1, N_TD
     TD(I) = EXP(LOG(TD0)+(I-1)*D_LOGTD)
```

```
   ENDDO

   BLOCK_LM(1) = 1.0D0   !SINGLE BLOCK, DIMENSIONLESS
   BLOCK_DM(1) = 1.0D0
   BLOCK_RM(1) = 1.0D0
   BLOCK_WM(1) = 1.0D0

   RLY(1) = 1.0D0
   RLY(2) = 0.5D0
   RLY(3) = 0.2D0
   RLZ(1) = 1.0D0
   RLZ(2) = 0.2D0
   RLZ(3) = 0.1D0

!=====================================================================================
! SOLUTION 1: REAL-TIME-DOMAIN NON-PRODUCT SOLUTION
!=====================================================================================
   CALL BLOCK_T_FLUX_SOLUTIONCOEFFICIENTS_INITIALIZATION()   !SOLUTION COEFFICIENT FOR FLUX-TEMEPRATURE

   !ISOTROPIC BLOCKS
   IS_PRODUCT = 0
   NN = 1            !HIGH-ACCURACY SOLUTION
   DO IBLOCK = 1, 5    !BLOCK SHAPE LOOP
    DO I = 1, N_TD
     CALL MEMORYFLUX_ZHOU_SOLUTION(MD, IBLOCK, TD(I))
     FD1(I, IBLOCK, 1) = MD
    ENDDO
   ENDDO
   WRITE(*,*) "STOP 1"

   !RECTANGLES WITH RLY=[1, 0.5, 0.2]
   RLXYZ(1) = 1.0D0
   RLXYZ(3) = 0.0D0
   NN = 100            !HIGH-ACCURACY SOLUTION
   IBLOCK = 6
   NUM = 5
   DO K = 1, 3        !3 RLY CASES
    NUM = NUM + 1
    RLXYZ(2) = RLY(K)
    CALL BLOCK_T_FLUX_SOLUTIONCOEFFICIENTS_UPDATE(IBLOCK, NN, RLXYZ)
    DO I = 1, N_TD    !RECTANG
     CALL MEMORYFLUX_ZHOU_SOLUTION(MD, IBLOCK, TD(I))
     FD1(I, NUM, 1) = MD
    ENDDO
   ENDDO
   WRITE(*,*) "STOP 2"

   !RECTANGULAR PARALLELEPIPED WITH (RLY, RLZ)=(1,1), (0.5, 0.2), (0.2, 0.01)
   RLXYZ(1) = 1.0D0
   NN = 100            !HIGH-ACCURACY SOLUTION
   IBLOCK = 7
   NUM = 8
   DO K = 1, 3       !THREE RLY CASES
    NUM = NUM + 1
    RLXYZ(2) = RLY(K)
    RLXYZ(3) = RLZ(K)
    CALL BLOCK_T_FLUX_SOLUTIONCOEFFICIENTS_UPDATE(IBLOCK, 100, RLXYZ)
    DO I = 1, N_TD
     CALL MEMORYFLUX_ZHOU_SOLUTION(MD, IBLOCK, TD(I))
     FD1(I, NUM, 1) = MD
    ENDDO
   ENDDO
   WRITE(*,*) "STOP 3"

   !A MIXTURE OF RECTANGULAR PARALLELEPIPED WITH (RLY, RLZ)=(1,1), (0.5, 0.2), (0.2, 0.01)
   DO I = 1, N_TD
    FD1(I, 12, 1) = 0.4D0*FD1(I,9,1) + 0.2D0*FD1(I,10,1) + 0.4D0*FD1(I,11,1)
   ENDDO

!=====================================================================================
! SOLUTION 2: LAPLACE-DOMAIN NON-PRODUCT SOLUTIONS
!=====================================================================================
             Tmax          = 5.0D0
   METHOD         = 3           !method
   Ndiscretization = 200          !Ndiscretization
```

```
ERROR          = 1.0E-8       !Error

CALL MEMORYFUNC_COEFFICIENT_INITIALIZATION()

!ISOTROPIC BLOCKS
N_BLOCK = 1
DO IBLOCK = 1, 5    !BLOCK SHAPE LOOP
  WRITE(*,*) "IBLOCK = ", IBLOCK
  BLOCK_IN(1) = IBLOCK
  CALL MEMORYFUNC_COEFFICIENT_UPDATE()
  WRITE(*,*) BLOCK_A1(1), BLOCK_A2(1), BLOCK_A3(1), BLOCK_B2(1, 1), BLOCK_B3(1, 1), BLOCK_TD0, BLOCK_NN(1)
  DO I = 1, N_TD
    CALL MEMORYFUNC_INVERSION(TD(I), MD)
    FD1(I, IBLOCK, 2) = MD
  ENDDO
ENDDO
WRITE(*,*) "MEMORYFUNC STOP 1"

!RECTANGLES WITH RLY=[1,0.5, 0.2]
BLOCK_RL(1, 1) = 1.0D0
BLOCK_RL(1, 3) = 0.0D0
NN = 100             !HIGH-ACCURACY SOLUTION
IBLOCK = 6
NUM = 5
DO K = 1, 3        !3 RLY CASES
  BLOCK_IN(1) = IBLOCK
  NUM = NUM + 1
  BLOCK_RL(1, 2) = RLY(K)
  CALL MEMORYFUNC_COEFFICIENT_UPDATE()
  WRITE(*,*) "IBLOCK = ", NUM, BLOCK_NN(1)
  DO I = 1, N_TD    !RECTANG
    CALL MEMORYFUNC_INVERSION(TD(I), MD)
    FD1(I, NUM, 2) = MD
  ENDDO
ENDDO
WRITE(*,*) "MEMORYFUNC STOP 2"

!RECTANGULAR PARALLELEPIPED WITH (RLY, RLZ)=(1,1), (0.5, 0.2), (0.2, 0.01)
BLOCK_RL(1, 1) = 1.0D0
IBLOCK = 7
NUM = 8
DO K = 1, 3       !THREE RLY CASES
  BLOCK_IN(1) = IBLOCK
  NUM = NUM + 1
  WRITE(*,*) "IBLOCK = ", NUM
  BLOCK_RL(1, 2) = RLY(K)
  BLOCK_RL(1, 3) = RLZ(K)
  CALL MEMORYFUNC_COEFFICIENT_UPDATE()
  WRITE(*,*) "IBLOCK = ", NUM, BLOCK_NN(1)
  DO I = 1, N_TD    !RECTANG
    CALL MEMORYFUNC_INVERSION(TD(I), MD)
    FD1(I, NUM, 2) = MD
  ENDDO
ENDDO
WRITE(*,*) "MEMORYFUNC STOP 3"

!A MIXTURE OF RECTANGULAR PARALLELEPIPED WITH (RLY, RLZ)=(1,1), (0.5, 0.2), (0.2, 0.01)
DO I = 1, N_TD
  FD1(I, 12, 2) = 0.4D0*FD1(I,9,2) + 0.2D0*FD1(I,10,2) + 0.4D0*FD1(I,11,2)
ENDDO

OPEN(2, FILE = FILEF(1), STATUS = 'UNKNOWN')
 WRITE(2, 2)
 DO I = 1, N_TD
 WRITE(2, 1) TD(I), (FD1(I, K, 1), K=1, 1), (FD1(I, K, 1), K=6, 12)
 ENDDO
 WRITE(2, 3)

 DO I = 1, N_TD
 WRITE(2, 1) TD(I), (FD1(I, K, 2), K=1, 1), (FD1(I, K, 2), K=6, 12)
 ENDDO
CLOSE(2)
1  FORMAT(25E17.9)
2  FORMAT(42HZONE T = "Real-time non-product solutions")
3  FORMAT(38HZONE T = "Lapalce-transform solutions")
```

```
STOP
END
```